

October 9, 2018

## Type Ia Supernova Explosions in Binary Systems: The Impact on the Secondary Star and its Consequences

E. Marietta<sup>1</sup>, Adam Burrows<sup>1</sup>, and Bruce Fryxell<sup>2</sup>

### ABSTRACT

One method of discriminating between the many Type Ia progenitor scenarios is by searching for contaminating hydrogen and helium stripped from the companion star. However, this requires understanding the effect of the impact of the supernova shell on different companion stars to predict the amount of mass stripped and its distribution in velocity and solid angle for the types of binary scenarios that have been proposed as Type Ia progenitor models.

We present several high-resolution 2-D numerical simulations of the impact of a Type Ia supernova explosion with hydrogen-rich main sequence, subgiant, and red giant companions. The binary parameters were chosen to represent several classes of single-degenerate Type Ia progenitor models that have been suggested in the literature. We use realistic stellar models and supernova debris profiles to represent each binary system. For each scenario, we explore the hydrodynamics of the supernova-secondary interaction, calculate the amount of stellar material stripped from the secondary and the kick delivered by the impact, and construct the velocity and solid angle distributions of the stripped material.

We find that the main sequence and subgiant companions lose  $0.15 - 0.17 M_{\odot}$  as a result of the impact of the supernova shell, 15% of their mass. The red giant companions lose  $0.53 - 0.54 M_{\odot}$ , 96% – 98% of their envelopes. The characteristic velocity of the stripped hydrogen is less than  $10^3 \text{ km s}^{-1}$  for all the scenarios:  $420 - 590 \text{ km s}^{-1}$  for the red giant companions,  $820 \text{ km s}^{-1}$  for the main sequence companion, and  $890 \text{ km s}^{-1}$  for the subgiant companion. The stripped hydrogen and helium contaminate a wide solid angle behind the companion:  $115^{\circ}$  from the downstream axis for the red giant,  $66^{\circ}$  for the main sequence star, and  $72^{\circ}$  for the subgiant. With such low velocities, the bulk of the stripped hydrogen and helium is embedded within the low-velocity iron of the supernova ejecta. The hydrogen and helium may be visible in the late-time spectra as narrow emission lines.

Although most of the stripped material is ejected at low velocities, all the numerical simulations yield a small high-velocity tail. The main sequence, subgiant, and the

---

<sup>1</sup>Department of Astronomy and Steward Observatory, The University of Arizona, Tucson, AZ 85721

<sup>2</sup>Enrico Fermi Institute, The University of Chicago, Chicago, IL 60637

red giant companions are just under the Della Valle *et al.* (1996) upper limit from observations of SN 1990M taken near maximum light.

The main sequence companion receives a kick of  $86 \text{ km s}^{-1}$  and the subgiant receives a kick of  $49 \text{ km s}^{-1}$ . In all cases, the kick to the remnant is smaller than the original orbital velocity. Because it is too small to intercept more than a negligible amount of momentum, the red giant core will not receive an appreciable kick.

The impact of the supernova ejecta with the secondary star creates a hole in the supernova debris with an angular size of  $\sim 30^\circ$  in the high-velocity ejecta and with an angular size of  $\sim 40^\circ$  in the low-velocity ejecta. This corresponds to 7 – 12% of the ejecta’s surface. Because we explore binary scenarios that are close enough, or almost close enough, to be in Roche lobe overflow, the degree of asymmetry is similar for all the models. The asymmetry in the supernova debris could have observational consequences beyond the change in morphology of the supernova remnant. The asymmetry in the supernova atmosphere will result in distorted P Cygni profiles that might indicate the presence of the companion star, but it will be difficult to use the degree of asymmetry alone to discriminate between a main sequence, subgiant, or red giant companion.

The impact of the supernova shell will have consequences for the future evolution of the secondary star. After the impact, the main sequence star is puffed up, much like a pre-main sequence star. The luminosity will rise dramatically, to as high as  $\sim 5000 L_\odot$ , as the extended envelope relaxes back into thermal equilibrium. The subgiant companion will follow a similar sequence of events. The star will not be contaminated by much supernova debris from the initial impact, but it may accrete low-velocity iron-group elements (or oxygen and silicon if the ejecta is radially mixed) at late times.

A He pre-white dwarf will be left behind after a supernova explosion with a red giant companion. Almost all the envelope will be ejected by the impact, but a residual amount of material ( $\sim 0.02 M_\odot$ ) will form an extended, hydrogen-rich envelope around the degenerate core. The star will evolve away from the red giant branch on a timescale of  $10^5 - 10^6$  years. On its post-RG track, it may appear as an underluminous O or B star before passing through an sdO or sdB phase on its way to a standard He white dwarf cooling track. This binary scenario could be a possible pathway for the formation of a subset of single, low-mass He white dwarfs.

*Subject headings:* supernovae: general

## 1. Introduction

Unlike a Type II explosion, a Type Ia explosion, the thermonuclear explosion of a CO white dwarf, is characterized by the absence of hydrogen in its spectrum. Although a massive star that is responsible for a Type II supernova explosion can be in a single or a binary system, the Type Ia progenitor scenarios that are based on the thermonuclear explosion of an accreting white dwarf require a companion as a mass donor to enable the white dwarf to reach its critical mass. However, despite searches for the remnant of the companion star, no direct evidence has yet been observed (Ruiz-Lapuente 1997).

One method of discriminating between the many Type Ia progenitor scenarios is by searching for contaminating hydrogen and helium stripped from the companion star. However, this requires understanding the effect of the impact of the supernova blast on different companion stars to predict the amount of hydrogen stripped and its distribution in velocity and solid angle for the types of binary scenarios that have been proposed as progenitor models. To date, there have been only three numerical investigations of supernova impacts on companion stars. Fryxell & Arnett (1981) and Taam & Fryxell (1984) focused on impacts with low-mass main sequence stars. Livne *et al.* (1992) focused on red giant companions. In this paper, we improve upon the earlier theoretical work by exploring the nature of the interaction between the supernova ejecta and the companion star for specific Type Ia binary scenarios with higher resolution than was possible in the past. We select realistic ejecta profiles and realistic stellar models. It is no longer necessary to represent the supernova-secondary interaction by the collision of a simple shell with a polytropic companion. Although the earlier simulations studied the stripped mass and kick, they did not study or provide the distribution of stripped hydrogen in velocity and solid angle, which are essential to predict any spectral signatures of the impact.

The goal of this project is to simulate with a 2-D hydrodynamics code the impact of a realistic supernova blast on a companion star in the context of current Type Ia progenitor scenarios in which the companion is hydrogen-rich. We select several of these scenarios from the literature to cover the possible range of secondary types which are typically low-mass ( $1.0 - 2.0 M_{\odot}$ ) main sequence, subgiant, or red giant stars. We use realistic stellar models and supernova debris profiles to represent each binary system. For each scenario we explore the hydrodynamics of the supernova-secondary interaction, calculate the amount of stellar material stripped from the secondary and the kick delivered by the impact, and construct the velocity and solid angle distributions of the stripped material. With the velocity and spatial distributions of the stripped material within the supernova debris it is possible to predict whether the contaminating hydrogen and helium are observable in the supernova spectrum as broad emission lines near maximum light or as narrow emission lines at late times. In addition, we can explore the change in structure of the secondary star caused by the impact to explore the possible final states (perhaps observable) of the secondary.

We find that our main sequence and subgiant companions lose  $0.15 - 0.17 M_{\odot}$  as a result

of the impact of the supernova ejecta. In contrast, the red giant companions lose almost their entire envelopes,  $0.53 - 0.54 M_{\odot}$ . The bulk of the stripped hydrogen, which has a characteristic velocity of less than or equal to  $10^3 \text{ km s}^{-1}$ , is embedded within the inner, low-velocity supernova debris. The complication that hydrogen and helium can be hidden deep and unseen within the ejecta, and obscured by competing iron and cobalt lines, can be addressed by radiative transfer calculations (Pinto *et al.* 1999). In principle, radiative transfer calculations can reveal how much of the stripped material can be hidden and when it is likely to be observable.

### 1.1. History of Theory

The effect of a supernova explosion on a nearby companion star has been the subject of speculation for many years. One issue raised was the strength of the kick delivered to the companion. Colgate (1970) proposed that the shock-heating of the stellar envelope would cause material to evaporate preferentially back in the direction of the supernova. The secondary would receive a substantial kick from the ablation (evaporation from the surface of the star), as well as a smaller kick from the direct collision with the ejecta. Other groups (Cheng 1974; Wheeler *et al.* 1975) made similar arguments supporting the suggestion that the kick due to ablation was larger than the kick from the collision. Numerical simulations by Fryxell & Arnett (1981) and Taam & Fryxell (1984) showed that the momentum transfer to the secondary was much less than previously thought and that ablation did not substantially increase the kick. The small binary separations we employ for the simulations in this paper, necessary for Roche lobe overflow, result in kicks larger than the  $\sim 10 \text{ km s}^{-1}$  kicks reported by Fryxell & Arnett (1981). However, our typical  $40 - 80 \text{ km s}^{-1}$  kicks are still small in comparison with typical orbital velocities.

The impact of the supernova debris on a nearby companion may be quite dramatic. The supernova ejecta may either directly strip material from the companion by direct transfer of momentum, or, through the conversion of the blast kinetic energy into internal heat, by evaporation. Because the incident energy (a fraction of  $10^{51}$  ergs) greatly exceeds the secondary’s binding energy ( $10^{48}$  ergs), Sofia (1967) suggested that a main sequence secondary in Roche lobe overflow would be completely destroyed. It was not until a more detailed study of the shock propagation into the stellar envelope was done that it was realized that, because the kinetic energy of the impact is deposited in the outer layers of the star, a main sequence star could easily survive such an impact (Cheng 1974).

Wheeler *et al.* (1975) analytically estimated the amount of mass stripped and the kick received by the companion as a result of the inelastic collision and the shock-heating. They calculated the outcome of the impact for an arbitrary secondary star using a geometrical parameter they devised, which depended on the incident momentum and the mass and compactness of the secondary. Their analysis implied that main sequence stars (represented by an  $n = 3$  polytrope), being tightly bound, are only slightly stripped by an explosion in a close binary system. Red giants with loosely-bound envelopes are so catastrophically heated by the impact that the entire envelope is

ejected.

The analytic prescription for the stripped mass and kick proposed by Wheeler *et al.* (1975) was put to the test in a series of numerical simulations of supernova impacts on both low-mass main sequence companions (Fryxell & Arnett 1981; Taam & Fryxell 1984) and low-mass red giants (Livne *et al.* 1992). Fryxell & Arnett (1981) demonstrated that the collision of a supernova shell with a  $2.0 M_{\odot}$ ,  $n=3$  polytrope, with a binary separation 5.9 times the stellar radius, ejects  $0.013 - 0.052 M_{\odot}$  from the secondary, a mass loss roughly consistent with the analytic estimates of Wheeler *et al.* (1975). Although in their study the emphasis was on the momentum transfer rather than the stripped mass, Taam & Fryxell (1984) performed numerical simulations with  $n=3/2$  and  $n=3$  polytropes that were designed to represent the range of compactness expected from a fully convective star to a radiative star. They found that the momentum was more efficiently transferred for the  $n=3/2$  star, which is less centrally concentrated than the  $n=3$  star. The stripped  $n=3/2$  star presents a larger geometrical area to intercept the momentum, even when a higher fraction of mass is stripped, so that the momentum transfer is more efficient. More recently, Livne *et al.* (1992) simulated a Type Ia supernova explosion of a white dwarf in a close binary with a low-mass red giant that is almost close enough to be in Roche lobe overflow. The blast stripped the red giant of almost its entire envelope, imparting a velocity to the stripped material well below the velocity of the supernova ejecta. This not only confirmed the conclusion of Wheeler *et al.* (1975) that the impact would destroy the red giant, but also verified a prediction of Chugai (1986). Chugai (1986) focused on the supernova red giant interaction for Type Ia events in which the hydrogen donor is a symbiotic star - with a binary separation 3 – 10 times the red giant’s radius. Chugai’s analytic model predicted that  $0.3-1.0 M_{\odot}$  would be ejected from the companion with a characteristic velocity less than or equal to  $10^3 \text{ km s}^{-1}$ , much smaller than the  $10^4 \text{ km s}^{-1}$  characteristic velocity of the supernova ejecta, and that it would fill the inner 20% of the radius of the supernova ejecta. The confirmation by Livne *et al.* (1992) of the low velocity of the stripped hydrogen has important implications for the identification of Type Ia progenitors. Our more detailed calculations build on and extend this earlier, seminal work.

## 1.2. Discriminating Between Type Ia Progenitor Scenarios by Searching for Hydrogen

The exact amount of hydrogen stripped and its characteristic velocity is a key issue in light of the current interest in identifying the progenitors of Type Ia supernovae. Because it is difficult to reconcile the extremely hydrogen-poor spectra with the presence of a hydrogen-rich companion, the amount of stripped hydrogen can be used to discriminate between Type Ia progenitor scenarios. Type Ia explosions, which are characterized by a lack of hydrogen, could be the result of mass accretion onto a white dwarf in a binary system (single-degenerate scenario) (Whelan & Iben 1973; Nomoto 1982a) or the merging of two degenerate white dwarf stars (double-degenerate scenario) (Iben & Tutukov 1984; Webbink 1984). Naturally, the double-degenerate scenario could account

for the lack of hydrogen in the supernova spectrum. However, no double-degenerate binaries have been found that are close enough to merge within a Hubble time and are massive enough to exceed the Chandrasekhar mass (Marsh *et al.* 1995; Saffer *et al.* 1998). The single-degenerate scenario is currently in favor (Livio 1999). If the companion is a main sequence, subgiant, or red giant star, the single-degenerate scenario necessarily implies that the binary system is rich in hydrogen. Hydrogen-rich material could be ejected from the secondary star as a consequence of the impact of the supernova shell. Hydrogen could also be present in the immediate environment as circumstellar material from stellar winds, mass lost from the primary in an earlier phase of mass transfer, or even as a layer of hydrogen on the white dwarf primary. If the hydrogen is swept up by the supernova ejecta, the origin of the material may determine its characteristic velocity, which in turn determines when it is most likely to be observed. Circumstellar material swept up with the supernova ejecta is expected to be observed as transient narrow  $H_\alpha$  emission or absorption lines (Wheeler 1992; Filippenko 1997) near maximum light. If the hydrogen is stripped from the secondary and embedded within the inner iron layer of the supernova ejecta, it is more likely to be observed in emission as narrow  $H_\alpha$  lines months after maximum light (Chugai 1986). Searches for hydrogen must be targeted at either early-times near maximum light or at late-times when the photosphere has receded to reveal the iron layer (Chugai 1986).

Identification of hydrogen at early-times, either in emission or absorption, has been claimed in at least three Type Ia supernovae: 1981B, 1990M, and 1990N. Branch *et al.* (1983) presented high-quality optical spectra of SN1981B from maximum light to 116 days post-maximum. Their March 13 observation showed a small, narrow emission feature consistent with the rest wavelength of  $H_\alpha$ . The feature was absent from a spectrum that was taken just 5 days later. Unable to firmly conclude that the feature was  $H_\alpha$ , they suggested that high-resolution spectra be taken of supernovae near the same phase ( $\sim 6$  days past maximum light) to search for  $H_\alpha$  emission. Cumming *et al.* (1996) searched for narrow  $H_\alpha$  emission in high-resolution spectra of SNIa 1994D 10 days before maximum and 6.5 days after maximum without detecting any hydrogen either in emission or absorption. Likewise, Ho & Filippenko (1995) in their high-resolution echelle observations of SNIa 1994D at 23 days past maximum did not detect any  $H_\alpha$  in emission or absorption.

From a series of observations of SNIa 1990N from 14 days before maximum light to 1 week past maximum light, Leibundgut *et al.* (1991) suggested that an unidentified absorption feature at  $6300\text{\AA}$  could be hydrogen. They suggested that a thin layer of hydrogen on the surface of the progenitor star could be responsible for the feature, but because the velocity of the feature ( $1.2 \times 10^4 \text{ km s}^{-1}$ ) was much lower than that of the other lines, this was unlikely. Later, based on an analysis of optical and UV spectra of SN 1990N using synthetic spectra, Jeffery *et al.* (1992) concluded that the unidentified absorption feature at  $6300\text{\AA}$ , and an additional unidentified feature at  $6900\text{\AA}$ , were probably due to C II at  $6580\text{\AA}$  and  $7243\text{\AA}$ .

Polcaro & Viotti (1991) identified a broad  $H_\alpha$  absorption feature in SNIa 1990M at four days after maximum light. This was later convincingly ruled out by Della Valle *et al.* (1996), who

showed from a spectrum obtained a few days past maximum light that the absorption feature was due solely to observational bias. They found no evidence of  $H_\alpha$  in SN 1990M. Using an upper limit to the  $H_\alpha$  equivalent width and a measurement of the Si II 6350Å equivalent width, they set an upper limit in the supernova atmosphere for H/Si of  $2.0 \times 10^{-6}$ , relative to solar. By assuming perfect mixing and using the abundances of the standard W7 model (Nomoto *et al.* 1984), they derived the upper limit to the mass fraction, X(H), of 0.007. However, they pointed out that if the hydrogen is buried deep within the supernova ejecta instead of being perfectly mixed, the integral mass fraction could be much higher. Likewise, if the hydrogen is restricted to the outer layers, the mass fraction could be much lower. Scaling X(H) by the ratio of the mass in the atmosphere to the total mass and assuming that 20 days past the explosion only 1/20 of the ejecta are revealed, they derived an X(H) of  $\sim 0.007 M_{atm}/M_{tot} \approx 3 \times 10^{-4}$ .

A similar argument was made earlier by Applegate & Terman (1989) to place an upper limit on the hydrogen mass fraction in SN 1981B. Using the upper limit of  $[H/Si] < -4.0$  in the LTE spectral fit to the maximum light observations of SN 1981B of Branch *et al.* (1982), Applegate & Terman (1989) derived an upper limit on the hydrogen mass fraction near maximum light in SN 1981B of 0.02. To find a lower limit to the hydrogen contamination due to the impact of the supernova ejecta on the secondary star, Applegate & Terman used the analytic prescription developed by Wheeler *et al.* (1975). They focused on a cataclysmic variable system with a  $0.2 M_\odot$  main sequence companion, represented by an  $n=3/2$  polytrope, that was close enough to the primary to be in Roche lobe overflow. If the Type Ia progenitors are cataclysmic variables, Applegate & Terman 1989 concluded that  $X(H) > 0.01$ . This is just below the Applegate & Terman upper limit of  $X(H) < 0.02$ . In contrast, if the companion is a low-mass red giant with an envelope mass of  $0.5 M_\odot$ , then  $X(H) > 0.20$ , which clearly would exceed the upper limit they deduced from observations of SN 1981B. Applegate & Terman (1989) conclude that binary scenarios with hydrogen-rich companions are not likely candidates for Type Ia progenitors. However, to directly compare their lower limit with their upper limit based on maximum light observations of SN 1981B, they implicitly assumed that the stripped hydrogen from either the low-mass main sequence star or the red giant companion was ejected at high velocities.

It is currently believed, based on the work of Chugai (1986) and Livne *et al.* (1992), that any material stripped from a red giant companion will have a characteristic velocity  $\lesssim 10^3$  km  $s^{-1}$ , much lower than that of the supernova ejecta. As we show below, we agree with this general conclusion. If any hydrogen is embedded within the supernova ejecta, narrow hydrogen emission lines will appear only after the photosphere retreats into the iron layer. Thus, a critical test of the presence of a secondary star is the detection of low-velocity hydrogen lines in the late-time spectrum (Ruiz-Lapuente *et al.* 1993). However, such a detection is difficult because of the number of Fe lines that overwhelm the spectrum. To date, there has been only one claim of a detection of a low-velocity hydrogen line, ostensibly from a stripped companion. Ruiz-Lapuente *et al.* (1993) initially identified a weak  $H_\alpha$  line in a spectrum of SNIa 1991bg, a peculiar underluminous Type Ia supernova, 197 days after maximum light. However, this was not verified by Turatto *et al.* (1996).

Turatto *et al.* were not able to associate any emission lines with  $H_\alpha$  in their observations of SN 1991bg, although they suggested a possible blend with [Co III] at 6578Å or numerous Fe II and [Fe II] lines in that region of the spectrum. Garnavich & Challis (1997), in a reanalysis of a spectrum of SN 1991bg at 200 days after maximum light, confirmed the existence of the narrow emission lines of Ruiz-Lapuente *et al.* (1993), but they could not unambiguously identify them.

A key question for theoreticians is how much contaminating hydrogen and helium, whether of circumstellar or companion origin, can be hidden within the supernova ejecta. Very few theoretical upper limits have been set (Wheeler & Harkness 1990; Wheeler 1992). Wheeler (1992) claimed that, if the hydrogen is in LTE in the outer layers of the supernova ejecta, as much as  $0.1 M_\odot$  could be present without contributing to the spectrum at maximum light. Branch *et al.* (1991) found a tighter upper limit of 1% by mass ( $\sim 0.01 M_\odot$ ) in a non-LTE calculation. By adding hydrogen to a synthetic spectrum and comparing with the maximum-light optical spectrum of SN 1981B, they concluded that 1% by mass is an upper limit on the hydrogen contamination for a layer of hydrogen uniformly mixed in the line-forming layer at maximum light. They found that, not only would a weak  $H_\alpha$  line be visible, but, as an indirect consequence of hydrogen contamination, that the optical depth in the Lyman continuum would change the ultraviolet radiation field, the ionization structure in the line-forming layer, and, hence, the strengths of many of the non-hydrogen lines. Because Applegate & Terman (1989) estimated  $X(H) > 0.01$ , Branch *et al.* (1991) concluded that accreting white dwarfs with hydrogen-rich companions are unlikely to be progenitors of Type Ia supernovae. However, there are several caveats. First, the synthetic spectra employed for these investigations were done only near maximum light, when only high-velocity hydrogen would be visible. If most of the contaminating hydrogen is at low velocities, synthetic spectra need to be calculated at much later times when the photosphere has receded into the inner ejecta. Second, the hydrogen buried within the supernova ejecta may not be uniformly mixed in angle. Because non-uniform mixing may act to hide the embedded hydrogen, the angular dependence of the spectra needs to be considered.

In this paper, we explore in detail the theoretical expectations for the distribution of hydrogen and helium in Type Ia debris, the hydrodynamic character of the impact, the kick to the secondary, and the nature of the post-impact structure. In §2, we review the numerical methods used. In §3, we describe the classes of supernova Type Ia progenitor scenarios and the criteria for selecting the candidate scenarios. In §4, we discuss details of the main sequence simulations, including the hydrodynamics of the impact, the stripped mass, the velocity and solid angle distributions of the stripped material, and the kick received by the companion. In §5, we present a sequence of simulations with the main sequence secondary to determine systematic trends in the quantity of stripped hydrogen and its velocity and solid angle distributions as the binary separation increases. In §6, we discuss details of the subgiant simulations, including a description of the impact, the stripped mass, the velocity and solid angle distributions of the stripped material, and the kick received by the companion. Section 7 contains similar details for the red giant



simulations. In §8, we explore the implications of the revealed velocity distributions of the stripped material and the possibility that contaminating hydrogen may be observable in a Type Ia supernova spectrum. In §9, we speculate on the effect of the impact on the future evolution of the secondary, and in §10 we summarize our conclusions and suggest directions for future work. Postscript images, MPEG movies, and a selection of figures presented in this paper, are posted at <http://www.astrophysics.arizona.edu> and are available via FTP at [www.astrophysics.arizona.edu](http://www.astrophysics.arizona.edu), in directory `pub/marietta`.

## 2. Numerical Methods and Techniques

The hydrodynamics code we employ for these simulations is an extension of the code, *Prometheus* (Fryxell *et al.* 1989), which is based on the Piecewise-Parabolic Method (PPM) (Colella & Woodward 1984; Colella & Glaz 1985). Our version of PPM is a non-relativistic, explicit, automatically conservative, Eulerian scheme that achieves second-order spatial and temporal accuracy. Fluxes at interfaces are obtained by solving the Riemann shock-tube problem and shocks are resolved to one or two zones.

A simple equation of state, including just radiation and ideal gas, is employed for all the calculations involving the main sequence companion and the envelope of the red giant; the degenerate core of the red giant is added only as a gravitational point mass. For the calculations involving subgiant companions, where degenerate electrons are required, we use a tabulated equation of state with arbitrary degeneracy and relativity. We tabulate the pressure, energy, and entropy of the ionization electrons, and any pair-produced electrons and positrons, by directly integrating the appropriate Fermi-Dirac integrals, following the prescription of Cox & Giuli (1968). Using the ionization electron density ( $n_e = \rho Y_e N_{av}$ , where  $\rho$  is the density,  $Y_e$  is the electron fraction, and  $N_{av}$  is Avogadro's number) and the temperature ( $T$ ) as independent variables, we use an iterative technique to solve for the degeneracy factor ( $\eta = \mu/k_B T$ , where  $\mu$  is the chemical potential, and  $k_B$  is Boltzmann's constant), which can be used to directly integrate the Fermi-Dirac integrals for pressure and energy. This method, although laborious, is thermodynamically consistent. The table, once generated, is accessed by a second-order interpolation routine. We estimate the pressures and energies to be accurate to better than  $\sim 10^{-4}$ .

We incorporate into PPM an integral Poisson solver created by Müller & Steinmetz (1995) to calculate the gravitational potential for an arbitrary 2-D mass distribution. Having found the gravitational potential, the gravitational force can be calculated using a finite difference approximation to the gradient. In the simulations involving the red giant companions, the gravitational point mass of the compact core is added directly to the force. In our implementation the solver expands the gravitational potential in Legendre polynomials. Up to twenty moments can be employed, including the dipole moment which we include to allow the secondary to move freely down the hydrodynamic grid in response to the impact of the blast. With the

addition of an interpolation routine, the hydrodynamical equations can be differenced in spherical  $(r, \theta)$ , Cartesian  $(x, y)$ , or cylindrical coordinates  $(\rho, z)$  while the gravitational potential can be constructed in spherical coordinates  $(r, \theta)$ . To improve accuracy, the gravitational potential can be centered on the center of mass at each cycle, in effect following the star as it moves down the grid. This decreases errors, notably in the stellar core, that over the long timescale of the simulation can otherwise slowly decrease the star’s terminal velocity. Even with this improvement, the terminal velocity slowly decreases at an average rate of  $\sim 2.8\%$  per stellar sound crossing time in a typical simulation with a low-mass main sequence companion. Thus, as will be seen in §4.6, we determine the kick after the terminal velocity is reached (4000 – 5000 seconds), but before the small errors have time to grow appreciably.

For simplicity, we use all the mass on the hydrodynamic grid, stellar and supernova, to calculate the gravitational potential. Because the grid is so large, typically  $6R$  ( $R =$  the stellar radius) in the  $\rho$  direction, and, since the explosion is  $\sim 1R$  away from the upper boundary, about 42% of the supernova debris passes through the grid. Only a small fraction of the ejecta directly collides with the secondary. The characteristic velocity of the supernova ejecta is so fast that the error to the kick from including the supernova material on the grid is only  $\sim 4 \text{ km s}^{-1}$ , which is an error of  $\sim 5\%$ .

For this project, a selection of low-mass stellar models were evolved by Chaboyer (1998). Following the lead of Sills *et al.* (1997), we reintegrate the main sequence and subgiant secondaries using a 1-D fourth-order Runge-Kutta program, the entropy and composition profiles, and the same equation of state used in our PPM code. We do not attempt to reproduce the distortions in the secondary due to the Roche lobe geometry.

The weakly-bound envelope of the red giant requires special treatment. We reintegrate its entropy profile with a softened potential ( $\phi(r) = -GM_c/(r + r_c)$ ) to help stabilize it. Even with this adaptation, we find it necessary to switch to spherical coordinates for the red giant impacts. We surround each secondary star with a high-entropy, very low-density hydrostatic envelope which serves to fill the Eulerian grid with a background medium. In later sections we refer to this background material as the “circumstellar” medium to distinguish it from the stellar envelope. The new 1-D models with their hydrostatic envelopes are interpolated onto a 2-D cylindrical grid (main sequence or subgiant models) or a 2-D spherical grid (red giant envelopes). We use 2-D cylindrical coordinates whenever possible in order to efficiently follow the stripped material. To stabilize the envelope of the red giant, we must use 2-D spherical coordinates.

We verify that each secondary star remains in hydrostatic equilibrium by running a simulation without the supernova explosion. The main sequence and subgiant simulations were run for three sound crossing times. Because the envelope of the red giant will be completely disrupted in less than one sound crossing time, the red giant simulation was run for only one sound crossing time. We estimate the fractional change in radius by the fractional change in gravitational energy for the main sequence and subgiant secondaries. We find that the radius changes by at most  $\sim 1\%$ .

In the red giant case, the radius changes by at most  $\sim 8\%$ .

We perform all of the simulations with the main sequence and subgiant secondaries in 2-D using cylindrical coordinates  $(\rho, z)$ , with the  $z$ -axis defined to be the direction joining the primary and secondary of the original binary system. We estimate that the error in neglecting the orbital motion of the secondary, necessary for a 2-D calculation, is  $\sim 10^{-2}$ , the ratio of a typical orbital velocity of  $10^2 \text{ km s}^{-1}$  to a characteristic velocity of the supernova ejecta of  $10^4 \text{ km s}^{-1}$ . The thermonuclear explosion of the white dwarf occurs exterior to the grid and the supernova ejecta, specified by a realistic density and velocity profile, flows onto the grid via time-dependent boundary conditions in assumed spherical homologous flow. The other exterior boundaries are subject to the constraint that material is allowed only to leave the grid. The interior boundary ( $\rho = 0$ ) is reflecting.

We switch to spherical coordinates for the red giant companions because only in these coordinates is the loosely-bound envelope of the red giant stable. We position the red giant envelope at the origin and add a gravitational point mass to the force to represent the degenerate core. We assume throughout the simulation that the degenerate core does not move as a result of the impact. We justify this by noting that, because of the extremely small solid angle subtended by the degenerate core and its very high areal density, it can receive only a negligible ( $\ll 1 \text{ km s}^{-1}$ ) kick. The supernova explosion, which in this case occurs on the grid, is interpolated onto the grid from a post-explosion ejecta profile. To avoid numerical problems associated with high-Mach flows, we assume an initial temperature in the supernova ejecta high enough that the internal energy is  $\sim 7.7\%$  of the specific kinetic energy.<sup>3</sup> To minimize numerical problems at the center of the supernova where the expansion leaves a low-density interior, we employ a minimum temperature which decreases linearly with time to mimic the cooling of the interior. Outside of the supernova ejecta at the interface between the supernova ejecta and the “circumstellar” medium, a minimum temperature of 100 K is enforced. These numerical problems appear only in the spherical calculations. The cylindrical calculations in which the supernova is added by time-dependent boundary conditions are always well-behaved.

With the change to spherical coordinates, we alter the boundary conditions. The outer boundary is straightforward. As in cylindrical coordinates, the outer radial boundary is transmitting, but subject to the constraint that material is allowed only to leave the grid. The inner radial boundary is fixed at a small, but non-zero, radius. This helps to stabilize the interior of the envelope and, in addition, helps to avoid Courant problems. The inner boundary is non-transmitting (no mass flux allowed) with a zero-velocity condition. The inner boundary seems to affect the flow only after the envelope has been stripped. After the mass-stripping phase of the interaction, we regrid the calculation by removing the innermost zones, usually the first 25, in effect moving the inner boundary outward about a factor of 10 in radius, which increases the

---

<sup>3</sup> Our initial temperature is a factor of 1.0 – 4.0 higher than the temperature provided in the supernova ejecta model hedtb11 (Woosley & Weaver 1994).

timestep by the same factor, allowing us to continue the simulations efficiently. The mass enclosed in the innermost zones is added to the gravitational point mass. The region removed is typically only 1% in radius, and therefore, only  $10^{-4}\%$  in computational volume. The boundary along the axis of symmetry is reflecting. For high-velocity flow, the axis of symmetry manifests minor numerical artifacts which, however, do not affect the conclusions of the work.

In addition to determining the stripped mass and the kick given to the companion, we find the distribution of the stripped material in both velocity and solid angle. The velocity distribution can in principle be used with a radiative transfer code to predict when, and if, the contaminating hydrogen is observable in the supernova Type Ia spectrum and to place useful constraints on the type of binary scenarios likely to be responsible for Type Ia supernovae. The solid angle distribution can be used to determine by how much the stellar material lags behind the supernova ejecta and the size of the solid angle contaminated by the stellar hydrogen and helium. It may also be relevant for estimates of the polarization of the emergent light. As stripped stellar material flows through the outer boundary, we record its mass, velocity, entropy, and composition. We advect the electron fraction  $Y_e$  and ion fraction  $Y_i$  along with ten general composition labels, five of which are reserved for the Type I supernova ejecta (“hydrogen”, “helium”, “oxygen-group”, “silicon”, and “iron-group”), four for the companion star (“hydrogen”, “helium”, “oxygen-group”, and “silicon/iron-group”), and one for the “circumstellar” medium. The  $Y_i$  and  $Y_e$  are required by the equation of state, but we advect the composition labels as mass fractions so we can keep track of the origin of the stripped companion material and can distinguish it from the supernova and “circumstellar” material with which it is intermixed. To find the velocity and solid angle distributions, we include the distribution of the stripped companion material on the grid, as well as the stripped material that has left the grid. The stripped mass left on the grid is usually extremely small, given the length of a typical simulation.

For the main sequence and subgiant simulations we generally employ a  $\sim 300(\rho) \times 600(z)$  cylindrical grid, and for the red giant a  $\sim 600(r) \times 300(\theta)$  spherical grid, with nonuniform zoning that is finest in the region surrounding the secondary and coarsest near the edge of the grid. To cover 6 stellar radii around the secondary and still resolve the center of the star well enough to maintain hydrostatic equilibrium, nonuniform zoning is necessary. This nonuniform zoning, although efficient, creates difficulties in quantifying the effect of increasing or decreasing the resolution.

To test the effect of the resolution we employ a cylindrical grid that has uniform zoning in a rectangular region enclosing the secondary. Outside this region, the zones are slowly increased in size to keep the calculation tractable. For the main sequence calculation, we performed two simulations: one with a spacing of  $8.0 \times 10^3$  km requiring a  $300(\rho) \times 550(z)$  grid and one with a slightly smaller spacing of  $6.0 \times 10^3$  km requiring a  $320(\rho) \times 845(z)$  grid. We can not vary the “resolution” by a large factor because greatly decreasing the resolution destabilizes the secondary while greatly increasing the resolution creates enormous Courant and data storage problems.

Nevertheless, we find that changing the resolution in the region around the secondary can affect the results in several systematic ways. First, the amount of mass stripped increases, but only very slightly, as the resolution increases. In the high-resolution simulation the secondary lost almost  $\sim 0.1\%$  more mass than in the low-resolution simulation. Second, as the resolution increases, the kick to the remainder of the secondary increases. The velocity of the center of mass follows the same overall profile, the only difference being a slight increase of 1.1% in the terminal velocity. An increase in momentum transfer with higher resolution was noted by Taam & Fryxell (1984). They attributed this trend to a more accurate description of the momentum transfer in the outer layers of the star, where the shock energy is deposited, because of the steep density gradient there. Third, as the resolution increases, the velocity of the stripped material systematically shifts to slightly lower velocities. The velocity at the half-mass point shifts from  $841 \text{ km s}^{-1}$  to  $829 \text{ km s}^{-1}$ . If with higher resolution the transfer of momentum to the remainder of the secondary is more efficient, then less momentum is available for the stripped material. Apart from the subtle systematic shift as the resolution changes, the features in the moderate-velocity region ( $1000 - 3000 \text{ km s}^{-1}$ ), which we associate in §4.1 with the composition transitions in the supernova ejecta, vary in position and amplitude. However, the velocity distributions of the low- and high-resolution calculations show the same overall profile, especially at the low- and high-velocity tails. Above  $3 \times 10^3 \text{ km s}^{-1}$ , the low-resolution distribution has 12% more mass than the high-resolution simulation. To reprise, as the resolution increases, the amount of stripped mass and the kick imparted to the secondary increase slightly, and the half-mass velocity of the stripped material decreases slightly.

### 3. Standard Type Ia Supernova Binary Scenarios

A Type Ia supernova could be the product of a merger of CO white dwarf with a He or CO white dwarf (double-degenerate scenario), or the explosion of a white dwarf which has reached its Chandrasekhar mass by accreting hydrogen or helium from a nondegenerate companion (single-degenerate scenario) (Iben & Tutukov 1984). These two competing binary scenarios originate from very different evolutionary paths and naturally have different predictions for the Type Ia supernova rates. Binary population synthesis, a statistical tool for exploring the possible phases of binary evolution, can be used to estimate rates for progenitor scenarios to discriminate between progenitor models (cf. Iben & Tutukov 1984; Tutukov *et al.* 1992; Branch *et al.* 1995). However, the Type Ia supernova rates from population synthesis calculations suffer from serious uncertainties. Common envelope evolution is not well-understood. It is parameterized by  $\alpha_{CE}$ , the efficiency with which the orbital energy is used to eject the common envelope, whose value is uncertain. The realization frequencies are dependent on the stellar population and age. Another complication arises from the different models for the thermonuclear explosion of the white dwarf. In a Chandrasekhar explosion (the standard model), the CO white dwarf accretes material until it approaches the Chandrasekhar mass and carbon ignites in the core (Woosley & Weaver 1986). In sub-Chandrasekhar explosions, the ignition occurs in a helium layer around the CO white dwarf

before the Chandrasekhar mass is reached (Nomoto *et al.* 1982b). In general, binary population synthesis calculations favor the double-degenerate scenario over the single-degenerate scenario (Branch *et al.* 1995). Recent calculations by Branch *et al.* (1995) for a young population ( $10^8$  yr) find double-degenerate rates of  $\sim 10^{-3}$  yr $^{-1}$ . This is closer to the current galactic Type Ia supernova rate of  $4.0 \times 10^{-3}$  yr $^{-1}$  than the rates of  $10^{-4} - 10^{-6}$  yr $^{-1}$  for each of the many possible single-degenerate scenarios. But, for an older population ( $10^{10}$  yr) the double-degenerate rate drops to  $\sim 10^{-4}$  yr $^{-1}$  which can be matched by the realization frequency for symbiotic systems, a single-degenerate scenario in which the white dwarf accretes hydrogen from the wind of its red giant companion. Likewise, Ruiz-Lapuente (1996) finds that for an Sb galaxy the double-degenerate rate is  $\sim 10^{-4}$  yr $^{-1}$ , but that several single-degenerate scenarios have rates similar to this. Because of the complexity of the population synthesis calculations, it is difficult to exclude any Type Ia progenitor scenario outright just on the basis of realization frequencies. The presence of hydrogen in Type Ia supernova spectra is a stronger indication of a single-degenerate progenitor system because any Type Ia explosion in a double-degenerate binary system is expected to be hydrogen-free. In this paper, we examine only the single-degenerate scenarios for Type Ia supernova explosions.

Single-degenerate Type Ia models can be coarsely subdivided (see Table 1) into Hydrogen Cataclysmic Variables (H CV), Hydrogen Cataclysmic-Like Variables (H CVL), Symbiotic Stars (SS), Hydrogen Algols (H Algols), Helium Cataclysmic Variables (He CV), and Helium Algols (He Algols), based on the evolutionary stage of the secondary, method of mass transfer, and composition of the secondary’s envelope (Branch *et al.* 1995; Ruiz-Lapuente 1996). The secondary can be a low-mass main sequence, subgiant, or red giant star that slowly loses its envelope to the primary by Roche lobe overflow for close binaries or by stellar winds for wider binaries. The mass transferred can be hydrogen or helium in cases where the hydrogen layer has already been lost by earlier phases of mass transfer.

In the H CV scenario, a CO white dwarf, left in a close binary orbit by an earlier episode of common envelope evolution in its AGB phase, accretes hydrogen by Roche lobe overflow from a lower-mass main sequence secondary. The mass transfer is maintained by magnetic braking and has a characteristic rate of  $\dot{M} > 1.0 \times 10^{-8} M_{\odot}$  yr $^{-1}$  (Verbunt & Zwaan 1981). Not all H CV systems end as Type Ia supernova progenitors. Only the largest white dwarfs with the highest mass transfer rates, high enough to suppress hydrogen flashes, can accrete enough mass to reach the Chandrasekhar mass. Livio & Truran (1992) associated these binaries with recurrent nova systems. When the Chandrasekhar mass is reached, the white dwarf explodes as a Type Ia supernova, but only if it can avoid accretion-induced collapse (Nomoto & Kondo 1990). Della Valle & Livio (1994) suggested these binaries could be responsible for Type Ia events in late-type galaxies while another progenitor from an older stellar population could be responsible for Type Ia events in early-type galaxies.

The H CVL systems have an evolutionary path like that of the H CV systems. After an episode of common envelope evolution, a white dwarf is left in a close binary orbit with a slightly

higher-mass main sequence or subgiant secondary. Because of the mass ratio, the mass transfer is unstable and proceeds on a thermal timescale. This higher mass transfer rate ( $\dot{M} \sim 10^{-6} M_{\odot} \text{ yr}^{-1}$ ) is responsible for the steady burning of hydrogen to helium on the surface of the white dwarf. Eventually, the Chandrasekhar mass is reached and the star explodes (Rappaport *et al.* 1994; Hachisu *et al.* 1996; see also Hachisu *et al.* 1999b).

We use the H Algol and Symbiotic classification, following the path of Branch *et al.* (1995), as a general term to describe binaries in which the donor is a red giant that slowly loses mass to the white dwarf. In these scenarios, after a common envelope phase, a CO white dwarf is left in a binary orbit with a main sequence star. In the H Algol scenario, the main sequence secondary evolves all the way to the red giant phase before filling its Roche lobe for the first time (Whelan & Iben 1973; Iben & Tutukov 1984). Mass transfer to the white dwarf is by Roche lobe overflow, like the other Type Ia progenitor scenarios. In the symbiotic scenario, the red giant is too distant to fill its Roche lobe in the course of its evolution. Mass loss will occur by stellar winds. Many evolutionary paths can lead to the symbiotic scenario, the simplest being a wide binary whose stars evolve independently. Other possible paths include prior phases of common envelope evolution or conservative mass transfer during the primary’s evolution, which leaves the binary separation too wide for the secondary to ever fill its Roche lobe (Yungelson *et al.* 1995). Until recently, symbiotics were considered as viable Type Ia candidates only for sub-Chandrasekhar explosions (Kenyon *et al.* 1993; Yungelson *et al.* 1995). However, recently Hachisu *et al.* (1999a) have proposed that symbiotic systems with Chandrasekhar explosions can account for the Type Ia rate.

The He CV and He Algol classes are analogous to the H CV and H Algol classes, the primary difference being that the mass transferred is helium instead of hydrogen. This complicated evolutionary path begins with the creation of a white dwarf in a close binary orbit, following a phase of common envelope evolution with a main sequence star, as in the previous scenarios. The secondary evolves through the red giant phase. However, unlike the earlier scenarios, the secondary catastrophically loses its hydrogen envelope in another common envelope phase. The secondary, now a helium star, continues to evolve. For the He CV scenarios, mass transfer begins when the helium star goes into Roche lobe overflow. Stable mass transfer ( $q < 1$ ) is maintained by gravitational wave radiation and proceeds on a nuclear timescale. For these binaries, helium star masses are typically in the range of  $0.3 - 1.0 M_{\odot}$  and white dwarf masses are in the range of  $0.6 - 1.0 M_{\odot}$ . These are Type Ia supernova Chandrasekhar and sub-Chandrasekhar explosions (Iben & Tutukov 1991). For the He Algol scenarios, mass transfer begins during the secondary’s expansion to a helium giant. Mass transfer is quasi-stationary ( $\dot{M} \sim 10^{-6} M_{\odot} \text{ yr}^{-1}$ ) with secondary masses in the range of  $0.75 - 2.3 M_{\odot}$  and with white dwarf masses in the range of  $0.9 - 1.4 M_{\odot}$ . The He Algol systems are candidates for Type Ia Chandrasekhar explosions (Iben & Tutukov 1994). Branch *et al.* (1995) finds that the realization frequencies for these scenarios are  $10^{-4} - 10^{-5} \text{ yr}^{-1}$  for young populations and are negligible for old populations.

In this paper, we focus on exploring the supernova-secondary interaction for the four hydrogen-rich scenarios in Table 1. To simulate each impact, we select a representative binary

system from the literature for each of the four scenarios and estimate the binary separation and the companion’s mass at the time of explosion. We use a stellar model in the simulation that is reasonably close in mass and evolutionary stage. We use either SNIa W7 (Nomoto *et al.* 1984) to represent a Chandrasekhar explosion or SNIa Hedt (Woosley & Weaver 1994, hedtb11) to represent a sub-Chandrasekhar explosion, depending on which is more likely for each binary scenario. The secondary models are listed in Table 2 with the masses and radii provided. Information on the supernova ejecta models is given in Table 3.

To represent the H CV class, we construct a prototype binary, based on the Type Ia supernova progenitor candidates of Livio & Truran (1992), consisting of a  $1.0 M_{\odot}$  main sequence secondary that lost  $0.1 M_{\odot}$  to a massive  $1.3 M_{\odot}$  white dwarf primary, allowing it to reach the Chandrasekhar mass. Assuming that the binary is in Roche lobe overflow at the time of explosion and that the secondary just fills its Roche lobe, from Eggleton’s relation (Eggleton 1983) for  $q = 1.0/1.4$  we estimate a binary separation of  $\sim 3R$ . For this simulation, we represent the secondary by a  $1.0 M_{\odot}$  solar model (Chaboyer 1998), the exploded white dwarf by the SNIa W7 (Nomoto *et al.* 1984) ejecta profile, and employ a binary separation of  $3R$ .

We use the work of Li & van den Heuvel (1997) on supersoft X-ray sources as Type Ia supernova progenitor candidates to construct sample scenarios for both the H CVL and H Algol classes, one for each candidate proposed by Li & van den Heuvel (1997). Although H CVL binary systems have been included in the past as part of population synthesis studies (Rappaport *et al.* 1994), they are now the subject of renewed interest due to the suggestion by Hachisu *et al.* (1996) that a white dwarf fed by an optically thick wind can experience a much higher mass transfer rate than previously thought. Hachisu *et al.* (1996) have suggested that these binary systems are the progenitors of some supersoft X-ray sources, as well as potential Type Ia supernova progenitors, although the realization frequency is in dispute (Yungelson & Livio 1998).

As prototypes for our H CVL and H Algol classes, we select the two Li & van den Heuvel (1997) scenarios: the first scenario with a  $2.5 M_{\odot}$  subgiant companion and the second with a  $1.0 M_{\odot}$  red giant companion, prior to mass transfer. We represent the subgiant companion just prior to mass transfer with a  $2.1 M_{\odot}$  subgiant star having a radius of  $2.3 R_{\odot}$  (Chaboyer 1998). To simulate the effect of binary mass transfer, which was not included when the star was evolved, we adjust the entropy profile to decrease the mass and radius of our secondary to  $1.13 M_{\odot}$  and  $1.7 R_{\odot}$ , respectively, which reproduces the mass and radius of the secondary at the time of explosion as estimated from Li & van den Heuvel (1997). We do not attempt to reproduce the effect of the mass transfer on the red giant secondary. We represent the red giant companion with a  $0.98 M_{\odot}$  red giant with a radius of  $170 R_{\odot}$  (Chaboyer 1998). Because we can not include binary mass transfer in the stellar evolution code, our stellar models can not be exact recreations of the secondaries used in the binary evolution calculations of Li & van den Heuvel (1997). However, as we shall see, the stripped fraction and the velocity distribution of the stripped material are fairly robust and predictable.



To represent the Symbiotic (SS) class, we construct a prototype system based on the work of Yungelson *et al.* (1995), who concluded that symbiotic systems could be the progenitors of up to 1/3 of Type Ia events in young and intermediate age ( $t \lesssim 6 \times 10^9$  yr) stellar populations. We select the same  $0.98 M_{\odot}$  red giant secondary as in the H Algol case, but to ensure that mass transfer takes place by stellar winds we increase the binary separation so that the red giant could not have filled its Roche lobe. Because these systems are good candidates for Type Ia sub-Chandrasekhar explosions, we select the ejecta model SNIa Hedt (hedtb11, Woosley & Weaver 1994) to represent the exploded white dwarf.

Table 4 lists the key simulations performed for this paper, with the stellar model, supernova ejecta model, and binary separation that were used in each simulation. The four simulations, representing the four hydrogen-rich classes of single-degenerate progenitor models, are labeled after their respective class as HCV, HCVL, HALGOLa, and SYMB. Additional calculations were performed (HCVa, HCVb, HCVc, and HCVd) to gauge the trends with separation in the mass stripped, the kick, and the velocity distribution of the stripped hydrogen. We include a simulation using a  $2.1 M_{\odot}$  subgiant (HCVLa) secondary, which we compare to the HCVL simulation, whose secondary suffered substantial mass loss prior to the supernova explosion.

Our choice of reference binary scenarios is motivated in part by the likelihood that a particular progenitor can be responsible for a significant fraction of Type Ia events, and in part by the desire to cover the range of parameter space likely to be encountered by any Type Ia explosion in a single-degenerate binary system. We expect that the four binary scenarios HCV, HCVL, HALGOLa, and SYMB will cover the basic range of secondary stars, supernova explosion models, and binary separations expected for Type Ia supernova progenitors with a minimum of overlap. For example, the HCV, HCVL, and the HALGOLa simulations represent low-mass main sequence, subgiant, and red giant companions in Roche lobe overflow, in order to cover the range of compactness in the the evolution of a low-mass star. The mass profile of each secondary model is shown in Figure 1, and the binding energy profile is shown in Figure 2. The kinetic energy of the supernova blast is roughly 11, 10, 2300, and 1300 times the binding energy of the secondaries for the HCV, HCVL, HALGOLa, and SYMB simulations, the difference being the large difference in binding energy between the tightly-bound main sequence and subgiants and the loosely-bound envelope of the red giant. To explore the role of the supernova debris profiles, we employ two Type Ia models (see Table 3): W7, a standard Chandrasekhar explosion model, and Hedt, a sub-Chandrasekhar model with 78% of the momentum of W7. The HALGOLa and SYMB simulations represent the red giant companion with the same secondary model, but the HALGOLa simulation represents the supernova ejecta with W7. The SYMB simulation represents the ejecta with Hedt at a slightly greater binary separation. Because the mass transfer is wind-driven, the solid angle subtended by the red giant in the SYMB simulation is therefore slightly smaller. The solid angle subtended determines the fraction of the supernova momentum incident on the secondary. For any low-mass companion in Roche lobe overflow the fraction of the sky subtended is typically  $(1/4)(R/a)^2 \sim 1/36$  because  $a \sim 3R$ , independent of the companion’s stellar type.

#### 4. The Main Sequence Companion

In this section, we describe the impact of the blast wave on a main sequence star, our HCV scenario. As in the subgiant and red giant cases, we neglect any changes to the structure of the star from the Roche potential. Likewise, we do not add an accretion disk, magnetic field, or any other intrinsic features of cataclysmic variables which would introduce complications. For this simulation, we use a  $300(\rho) \times 575(z)$  cylindrical grid with the  $1.0 M_{\odot}$  main sequence secondary, centered on the origin. Approximately  $161(\rho) \times 322(z)$  zones are allocated to the secondary. The grid extends 6 stellar radii in the  $\rho$  direction, 12 stellar radii in the downstream (negative  $z$ ) direction and 2 stellar radii in the upstream (positive  $z$ ) direction. The white dwarf primary explodes just off the grid in the upstream direction, and the supernova debris flows through the upper boundary onto the grid by time-dependent boundary conditions. The density and velocity, which characterize the debris structure, energy, and momentum, are scaled with time: the Eulerian velocity as  $t^{-1}$  and the Lagrangian density as  $t^{-3}$ .

The HCV was run for  $2.0 \times 10^4$  seconds, slightly more than 7 of the companion’s sound crossing times and much longer than the  $1.4 \times 10^3$  seconds that it takes for the trailing edge of the supernova to sweep past the back of the companion. The length of the calculation is chosen to be sufficiently long, and the size of the grid sufficiently large, that we can follow the progress of the shock-heated material ejected from the companion in both velocity and solid angle and can construct a distribution for each. In addition, the long simulation time allows the companion star to begin to reestablish hydrostatic equilibrium. Although we can not follow the companion’s Kelvin-Helmholtz evolution, its post-impact structure may provide us with some insight into the possible consequences of the impact for the companion’s future evolution.

For clarity, this section is subdivided into distinct topics. In §4.1, we describe the debris structure of the impact, and in §4.2 we consider the consequences of the impact for hydrogen burning. In §4.3, we present and describe the stripped mass for this scenario. In §4.4, we qualitatively discuss the possibility that the main sequence companion may accrete supernova material and contaminate its envelope with heavy metals. In §4.5, we discuss the velocity and solid angle distributions of the stripped companion material and possible observational implications. In §4.6, we discuss the kick received by what remains of the companion.

##### 4.1. Hydrodynamics of the Impact on the Main Sequence Companion

The impact of a blast wave on a main sequence star begins a sequence of events common to all supernova-companion interactions. The initial impact of the supernova shell on the surface of the star drives a shock into the stellar envelope. A reverse shock propagates back into the ejecta. A contact discontinuity marks the interface between the supernova ejecta and the shocked stellar material. The shock propagating through the envelope decelerates as it runs up the steep density gradient of the star. After the shock passes through the stellar core, it accelerates down the

decreasing gradient. The shock front, highly curved because of the density gradients, converges in the back of the star. The reverse shock develops into a bow shock around the companion star that smoothly deflects the rest of the incoming supernova debris around the companion. After most of the supernova debris has passed by, the outer layers of the stellar envelope, which have been shock-heated to such an extent that the new speed of sound exceeds the companion’s escape velocity, are ejected, often corrugated by Kelvin-Helmholtz and Rayleigh-Taylor instabilities. The stripped material flows slowly away from the star, embedded within the inner layer of the supernova ejecta. The stellar core expands and cools in response to the initial compression by the shock. The star now has an extended, asymmetrical envelope and begins to pulsate to bring the envelope back into hydrostatic equilibrium. Figures 3 - 4 illustrate the sequence of the interaction in a series of 2-D images from the initial impact to the reestablishment of hydrostatic equilibrium. Figures 5 illustrate the mass stripping of the companion in a series of 2-D cartoon images, with each color indicating the dominant element in that region.

Figure 3a shows the companion centered at the origin of the cylindrical grid at the beginning of the simulation. Figure 3b shows the initial impact of the blast at  $\sim 100$  seconds after the explosion. The supernova ejecta can be seen flowing onto the grid, sweeping up “circumstellar” material as the leading edge begins to flow around the secondary star. There is a region of high pressure at the site of the impact on the companion’s surface where a shock is being driven into the star, and a bow shock is beginning to develop that will divert the flow of the supernova ejecta around the companion. The back of the companion is still undisturbed.

The density variations in the ejecta that are visible as spherical rings in Figure 3b can be directly identified with the density variations in Figure 6 by their velocity. For example, the first strong ring striking the surface of the companion star in Figure 3b has a velocity of  $1.59 \times 10^4$  km s<sup>-1</sup> and can be identified with the first sharp density spike in Figure 6. The second ring has a velocity of  $1.36 \times 10^4$  km s<sup>-1</sup> and can be identified with the second density spike in Figure 6. These features are associated with changes in the composition of the ejecta: the transitions between the “oxygen”, “silicon”, and “iron” layers. (see Figure 5a).

Figure 3c shows the impact 179 seconds after the explosion. The tail shock and bow shock dominate this image. By this time, the collision of the supernova ejecta with the “circumstellar” medium has created a curved shock front which has converged along the downstream axis after flowing around the companion. The shock front reflects at the axis and begins to move outward. The tail shock is visible in Figure 3c as the flared vertical discontinuity along the downstream axis. The upstream axis is dominated by the bow shock which wraps smoothly around the top of the companion, but becomes distorted farther down as a consequence of the impact of the density variations of the ejecta. The material between the bow shock and the shocked surface of the star is primarily supernova debris mixed with “circumstellar” medium. The pressure in this region now rivals the pressure in the interior of the star (see Figure 7).

At 329 seconds (Figure 3d), the shock front passing through the companion has a strong

curvature caused by the density gradient of the star. The center of the shock decelerates as it encounters the rising density near the stellar core, while the wing of the shock accelerates through the back half of the companion where the density is decreasing. The shock-heated envelope of the companion starts to suffer mass loss; escaping material is now visible in the flow that passes around the star behind the bow shock. Kelvin-Helmholtz and Rayleigh-Taylor instabilities in the shocked envelope are just barely visible in this image.

The ejected companion material is confined to a torus around the back of the companion - with the inside of the torus filled with “circumstellar” material that has been compressed behind the companion. There, the flow is almost directly parallel to the downstream axis (see Figure 5c). This material is the first to be ejected from the star and is mixed with the oxygen layer of the supernova debris. This will form the high-velocity tail of the velocity distribution of the stripped companion material. In Figure 5c, the iron shell has expanded to enclose the star, the silicon shell is just below the back of the star, and the oxygen shell is everywhere exterior to the silicon shell. More than 90% of the supernova’s mass and momentum that will collide with the companion is now represented on the grid.

Figures 4a and 4b show the interaction at 529 and 755 seconds after the explosion (see also Figures 5d and 5e). By 529 seconds, the collision is effectively finished. Only a negligible mass and momentum will collide with the companion after this time. The shock within the companion has just passed through the stellar core and will begin to accelerate down the density gradient of the back of the companion. Kelvin-Helmholtz and Rayleigh-Taylor instabilities, the fingers of swirling material in the shocked envelope, are very visible by this time. As yet, only  $0.07 M_{\odot}$  has been ejected. By 755 seconds, the shock within the companion has converged along the downstream axis. In subsequent frames, a reflection shock can be seen progressing back through the remnant of the companion.

Figure 4c shows the end of the mass stripping phase. By 2027 seconds, the star has expanded and pushed the bow shock back towards the site of the explosion. About 93% of the companion’s mass that will be ejected has been ejected by this time. The velocity field around the star is now more spherical. This can be inferred from Figure 5f by the change in the distribution of the stellar hydrogen, which is no longer confined along the downstream axis. About 1000 seconds later, the first in a series of shocks is driven into the envelope marking the beginning of a global stellar pulsation phase.

Figure 4d shows the remnant after three oscillations,  $2 \times 10^4$  seconds after the supernova explosion. The star is almost spherical again, but it is surrounded by a complicated system of shocks. The shock structures can be qualitatively explained in terms of the overtaking of each shock front by the subsequent shock front. Add to this mixture of shocks the reflected shock from the original shock through the companion, and the structure becomes difficult to disentangle.

Exactly what happens to the structure of the companion as the shock is driven through the star? To reliably follow the companion from the impact to the reestablishment of hydrostatic

equilibrium, we ran a slightly different simulation, with the same binary scenario, but with a uniform grid and the gravity solver centered on the center of mass at each timestep, which is more suitable for long simulation times. Figures 7 - 9 show the evolution of the secondary’s pressure profile from the beginning to the end of that simulation. Figure 7 shows the shock climbing the density gradient towards the stellar core. At  $\sim 400$  seconds, the shock passes through the stellar core and begins to descend down the density gradient. Also, as a result of the impact, a reverse shock is formed at the interface between the star and supernova that propagates back into the supernova material. Eventually, the reverse shock becomes the bow shock.

As Taam & Fryxell (1984) discussed in their work on impacts on low-mass main sequence secondaries, the ram pressure of the ejecta is roughly equal to the central pressure of the main sequence secondary. The typical ram pressure of the ejecta is  $P = \rho v^2 \approx M_{ej} v^2 / (4\pi a^3 / 3)$ , (N.B., a  $\sim 3R$  when it hits a low-mass secondary in Roche lobe overflow). For our main sequence simulation this is  $\sim 10^{17}$  dynes  $\text{cm}^{-2}$ , very close to the central pressure of  $2.37 \times 10^{17}$  dynes  $\text{cm}^{-2}$ . The ram pressure of the ejecta is close to the central pressure of the secondary only in the simulation with the main sequence companion. The more evolved subgiant and red giant have larger radii, which increases the binary separation and, thereby, decreases the incoming density and the ram pressure at first impact. For our subgiant and red giant secondaries, the expected ram pressures are roughly  $10^{16}$  and  $10^{10}$  dynes  $\text{cm}^{-2}$ , respectively, which is too low to significantly affect the subgiant’s core by 2 orders of magnitude and the red giant’s core by 7 orders of magnitude. In our HCV calculation, we find that the central pressure changes by a factor of only 2.5 as the shock passes through the core, which makes it a weak shock. The central density rises by only a factor of  $\sim 1.7$ , the temperature by  $\sim 1.5$  and the entropy by  $2.5 \text{ k}_B^{-1}$  baryon $^{-1}$ .

After the initial pressure rise, the star expands and the central pressure begins to drop. The shock accelerates down the density gradient in the back of the star until at  $\sim 700$  seconds it passes through the limb of the star and converges on the downstream axis. Figure 8 illustrates the dramatic pressure rise at the back of the star as the curved shock fronts converge. The high back-pressure exerts a force on the secondary which decreases the kick received from the impact. As part of the shock-heated envelope escapes from the star, the back-pressure drops, until after approximately 2000 seconds, the mass stripping phase is complete and the remainder of the secondary reaches its terminal velocity. At this stage, the star is slowly expanding. However, the passage of the shock and the ejection of part of the envelope begin a phase of radial pulsations during which shocks are sent out through the extended envelope. It is during this phase that the post-impact secondary recovers hydrostatic equilibrium.

Figure 9 shows the pressure profile from the end of the mass stripping phase to the reestablishment of hydrostatic equilibrium. As slow moving material begins to settle back onto the star, a bounce occurs ( $\sim 4000$  seconds) and a shock is driven into the outer envelope. Every 3000 – 4000 seconds, roughly a sound crossing time, another pulsation with a smaller amplitude is seen moving through the extended envelope. Despite the dramatic appearance of the shocks in the extended envelope, little or no mass ejection takes place as a result. As shown in Figure 10,

the stellar core also pulsates, with a period of  $\sim 2600$  seconds. In the last pressure profile shown in Figure 9, the central pressure has stabilized.

The changes in the central pressure, density, temperature, and entropy are listed in Table 5. All quantities but the entropy, which increases by shock-heating, have dropped significantly due to the expansion. Even after the interior of the star stops expanding and the infalling material compresses the core, the central pressure and density are not restored to their original values. Although such pulsations were not noted in earlier numerical simulations, probably due to shorter simulation times, Taam & Fryxell (1984) did find that some of their low-mass main sequence companions suffered an abrupt rise in central density followed by a severe drop as the star began to expand. The density and entropy profiles of the pre- and post-impact companion are shown in Figures 11 and 12. The radius of the remnant star, which we define as the radius that encloses about 90% of the remnant’s mass, is approximately  $7.4 \times 10^5$  km, a modest increase of less than 10%. The remaining 10% of the mass forms a low-density extended envelope out to  $6.7 \times 10^6$  km ( $\sim 10 R_\odot$ ) with a composition similar to that of the original stellar envelope.

#### 4.2. Quenching Hydrogen Burning in the Stellar Core

Do the abrupt rise and fall of the central temperature and density have any unique consequences for the energy generation rate and the luminosity of the companion during the impact? We expect that the energy generation rate, with its extreme temperature sensitivity, should rise and fall dramatically as the stellar core heats and cools. Figure 10 illustrates the rise and fall of the central temperature and density. The oscillations that the secondary experiences as hydrostatic equilibrium is reestablished are visible in both profiles. For a quick estimate of the energy generation rate, we calculate the hydrogen burning rate via the three pp chains and the CNO cycle (Clayton 1983; Kippenhahn & Weigert 1991) along a 1-D cut through the densest (and hottest) part of the companion. As can be seen in Figure 13, the energy generation rate shoots up by a factor of 1000 as a result of shock-heating, then drops precipitously as the star expands. Because the compression phase is so brief, despite the extremely high energy generation rate, only a small amount of additional energy is deposited in the center of the star. For the main sequence star an additional  $\sim 10^{38}$  ergs has been deposited, which is extremely small in comparison with the binding energy of the star ( $\sim 10^{48}$  ergs). However, because the timescale of the compression phase is close to the sound crossing time of the stellar core, the star may be able to expand and cool. Hence,  $10^{38}$  ergs is an upper limit. By the end of the simulation, the energy generation rate is only  $0.07 L_\odot$ . The hydrogen burning has been quenched by the impact. The implications of this are discussed in §9.

### 4.3. The Stripped Mass of the Main Sequence Companion

The amount of mass stripped from the secondaries is shown in Table 6. The third column lists the stripped mass for each scenario based on the numerical calculation and the fourth column lists the stripped mass based on the analytic estimation of Wheeler *et al.* (1975). To determine the amount of material ejected by the impact and the passage of the shock through the star, we compare the velocity of the companion’s material within each zone with its local escape velocity  $\sqrt{2\phi}$ ,  $\phi$  being the gravitational potential. If its velocity exceeds the escape velocity, we consider the mass unbound. If not, we consider the mass bound to the star, only displaced, although, because of the Eulerian nature of the code, we are not able to follow the calculation until the displaced stellar material falls back onto the companion. When any stellar material reaches the edge of the grid, we assume that if it is unbound at that time it will remain unbound. By the end of the simulation,  $0.15 M_{\odot}$  of the main sequence stars’s envelope is unbound, and all but 2.4% of this material has left the grid. Although we run the simulation for  $2 \times 10^4$  seconds, 93% of the stripped mass is ejected in the first  $2 \times 10^3$  seconds, which is longer than the  $1.4 \times 10^3$  seconds for the supernova to pass by the secondary.

In Table 6 we compare the numerical stripped mass with an analytic estimate. The analytic estimate is within 10% of the numerical estimate, surprisingly close, although that changes as the binary separation increases. A detailed comparison of the numerical results with the analytic estimates is in §5. For now, we note that the analytic estimates do provide ballpark estimates of the stripped mass for the main sequence case. Because we use a smaller  $a/R$  ratio, consistent with Roche lobe overflow, our  $0.15 M_{\odot}$  of stripped material is substantially higher than the  $0.013 - 0.052 M_{\odot}$  reported by Fryxell & Arnett (1981). However, we can compare our HCVc simulation to Fryxell & Arnett’s CASE C, which has a similar  $a/R$  ratio, by scaling our stripped mass fraction by the new incident supernova momentum. After the scaling, our  $0.022 M_{\odot}$  of stripped material increases to  $0.057 M_{\odot}$  which is not inconsistent with the  $0.052 M_{\odot}$  they report.

### 4.4. Contamination of the Main Sequence Companion with Supernova Debris

It is possible that some supernova material may be mixed into the envelope of the secondary star, either as a direct consequence of the impact or as fallback. The enhancement of heavy elements in the atmosphere of the secondary star may be observable  $10^3 - 10^4$  years (the Kelvin-Helmholtz timescale) after the impact or might change the course of the secondary’s post-impact Kelvin-Helmholtz evolution by increasing the opacity of the stellar envelope. The question of how much supernova material is likely to be accreted by the secondary star as a direct result of the explosion is of particular interest in connection with the overabundance of  $\alpha$ -elements observed in the atmosphere of the secondary star in Nova Scorpii 1994 (GRO J1655-40) (Israelian *et al.* 1999). This binary X-ray source is believed to consist of a black hole primary in close orbit with a subgiant secondary. Israelian *et al.* (1999) have interpreted the anomalous abundances in

the subgiant’s atmosphere as contamination by fresh nucleosynthesis products ejected during a Type II supernova explosion that might have accompanied the formation of the black hole.

Our calculations imply that the stellar remnant is not contaminated by the supernova material as a direct result of the impact. At the end of our main sequence simulation, no significant amount of supernova material is within the original radius of the secondary. However, a trace amount ( $1.3 \times 10^{-4} M_{\odot}$ ) of supernova material, predominately iron-rich ( $\geq 90\%$ ) is bound by the secondary star, although the only supernova material in the immediate vicinity of the secondary star at the end of the main sequence simulation is physically located exterior to the bow shock. It is possible that the secondary may accrete this low-velocity iron and any additional iron mixed with the marginally-bound companion material when the displaced envelope, which is embedded within the iron layer of the supernova ejecta, begins to fall back. In addition, the slow trailing edge of the supernova ejecta could act as a source of iron-group elements long after the impact.

We can make a ballpark estimate of the amount of supernova debris that can contaminate the secondary star by finding the amount of mass of the supernova ejecta which can not escape the gravitational potential of the secondary. A typical escape velocity for a  $1.0 M_{\odot}$  main sequence star is  $\sim 600 \text{ km s}^{-1}$ . From the supernova ejecta model W7, we find that  $\sim 1.5 \times 10^{-3} M_{\odot}$  has a velocity lower than the escape velocity; we can use this as a crude and conservative upper limit for the degree of contamination.

#### 4.5. Distribution in Velocity and Angle of the Material Stripped from the Main Sequence Companion

One of our key results is the velocity distribution of the stripped hydrogen material, shown in Figure 14a, for the HCV simulation. Also plotted in this figure is the velocity distribution of W7, the supernova ejecta model. The first feature to catch the eye is the clear separation in velocity space between the stripped material and the supernova ejecta. The velocity at the half-mass point in the velocity profile of the main sequence secondary is  $823 \text{ km s}^{-1}$ , much less than the half-mass velocity of the supernova ejecta of  $7836 \text{ km s}^{-1}$ . Each half-mass velocity is marked with a vertical line and an arrow in Figure 14a. The high-velocity tail shows three sharp spikes, which we identify with the three sharp density peaks at the composition transitions in SN W7. The composition groups for both the stripped material and supernova are shown; from this, it is clear that the bulk of the stripped material, predominately hydrogen, is embedded within the iron layer of the supernova ejecta. This result reinforces the belief that contaminating hydrogen and helium are most likely to be observed as late-time emission when the photosphere of the supernova moves to low-velocities, revealing the core. However, a high-velocity tail does exist, implying that a trace of companion hydrogen is swept up in the oxygen and silicon layers of the supernova ejecta. Given the upper limits on the hydrogen abundance from Type Ia observations near maximum light, this may provide a criterion for discriminating between Type Ia progenitor scenarios.

In Figure 14a we correct the low-velocity tail by allowing the stripped material to escape to infinity, free of the secondary’s gravitational potential. If we assume the stripped material flows off



the grid at high-Mach numbers (typically  $M \sim 5 - 30$ ), then the specific enthalpy  $w = c_s^2/(\gamma - 1)$  is small in comparison with the kinetic energy, and we can neglect the enthalpy in Bernoulli's Equation  $w + 1/2v^2 + \phi = C$ , where  $C$  is a constant along a streamline. Therefore, we can estimate the velocity of the flow at infinity as  $v_\infty^2 = v^2 - v_{esc}^2$ . In Figures 14 we have subtracted the escape velocity in quadrature. The subtraction in quadrature affects only the low-velocity tail.

Figures 15 and 16 show the spatial distribution of the stripped mass. Figure 15 illustrates the distribution of the stripped material in solid angle ( $dM/d\Omega$ ) in the HCV simulation, expressed in terms of the angle,  $\alpha$ , from the downstream axis. The half-mass point of the HCV distribution is  $\sim 43^\circ$ , so about half of the stripped material is confined in a cone within about  $\sim 43^\circ$  of the downstream axis and the other half extends out to  $\sim 90^\circ$ . The sudden rise along the axis for the HCV distribution is a consequence of the use of the differential element  $d\Omega = 2\pi \sin \alpha d\alpha$  when  $\alpha \rightarrow 0$ . Figure 16 illustrates the same spatial distribution as a polar plot. The polar angle,  $\alpha$ , once again represents the angle from the downstream axis, and the radial coordinate represents the magnitude of  $dM/d\alpha$ . The profile clearly shows that the preferred direction is along the  $43^\circ$  line. In addition, the majority of the mass is exterior to the geometrical shadow, the shadow that the secondary would cast from the site of the explosion of the primary. Because of the compression of the “circumstellar” material along the downstream axis as the supernova sweeps around the star, very little stripped material is directly behind the secondary. In a 3-D calculation instabilities along the downstream axis are likely to mix the compressed “circumstellar” material with the stripped stellar material, filling in this region.

As shown in Figure 15, the collision of the supernova debris with the secondary will create a hole in the debris structure. The highest velocity debris will flow around the secondary, creating a cut-out region. The lower velocity material will flow around the bow shock, creating a wider hole in the inner ejecta. For the HCV simulation, the supernova debris will have a hole of  $\sim 31^\circ$  in the outer ejecta, which will widen to  $\sim 40^\circ$  in the inner ejecta. This corresponds to 7% and 12% of the surface of the supernova ejecta. Due to the supersonic nature of the flow, the hole will not close with time. Hence, the asymmetry in the supernova remnant may indicate the presence of a secondary star.

If the stripped hydrogen were ejected spherically and uniformly mixed with the (unperturbed) supernova ejecta, then the mass fraction of hydrogen would be 0.6 to 0.7, almost solar, in the low-velocity region ( $\lesssim 10^3 \text{ km s}^{-1}$ ). The hydrogen mass fraction,  $X(\text{H})$ , is shown as a function of supernova mass and velocity in Figures 17 and 18. The hydrogen mass fraction falls abruptly as the velocity increases. At  $10^4 \text{ km s}^{-1}$ , which is near the oxygen and silicon layers,  $X(\text{H}) \sim 3 \times 10^{-3}$ . Of course, we know from the numerical simulation that the ejected material contaminates a wide solid angle behind the secondary. For the HCV simulation, 90% of the stripped hydrogen lies within  $65.7^\circ$  of the downstream axis which corresponds to a fractional solid angle of 29%. Figures 17 and 18 show the expected mass fraction within the contaminated solid angle. As expected, the mass fraction rises dramatically.

#### 4.6. The Kick Received by the Main Sequence Companion

Table 7 lists the kicks given to the remnant companions in the main sequence and subgiant scenarios. We note that the red giant core, because of its extremely small size, receives a negligible kick. We calculate the kick from the supernova impact by finding the terminal velocity of the center of mass of the unstripped stellar material that remains on the grid. Although some material still bound to the star can flow off the grid, it is a negligible fraction ( $\Delta M/M \leq 10^{-2}$ ), since the star reaches its terminal velocity very early in the simulation. For the main sequence simulation HCV, the companion receives a kick of  $\sim 86 \text{ km s}^{-1}$ . Although substantial, this is still much less than its  $227 \text{ km s}^{-1}$  orbital velocity.

In the HCV simulation the terminal velocity is reached by 5000 seconds after the explosion. The secondary receives a very strong kick ( $> 100 \text{ km s}^{-1}$ ) in the first  $\sim 500$  seconds as the shock passes through the center of the companion. As the shock converges and reflects in the back half of the companion ( $\sim 700$  seconds), the pressure rises dramatically, and the companion, now elongated, decelerates. By 1500 seconds, part of the shock-heated envelope has escaped the star and the over-pressure behind the star begins to drop. As the mass-stripping phase nears completion, the companion is almost spherically symmetric and close to its terminal velocity.

Column three in Table 7 provides our ballpark estimate of the kick that we calculate by assuming an inelastic collision in which all the momentum of the supernova ejecta incident on the remnant of the companion is directly transferred to the remnant. That is, using  $\Delta\Omega_{REM}$  and  $M_{REM}$  as the solid angle subtended by the remnant and the mass of the remnant, and  $M_{SN}$  and  $V_{SN}$  as the mass and velocity of the supernova ejecta, respectively, we estimate the kick as  $v \lesssim \Delta\Omega_{REM}M_{SN}V_{SN}/M_{REM}$ . This is clearly an overestimate because not all of the momentum will be directly transferred to the remnant. The momentum transferred to the remnant will depend on the details of the interaction, such as the changing geometrical area as mass loss decreases the surface area of the companion. Our estimate is directly related to the method of Wheeler *et al.* (1975), except that we drop the logarithmic factor because it was concluded (Fryxell & Arnett 1981; Taam & Fryxell 1984) that ablation did not substantially increase the kick.

### 5. Systematic Trends with Binary Separation

To study the effect of changing the binary separation, we performed four test cases with the  $1.0 M_{\odot}$  main sequence secondary in addition to the HCV simulation: HCVa, HCVb, HCVc, and HCVd. The ratio of binary separation to stellar radius ( $a/R$ ) is 2.57, 4.0, 6.0, and 12.0, respectively, with HCV having a ratio of 3.0, making it the second-closest secondary (see Table 4). Because the incident momentum scales as the inverse square of the separation, we expect a significant change in the amount of stripped mass and in the kick. From Tables 6 and 7 we see that over this range of orbital separation the stripped mass varies more than a factor of 100, from  $0.23 M_{\odot}$  to  $0.0018 M_{\odot}$ , and the kick varies by a factor of 9, from  $137 \text{ km s}^{-1}$  to  $15 \text{ km s}^{-1}$ .

Figures 19 visually demonstrate the change in the strength of the impact. In the strongest impact, the companion experiences the strongest initial acceleration, followed by the strongest deceleration as the pressure rises in the back of the star. In the weakest impact, the companion experiences a very weak acceleration, which is not followed by a deceleration phase. In this case, the shock propagating through the companion is too weak to cause a pressure rise in the back of the star. Figures 19 illustrate the decrease in strength of the impacts with a series of 2-D images shown at 1000 – 1300 seconds after the supernova explosion. In the HCV simulation (Figure 19a), the shock has already passed through the companion. The bow shock is broad, within which we see well-developed Kelvin-Helmholtz and Rayleigh-Taylor instabilities trailing behind the companion that indicate mass loss is occurring. In the HCVb simulation (Figure 19b), the interaction is at a comparable phase, except that the shock has just converged behind the star and the trailing instabilities are less developed. In the HCVc simulation (Figure 19c), the shock is still passing through the star and the bow shock is noticeably much narrower than in the stronger impacts. In comparison with the other cases, the impact is almost mild in the HCVd simulation (Figure 19d). Here, the bow shock is very narrow and the shock’s propagation through the star is slow.

We use the separation study to compare our numerical stripped mass and kick with the analytic formulae of Wheeler *et al.* (1975). From Tables 6, 7, and 4 we see that the stripped mass and kick are sensitive functions of  $(a/R)$ . As shown in the tables, the analytic stripped mass usually overestimates the amount of mass loss by 5 – 50% for separations in the range of  $a/R = 3.0 - 4.0$ . For greater separations, the mass loss is severely overestimated. For smaller separations, the mass loss is underestimated. Our analytic estimate of the kick is calculated from simple conservation of momentum and does not include a logarithmic factor to represent an additional kick from ablation. The analytic method consistently overestimates the kick from the impact, by 18% – 47% in the range of our test cases. To conclude, we can say that the analytic estimates of the stripped mass provide a good estimate (within 10%) for binaries near Roche lobe overflow ( $a/R \approx 3$ ), but for closer and farther separations the estimates are substantially in error. Furthermore, the analytic estimates of the kicks provide a ballpark value for all separations, but are systematically high. The kicks are below the orbital velocity of the secondary for all orbital separations.

We can use the separation study to see how the average drag coefficient is likely to depend on the strength of the impact. The efficiency of the transfer of momentum is given by the ratio of stellar remnant momentum to the incident supernova momentum and can be equated to an average drag coefficient (Table 7). Typical coefficients lie in the range of 0.2 – 0.5, rising systematically as the binary separation increases. We note that, as the binary separation increases, less mass is stripped from the companion and its geometrical area does not decrease as much. More of the incident supernova momentum can be intercepted by the remnant. In essence, the average drag rises for impacts in which less material is stripped.

Despite the dramatic change in stripped mass and kick, the characteristic velocity of the stripped material stays between  $855 \text{ km s}^{-1}$  and  $664 \text{ km s}^{-1}$ , with the stripped material from the

closest binaries having the highest characteristic velocities. The half-mass velocities are: 855 km s<sup>-1</sup>, 823 km s<sup>-1</sup>, 778 km s<sup>-1</sup>, 664 km s<sup>-1</sup>, and 730 km s<sup>-1</sup> for the HCVa, HCV, HCVb, HCVc, and HCVd simulations respectively. The fluctuations in the high-velocity end of the velocity distributions seem to reflect the density variations in the initial supernova ejecta model, and like the characteristic velocity, decrease in strength and velocity as the binary separation increases.

We can understand the characteristic velocity by noting that the companion’s shocked material has a specific internal energy equal to its specific kinetic energy, which is determined by the speed of the shock. When the shock is strong, the envelope is heated enough that its new speed of sound exceeds the companion’s escape velocity and the envelope is free to evaporate away from the star. As the shock decelerates, as it will when it climbs the steep density gradient of the star, less specific internal energy is deposited in the envelope and the new speed of sound will be lower. Eventually, the speed of sound will be lower than the escape velocity and the heated material will remain bound to the star. The material that escapes first will be the material shock-heated in the outer layers where most of the energy is deposited; this material will have the highest characteristic velocities. In time, the underlying layers of the envelope will evaporate off, leaving the marginally bound material clinging to the stellar surface. The amount of mass heated to sufficiently high temperatures is less for greater separations.

The closest companions will create the widest plume of stripped material. For an explosion in a close binary with a hydrogen-rich companion, the contaminating hydrogen can fill a solid angle of  $2\pi$  steradians. A companion in a more distant binary will leave a narrower trail of contaminating hydrogen. Figure 20 shows the solid angle distribution plotted as a polar plot, with the radius being the magnitude of  $dM/d\alpha$  and  $\alpha$  once again being the angle from the downstream axis. Clearly, the closer the secondary is to the explosion, the wider in solid angle is the stripped material. The half-mass angles for each distribution range from 10° to 45°. As shown in Figure 20, most of the contaminating hydrogen is exterior to the geometrical shadow. The outer extent of the contamination is related to the amount of mass loss, which as can be seen in Figures 19, is greatest for the strongest impacts.

## 6. The Subgiant Companion

Next, we describe the impact of the blast wave on a subgiant star, our HCVL scenario. As in the main sequence case, we neglect any changes to the structure of the star from the Roche potential or an optically thick wind from the white dwarf which would complicate the simulation. For this simulation we use a  $330(\rho) \times 565(z)$  cylindrical grid with the  $1.13 M_{\odot}$  subgiant secondary centered on the origin. Approximately  $200(\rho) \times 100(z)$  zones are allocated to the secondary. We use the same dimensions relative to the companion’s radius as the main sequence simulation: 6 stellar radii in the  $\rho$  direction, 12 stellar radii in the downstream (negative  $z$ ) direction and 2 stellar radii in the upstream (positive  $z$ ) direction. The same supernova ejecta model (W7) is used and the debris flows onto the grid in the same way. We show time frames of this simulation up to

$2.0 \times 10^4$  seconds, which is longer than the companion’s dynamical time of  $3.5 \times 10^3$  seconds and longer than the  $2.5 \times 10^3$  seconds that it takes for the trailing edge of the supernova to sweep past the back of the companion.

For clarity, this section is subdivided into distinct topics. In §6.1 we describe the hydrodynamic stages of the impact and in §6.2 we describe the stripped mass for this scenario. In §6.3, we discuss the velocity and solid angle distributions of the stripped companion material and the observational implications. Finally, in §6.4, we discuss the kick received by the remnant of the companion. To avoid repetition, we focus only on the important differences between the main sequence and subgiant simulations.

### 6.1. Hydrodynamics of the Impact on the Subgiant Companion

The impact of the supernova W7 on the subgiant follows the same sequence of events as the impact on the main sequence star. The subgiant subtends almost the same solid angle as the main sequence star (see Table 4), so the incident momentum is almost the same in both simulations. Given this, it is not surprising that the character of the impact has not changed. However, because of the increase in physical scale, which goes as the radius of the companion star, the sequence of events occurs at slightly different times. Also, the compact core of the subgiant alters the progress of the shock through the star, and the larger envelope increases the timescale required to bring the remnant back into hydrostatic equilibrium. The highlights of the impact on the subgiant are shown in several 2-D images in Figures 21 and 22.

Figure 21a shows the impact of the supernova ejecta on the subgiant 343 seconds after the explosion. The leading shock front preceding the ejecta has converged along the downstream axis. The density jumps in the ejecta that are visible as spherical rings have already distorted the bow shock. More than 90% of the supernova’s mass and momentum that will collide with the subgiant is now represented on the grid. At this early stage, only  $0.06 M_{\odot}$  of the secondary’s envelope has been stripped and the stripped material is still in close proximity to the secondary.

Figure 21b illustrates the curvature of the shock front at 945 seconds. As with the main sequence companion, the shock front driven through the center of the subgiant decelerates as it nears the subgiant’s tightly-bound core. The shock front driven into the outer envelope propagates so much faster that it converges on the downstream axis just after the stellar core is shocked. As with the main sequence companion, a reflection shock passes back through the subgiant.

By Figure 21c, 2044 seconds after the explosion, the supernova shell has swept by the secondary. Shock-heated material can be seen streaming from the subgiant within the cavity shaped by the bow shock. By this time,  $0.15 M_{\odot}$  of stellar material has been stripped. The Rayleigh-Taylor and Kelvin-Helmholtz instabilities can be seen easily in Figure 22.

At  $2 \times 10^4$  seconds (Figure 21d), the companion is beginning to recover hydrostatic

equilibrium. Like the main sequence companion, the star is surrounded by an extended envelope of low-density material. A complicated series of shocks formed during the stellar pulsation phase are propagating slowly through the outer envelope. By this time,  $0.17 M_{\odot}$  has been stripped and the subgiant has received a kick of  $49 \text{ km s}^{-1}$  from the impact.

The pressure and density of the subgiant fluctuate in the same way as in the main sequence case. The central pressure first rises rapidly as the shock passes through the stellar core at  $600 - 700$  seconds, then slowly falls as the star expands. As in the main sequence impact, the material which is now only marginally bound begins to collapse back onto the subgiant and at  $\sim 4000$  seconds a shock is transmitted into the outer envelope. A pulsation phase follows.

The density and entropy profiles for the pre- and post-impact subgiant are shown in Figures 11 and 12. The radius of the remnant star, which we define as the radius that encloses about 90% of the remnant’s mass, is  $\sim 0.9 R_{\odot}$ , which is a decrease of 48%. The remaining 10% of the mass forms a low-density extended envelope out to  $5.9 \times 10^6 \text{ km}$  ( $\sim 8 R_{\odot}$ ).

## 6.2. The Stripped Mass of the Subgiant Companion

We determine the amount of mass stripped in the same way we did for the main sequence case and list it in Table 6. We include the mass stripped for two subgiant scenarios: HCVL and HCVL<sub>a</sub>. The HCVL binary scenario uses a  $1.13 M_{\odot}$  subgiant which was created from a  $2.1 M_{\odot}$  subgiant that was artificially stripped of its outer envelope to coarsely mimic mass transfer prior to the supernova explosion. The HCVL<sub>a</sub> binary scenario uses the original  $2.1 M_{\odot}$  subgiant with a slightly larger binary separation so that the same solid angle is subtended in order to ensure that both secondaries receive the same incident momentum from the blast. This scenario was included only as a test case. At the end of the HCVL simulation,  $3 \times 10^4$  seconds after the supernova explosion ( $\sim 5$  sound crossing times),  $0.17 M_{\odot}$  of stellar material has become unbound, and of this material, about 97% has left the grid by the last timestep. The mass-stripping phase lasts roughly  $3.7 \times 10^3$  seconds, long enough for 96% for the mass that will be stripped by the end of the simulation to be stripped, and much longer than the  $2.5 \times 10^3$  seconds required for passage of the supernova blast around the secondary. In comparison, the original  $2.1 M_{\odot}$  subgiant in the HCVL<sub>a</sub> simulation loses  $0.25 M_{\odot}$ .

Table 6 compares the numerical stripped mass with an analytic estimate. The analytic calculation, which underestimates the stripped mass for both the HCVL and HCVL<sub>a</sub> simulations, is nonetheless within 22% of the numerical result. We ran the HCVL<sub>a</sub> simulation as a test case to see if the stripped mass scales directly with the companion’s mass for the same subtended solid angle. We find that the mass loss scales almost directly with the mass of the companion. That is, the  $2.1 M_{\odot}$  subgiant loses  $0.25 M_{\odot}$ , which is 12% of its mass. In comparison, the  $1.13 M_{\odot}$  subgiant loses  $0.17 M_{\odot}$ , which is 15% of its mass.

### 6.3. Distribution in Velocity and Angle of the Material Stripped from the Subgiant Companion

Our key result for the subgiant simulation is the velocity distribution of the stripped hydrogen, shown in Figure 14b with the SN W7 velocity distribution. The velocity profile of the material stripped from the subgiant shows many of the same features seen in the main sequence star simulation. The half-mass point for the subgiant is just slightly faster:  $890 \text{ km s}^{-1}$  compared with  $820 \text{ km s}^{-1}$  for the main sequence case. Both characteristic velocities are much less than the half-mass velocity of the supernova ejecta of  $7836 \text{ km s}^{-1}$ . Figure 14b marks the characteristic velocities with a vertical line and an arrow. As in the main sequence case, the bulk of the stripped material, predominately hydrogen and helium, is embedded within the iron layer of the supernova ejecta. Once again, a high-velocity tail exists which implies that a trace of companion hydrogen is swept up into the oxygen and silicon layers of the supernova ejecta.

The differences between the main sequence and subgiant can be seen in Figures 14, which shows the asymptotic velocity profile. As discussed in §4.5, we subtract in quadrature an estimate for the local escape velocity that was used to distinguish between the stripped and the unstripped material. This approximates the velocity profile at infinity, when the stripped material is free of the secondary’s gravitational potential. The velocity profile of the mass stripped from the subgiant companion shows a subtle shift to higher velocities, and the high-velocity tail shows a single peak near  $3 \times 10^3 \text{ km s}^{-1}$ . The velocity profile of mass stripped from the main sequence companion shows three peaks, which we identify with the three composition transitions in the W7 model; the other two peaks in the mass stripped from the subgiant are not clearly distinguishable.

Just as the velocity profile of the subgiant’s stripped material is very similar to the velocity profile of the main sequence star’s stripped material, the spatial distribution of the subgiant’s stripped material shows a strong similarity to that in the main sequence case. Figure 15 illustrates the distribution in solid angle ( $dM/d\Omega$ ) of the stripped material in the HCVL and HCV simulations, expressed in terms of the angle,  $\alpha$ , from the downstream axis. The half-mass point of the HCVL distribution is  $\sim 49^\circ$ , just slightly more extended in angle than in the main sequence case, which has a half-mass angle of  $43^\circ$ . In Figure 16, the polar angle,  $\alpha$ , once again represents the angle from the downstream axis and the radial coordinate represents the magnitude of  $dM/d\alpha$ . The material stripped from the subgiant and the main sequence companions fills almost the same cone, with the subgiant filling in a slightly broader one. Once again, the majority of the stripped mass is exterior to the geometrical shadow, the shadow that the secondary would cast from the site of the explosion of the primary. The collision of the supernova debris with the subgiant secondary will create a hole in the debris structure of  $\sim 32^\circ$  in the high-velocity ejecta and of  $\sim 40^\circ$  in the low-velocity ejecta. The asymmetry of the supernova ejecta will be slightly larger at the highest velocities for the subgiant model than the main sequence model. The asymmetry at low velocities will be almost the same for both models. As in the main sequence model, the asymmetry of the supernova ejecta is a direct indication of the presence of a companion star.

The hydrogen mass fraction is shown as a function of supernova mass and velocity in Figures 23 and 24. The hydrogen mass fraction falls abruptly as the velocity increases. At  $10^4$  km s<sup>-1</sup>, which is near the oxygen and silicon layers,  $X(\text{H}) \sim 3 \times 10^{-3}$ . Of course, we know from the numerical simulation that the ejected material contaminates a wide solid angle behind the secondary. For the HCVL simulation, 90% of the stripped hydrogen lies within  $72.5^\circ$  of the downstream axis, which corresponds to a fractional solid angle of 35%. Figures 23 and 24 show the expected mass fraction within the contaminated solid angle. As expected, the mass fraction rises dramatically. Of course, if the subgiant were of higher mass, then the hydrogen mass fraction in the supernova ejecta will rise accordingly. A higher mass secondary may be physically reasonable because our subgiant was initially  $2.1 M_\odot$  before its envelope was modified to mimic mass transfer prior to explosion.

#### 6.4. The Kick Received by the Subgiant Companion

The net kicks for the HCVL and HCVLa subgiant scenarios are listed in Table 7 along with the kicks for the main sequence companions. For the HCVL simulation, we see the same qualitative behavior as in the main sequence simulations. The secondary receives a strong kick in the first 700 seconds after the explosion. A brief period of deceleration occurs until  $\sim 1700$  seconds, and the secondary is left with a terminal velocity of  $49$  km s<sup>-1</sup> by 4000 seconds. The numerical velocity is only 70% of the analytic value of  $70$  km s<sup>-1</sup>.

### 7. The Red Giant Companion

In this section, we describe the impact of a blast wave with a red giant star, our HALGOLa and SYMB scenarios. These scenarios differ in the explosion model and binary separation (see Table 4). The SYMB scenario has a slightly larger binary separation because the mass transfer is by wind accretion, and its white dwarf primary explodes as a sub-Chandrasekhar Type Ia. The HALGOLa scenario has a binary separation consistent with Roche lobe overflow, and its white dwarf explodes as a Chandrasekhar Type Ia. We use the same  $0.98 M_\odot$  red giant model for both simulations. As in the main sequence and subgiant cases, we neglect any complicating changes to the structure of the envelope from the Roche potential.

We change to spherical coordinates for all the red giant simulations. The grid extends 12 stellar radii and  $\pi$  radians. We use  $585(r) \times 300(\theta)$  zones for the HALGOLa simulations and  $653(r) \times 300(\theta)$  zones for the SYMB simulation, with  $242(r) \times 300(\theta)$  and  $247(r) \times 300(\theta)$  zones reserved for the red giant’s envelope. The slight difference in the number of zones results from changing the grid to accommodate the different density and velocity profiles of the SN W7 (Nomoto *et al.* 1984) and SN Hedt (Woosley & Weaver 1994) ejecta models. We run the SYMB simulation for  $8.0 \times 10^6$  seconds and the HALGOLa simulation for  $6.0 \times 10^6$  seconds, which is



only slightly more than one dynamical time, but still plenty of time for the stripped material to flow off the hydrodynamic grid. Because the loosely-bound envelope of the red giant is almost entirely stripped by the impact, there is no need to extend the calculation any further. We will concentrate on the SYMB simulation in this discussion, but will point out differences with the HALGOLa scenario when appropriate.

For clarity, this section is subdivided into distinct topics. Section 7.1 describes the character of the impact and §7.2 discusses the stripped mass for this scenario. In §7.3, the velocity and solid angle distributions of the stripped companion material and the observational implications are discussed. We focus only on the important differences with the main sequence and subgiant simulations discussed earlier.

### 7.1. Hydrodynamics of the Impact on the Red Giant Companion

Because of the lower binding energy of the envelope of the red giant (Figure 2), the impact of the supernova on the red giant companion is much more dramatic than the impact on the main sequence and subgiant companions. Unlike the main sequence and subgiant secondaries, the incident kinetic energy ( $\sim 10^{49}$  ergs) is over 1000 times the envelope binding energy ( $\sim 10^{46}$  ergs). The catastrophic effect of the blast on the weakly-bound envelope was pointed out by a number of authors (cf. Wheeler *et al.* 1975; Chugai 1986; Applegate & Terman 1989) and demonstrated numerically by Livne *et al.* (1992). Our simulations confirm the basic result of Livne *et al.* (1992): the envelope of the red giant is stripped and the velocity of the stripped material is less than  $10^3$  km s $^{-1}$ . The half-mass point of our velocity distribution is 600 km s $^{-1}$ . Like Livne *et al.* (1992), we select a binary scenario with the red giant close enough to the white dwarf to be in Roche lobe overflow, our HALGOLa, and a scenario with a slightly larger binary separation, our SYMB. Unlike Livne *et al.* (1992), instead of a parameterized debris model, we use supernova Type Ia W7 for the blast for the HALGOLa and Type Ia sub-Chandrasekhar Hedt for the SYMB (Table 3). Figures 25 and 26 show highlights of the destruction of the red giant’s envelope in a series of 2-D images from the SYMB simulation. However, Figures 25 focus on the propagation of the shock through the envelope, while Figures 26 show the entire grid.

To start the simulation, the red giant is centered at the origin, and the density and velocity profiles of the exploding white dwarf, scaled to 1.73 hours after the explosion, are positioned along the upstream axis. The impact begins at  $\sim 3.0$  hours after the explosion. Figures 25a and 26a show the interaction 5.67 hours later, at 8.68 hours after the explosion. The initial impact has driven a shock into the companion. The shock front in the “circumstellar” medium joins smoothly with the shock propagating through the red giant’s envelope. The supernova material has not yet converged on the downstream axis.

By 14.23 hours, the bow shock has formed and the supernova ejecta have converged on the downstream axis right behind the star (Figures 25b and 26b). The shock passing through the

companion is extremely curved. Kelvin-Helmholtz and Rayleigh-Taylor instabilities are clearly visible in the shock-heated material. The faint line of low-density material that is along the upstream axis and just outside the bow shock is a numerical artifact caused by the reflecting boundary.

After 2.10 days (Figures 25c and 26c), the shock moving through the envelope converges in the back of the star. The entire star has been shocked, and almost the entire envelope has now been stripped down to the degenerate core. The slight distortion of the bow shock is due to the numerical artifact along the upstream axis. A reflection shock will soon be created that will pass back through the star.

By 5.86 days, pressure behind the bow shock has pushed it back towards the site of the explosion (Figure 25d and 26d). Although the velocity of the stripped material near the core is almost spherical, the bulk of the stripped material is moving downstream. In this simulation the bow shock is showing distortions as the density drops in the post-shock region. At this point, we regrid to increase the timestep and continue the simulation for an additional  $\sim 86.7$  days, or 92.6 days after the explosion, which is time enough for  $\sim 85\%$  of the stripped material to flow off the grid. Only a trace amount of material, at most 4% of the original envelope ( $\sim 0.02 M_{\odot}$ ), is left clinging to the degenerate core.

Unlike the main sequence and subgiant companions, which are done in cylindrical coordinates with the supernova debris added to the grid by the boundary conditions, the red giant simulations require the density and velocity profiles to be placed directly on the grid, off-center, as part of the initial conditions. The supersonic flow must propagate across radial lines and maintain its spherical structure. Figures 26 show that the spherical structure of the debris is maintained. But does placing the spherical explosion off-center have any consequences for the amount of stripped mass or the velocity distribution? To test this and to address a concern that the numerical artifact along the axis might have unexpected consequences, we inverted the position of the supernova and the secondary for the HALGOLa simulation. Although there are small differences between the two simulations, in both cases over  $0.54 M_{\odot}$  of the red giant’s envelope is ejected by the blast. For the original HALGOLa simulation the half-mass point of the velocity distribution of the stripped material is  $593 \text{ km s}^{-1}$ , and for the inverted simulation the half-mass velocity is  $584 \text{ km s}^{-1}$ .

After the red giant’s envelope is ejected, the degenerate core, now a single low-mass He pre-white dwarf, is left surrounded by a hot, entropized atmosphere. Although the blast strips most of the envelope, a small residual fraction (a few percent) may form an extended, hydrogen-rich envelope around the star. Although about  $\sim 75\%$  of this envelope is within  $4.4 \times 10^7 \text{ km}$  and has typical temperatures of  $10^4 - 10^5 \text{ K}$ , the remaining  $\sim 25\%$  is cooling adiabatically, and extends out as far as  $2.4 \times 10^8 \text{ km}$ . Typical entropies in the envelope are  $35 - 40$  in units of  $\text{k}_B^{-1} \text{ baryon}^{-1}$ . In time, this extended envelope will settle onto the star, adding  $\sim 0.02 M_{\odot}$  of hydrogen-rich material to the hydrogen burning layer. We speculate on the fate of the low-mass He pre-white dwarf in §9.

## 7.2. The Stripped Mass of the Red Giant Companion

We determine the mass lost in the same way we did for the main sequence and the subgiant cases. The stripped mass for the red giant simulations is shown in Table 6 with the results from the other simulations. Like Livne *et al.* (1992), we find that almost the entire envelope is removed by the impact, for all the red giant binary scenarios. For the HALGOLa simulation, the mass-stripping phase lasts roughly  $10^5$  seconds (or 1.2 days). After  $6.0 \times 10^6$  seconds (or 69.5 days),  $0.54 M_{\odot}$  (98% of the stellar envelope) of stellar material has become unbound, and of this material, about 85% has left the grid. The stripped mass for the SYMB simulation is similar. The mass-stripping phase for the SYMB simulation lasts roughly  $1.3 \times 10^5$  seconds (or 1.5 days). After  $8.0 \times 10^6$  seconds (or 92.6 days),  $0.53 M_{\odot}$  (96% of the stellar envelope) of stellar material has become unbound, and of this material about 85% has left the grid.

## 7.3. Distribution in Velocity and Angle of the Material Stripped from the Red Giant Companion

Figures 27 show the velocity distribution of the stripped envelopes; both are shown with the original velocity distribution of the supernova ejecta, W7 for the HALGOLa simulation and Hedt for the SYMB simulation. The velocity distributions from the red giant simulations, which have the same basic shape as the distributions from the main sequence and subgiant simulations, have systematically shifted to lower velocities. The half-mass velocity of HALGOLa is  $593 \text{ km s}^{-1}$  compared with  $421 \text{ km s}^{-1}$  for the SYMB case.

Because the Hedt debris profile has only 78% of the momentum of the W7 profile, we expect the SYMB scenario to have a lower characteristic velocity. In fact, the SYMB stripped material has a half-mass velocity of 71% of the HALGOLa case. However, the SYMB scenario has a slightly greater separation. By repeating the SYMB simulation with the same binary separation as the HALGOLa simulation, we find that the solid angle distribution remains almost unchanged, but the new velocity profile is almost, but not quite, identical to the HALGOLa profile. As in the HALGOLa distribution, the new half-mass velocity is  $593 \text{ km s}^{-1}$ . The only distinct difference between the velocity profiles is the slight bump in the high-velocity tail (near  $\sim 3.0 \times 10^3 \text{ km s}^{-1}$  in Figures 27), which is visible in the HALGOLa case and not visible in either the old or the new SYMB case. We conclude from this that the slight increase in the high-velocity tail reflects the different supernova ejecta models used and that the shift to lower velocities in the SYMB case reflects the slightly greater binary separation.

The solid angle distribution for both of the red giant scenarios is shown in Figure 28 and as a polar plot in Figure 29. Although the  $dM/d\Omega$  profiles appear to be rising along the downstream axis, the amount of mass ejected in that direction is actually less than would be expected if the envelope had been uniformly stripped. In fact, the half-mass angles are  $61^\circ$  and  $66^\circ$ , with that for the SYMB scenario being slightly more extended. As in the main sequence and subgiant cases,

the majority of the stripped mass is exterior to the solid angle enclosed by the geometrical shadow of the secondary as seen from the site of the explosion. In addition, there is now a substantial amount of mass that has been ejected past the  $90^\circ$  point.

The impact of the supernova ejecta onto the secondary creates a hole in the supernova debris (Figure 28). For the HALGOLa model, the supernova debris has a hole of  $\sim 34^\circ$  in the outer ejecta, which widens to  $\sim 40^\circ$  in the inner ejecta. This corresponds to 9% – 12% of the surface of the ejecta. The SYMB model has a slightly smaller hole of  $\sim 32^\circ$  in the outer ejecta, which widens to  $\sim 37^\circ$  in the inner ejecta. This corresponds to 8% – 12% of the surface of the ejecta. The HALGOL model clearly creates more asymmetry in the supernova ejecta at the highest velocities than the SYMB model or the main sequence and subgiant models.

Figures 30 and 31 illustrate  $X(\text{H})$ , the hydrogen mass fraction in the contaminated supernova ejecta (assuming uniform angular mixing in the unperturbed supernova model) for the HALGOLa scenario.  $X(\text{H})$  is generally higher in the red giant simulations than in the main sequence or subgiant simulations simply because of the larger mass ejected. However, because most of the hydrogen stripped from the red giant is at lower velocities, for the red giant case the hydrogen mass fraction at high velocities is slightly lower than in the main sequence and subgiant cases in that  $X(\text{H}) \sim 2 \times 10^{-3}$  at velocities of  $10^4 \text{ km s}^{-1}$ , compared with  $X(\text{H}) \sim 3 \times 10^{-3}$  for the main sequence and subgiant cases. If we constrain the mixing to just the contaminated solid angle behind the secondary,  $X(\text{H})$  does rise, but not dramatically, because the contaminated solid angle is now so much larger that this correction becomes small. For the HALGOLa simulation, 90% of the stripped hydrogen lies within  $115.4^\circ$  of the downstream axis which corresponds to a fractional solid angle of 71%.

## 8. Upper Limit on High-Velocity Hydrogen

Ideally, we would like a firm upper limit on the amount of hydrogen that can be mixed with the supernova debris at high and low velocities without being detected in the spectrum. The low-velocity upper limit requires a non-LTE radiative transfer study (Pinto *et al.* 1999). For the high-velocity upper limit we can use upper limits from Type Ia observations near maximum light. Although most of the stripped material is ejected at low velocities, for all the binary scenarios we have considered, there is a small high-velocity tail, as shown in Figure 32. In Table 8, selected points are tabulated. We present the velocity distribution as the total amount of hydrogen exterior to each velocity.<sup>4</sup>

Above  $3.0 \times 10^3 \text{ km s}^{-1}$ , the left-hand edge of Figure 32, all four scenarios have less than

---

<sup>4</sup> In §2, we discuss the effect of resolution on the high-velocity profile. In the HCV simulation there is 15% more mass above  $3 \times 10^3 \text{ km s}^{-1}$  and 26% less mass above  $1.5 \times 10^4 \text{ km s}^{-1}$  than in the high-resolution simulation. Hence, at the higher velocities we conclude that changes in mass greater than  $\sim 30\%$  are meaningful.

$\sim 0.014 M_{\odot}$  of high-velocity hydrogen. The HCVL simulation has  $0.014 M_{\odot}$ , followed by the HALGOLa with  $0.012 M_{\odot}$ , the HCV with  $0.010 M_{\odot}$ , and lastly, the SYMB simulation with only  $0.004 M_{\odot}$ . By  $10^4 \text{ km s}^{-1}$ , the amount of high-velocity hydrogen for all four scenarios has dropped by almost a factor of 10. The HCVL, HCV, and the HALGOLa scenarios are very similar up to this velocity. Because of the greater binary separation and smaller impact momentum and energy, the SYMB scenario has less than half the hydrogen of the other scenarios. When the SYMB scenario has the same binary separation as the HALGOLa scenario, it too has a velocity distribution like the others in this range ( $3 \times 10^3 - 10^4 \text{ km s}^{-1}$ ). It would be difficult to discriminate between the main sequence, the subgiant, and the HALGOLa red giant scenarios in this velocity range. However, we can easily discriminate between the companions in Roche lobe overflow and a model in which the red giant that is too distant to be in Roche lobe overflow, our SYMB scenario.

For  $1.5 \times 10^4 \text{ km s}^{-1}$ , the HALGOLa and the SYMB scenarios have the most high-velocity hydrogen, the HALGOLa with  $3.3 \times 10^{-4} M_{\odot}$  and the SYMB with  $3.0 \times 10^{-4} M_{\odot}$ . In Figure 32, the hydrogen distribution for the SYMB and HALGOLa scenarios converge at higher velocities, implying that the HALGOLa and the SYMB scenarios have almost the same amount of hydrogen at the highest velocities. We attribute this convergence to the momentum profile of Hedt (sub-Chandrasekhar model), which has more overall momentum at velocities greater than  $1.5 \times 10^4 \text{ km s}^{-1}$  than SN W7 (Chandrasekhar model) (Figure 6). We note that the amount of high-velocity hydrogen above  $1.5 \times 10^4 \text{ km s}^{-1}$  could be a direct indicator of the momentum profile of the supernova ejecta at the highest velocities.

Above  $1.5 \times 10^4 \text{ km s}^{-1}$ , the HCVL and HCV scenarios have much less high-velocity hydrogen than in the red giant scenarios. The HCVL scenario has only  $1.7 \times 10^{-4} M_{\odot}$ , which is only 53% of the high-velocity hydrogen of HALGOLa. The HCV has even less, only  $1.3 \times 10^{-4} M_{\odot}$ . We note that even if the red giant companions have more low-velocity hydrogen, they have more hydrogen above  $1.5 \times 10^4 \text{ km s}^{-1}$  than the main sequence or subgiant models. Because the HCVL has more high-velocity hydrogen than the HCV scenario, in principle we can discriminate between the subgiant and main sequence companion at  $1.5 \times 10^4 \text{ km s}^{-1}$ .

The upper limit of  $\text{H/Si} \leq 2.0 \times 10^{-6}$  (relative to solar) from SN 1990M, which, assuming perfect mixing of the silicon in an ejecta profile like W7, corresponds to a total hydrogen mass of  $\sim 3 \times 10^{-4} M_{\odot}$  (Della Valle *et al.* 1996) and is indicated by a horizontal line in Figure 32. Because Della Valle *et al.* (1996) estimated the error in the upper limit to be a factor of 2 – 3, we also include horizontal lines to indicate this range. The vertical line indicates the velocity in SN Ia W7 that corresponds to the outer  $0.04 M_{\odot}$  of the ejecta, which they estimated to be the mass in the photosphere at the time of the observations. If  $3 \times 10^{-4} M_{\odot}$  is a reasonable upper limit to the total amount of hydrogen, and if it is mixed only within the observable photosphere, then we can compare our mass profiles with this upper limit at the edge of the observable photosphere. We see from the figure that none of the binary scenarios we have considered exceeds this upper limit. However, if the upper limit were reduced by only a factor of 3, the red giant and subgiant

models would clearly exceed this limit, while the main sequence model is marginal. Because the supernova photosphere is non-LTE and the upper limit of Della Valle *et al.* (1996) is based on an LTE atmosphere, the hydrogen abundance in the supernova could be much higher than their upper limit indicates.

## 9. The Future of the Companion Star

The post-impact evolution of the main sequence and subgiant secondaries is a separate calculation requiring a 2-D stellar evolution code that is capable of handling initial models that are slightly asymmetric in density and temperature and completely out of thermal equilibrium. For example, although the main sequence star is recovering hydrostatic equilibrium by the end of the simulation, the density in the outer envelope of the star still varies by as much as a factor of 2 in different directions. The temperature and entropy profiles are also highly asymmetric, reflecting the shock history of the impact. Without attempting to follow the secondary’s post-impact evolution in detail, we can only speculate about the secondary’s future evolution.

Immediately after the impact, the main sequence star is puffed up, much like a pre-main sequence star. Although the nuclear energy generation in the core has been extinguished, the luminosity of the residue will be dramatically brighter for this extended envelope that is out of thermal equilibrium. Chaboyer (1998) estimated that with the asymmetrical temperature distribution the luminosity could vary from  $500 L_{\odot}$  to  $5000 L_{\odot}$  after the impact, with a Kelvin-Helmholtz timescale of 1400 years to 11000 years. After thermal equilibrium is reestablished, the remnant will return to the main sequence along a Kelvin-Helmholtz track and then will continue its evolution at a rate prescribed by its new mass. Without mixing in the stellar core to refresh the hydrogen supply, the born-again star will appear near the middle of its main sequence lifetime. Using the main sequence relations  $R \propto M^{2/3}$  and  $L \propto M^5$ , the  $1.0 M_{\odot}$  main sequence secondary will eventually return to the main sequence with a mass of  $0.85 M_{\odot}$  (having lost  $0.15 M_{\odot}$  by the impact), with a slightly smaller radius of  $0.9 R_{\odot}$ , and a luminosity near  $0.4 L_{\odot}$ .

The subgiant puffs up after the impact and must contract to re-ignite hydrogen shell-burning, which will have been extinguished during the subgiant’s expansion. As in the main sequence case, the luminosity will be extremely high during this phase. After thermal equilibrium is established and burning is reignited, the star will be back on a post-main sequence track with a slightly lower luminosity.

After the red giant’s envelope is stripped by the impact of the supernova, the degenerate core, now a single low-mass He pre-white dwarf, is left surrounded by a hot, entropized hydrogen/helium atmosphere. The structure of the core is only minimally affected by the impact because the converging shock was weakened by the extremely strong pressure and density gradients in the interior of the red giant. Although the blast strips most of the envelope, a small residual fraction ( $\sim 0.02 M_{\odot}$ ) may form an extended, hydrogen-rich envelope. Although the impact may

temporarily disrupt the hydrogen-burning layer, it is possible that the star may recommence shell burning as the envelope settles back down into a thin layer. As the degenerate core and hydrogen-rich envelope contracts, the star will evolve away from the red giant branch, along a track of constant luminosity ( $\sim 10^3 L_\odot$ ) and rising effective temperature on a timescale of  $10^5 - 10^6$  years for a  $0.42 M_\odot$  He core (Iben & Tutukov 1986; Iben & Livio 1993; Iben & Tutukov 1993). After the effective temperature rises to greater than  $\sim 3 \times 10^4$ K, the star may appear as an underluminous main sequence O or B star. At the end of the contraction phase, the luminosity begins to drop. When the luminosity drops to  $\sim 10 L_\odot$ , it will appear as a subluminous hot star; an sdO star if the temperature exceeds  $3.5 \times 10^4$ K or an sdB star if it does not (Iben & Livio 1993; Green 1999). The star will then continue to cool along a standard He white dwarf cooling track (Benvenuto 1999). This scenario could be a possible pathway for the formation of a subset of single, low-mass He white dwarfs.

## 10. Summary and Conclusions

In this paper, we have presented numerous hydrodynamic simulations of the impact of a Type Ia supernova explosion with hydrogen-rich main sequence, subgiant, and red giant companions. The binary parameters were chosen to represent several classes of single-degenerate Type Ia progenitor models that have been suggested in the literature. All of the simulations involved low-mass ( $1.0 - 2.0 M_\odot$ ) companions that are close enough, or almost close enough, to be in Roche lobe overflow when the white dwarf primary explodes.

We described the supernova-secondary interaction for a main sequence, subgiant, and red giant companions with 2-D illustrations from the simulations. The collision follows the same basic pattern for the main sequence and subgiant because of their similar structure. The initial impact of the supernova shell with the surface of the main sequence star drives a shockwave into the stellar envelope. A reverse shock propagates back into the ejecta. A contact discontinuity marks the interface between the supernova ejecta and the shocked stellar material. The shock propagating through the stellar envelope decelerates as it runs up the steep stellar density gradient. The shock front, highly curved because of the density gradients, converges in the back of the star. A bow shock develops in front of the companion star. After most of the supernova debris has passed by, the outer layers of the stellar envelope are ejected because they have been shock-heated to such an extent that the new speed of sound exceeds the companion’s escape velocity. Kelvin-Helmholtz and Rayleigh-Taylor instabilities are very visible at this stage. The outer shocked material evaporates away from the star, embedded within the inner layer of the supernova ejecta. The stellar core expands and cools in response to the compression by the shock’s passage through the core. The star has an extended, asymmetrical envelope and begins to pulsate as it settles back into hydrostatic equilibrium.

The subgiant follows a similar sequence, except that its more compact core alters the progress of the shock through the star and its larger envelope increases the timescale required to bring

the remnant back into hydrostatic equilibrium. Because of its weakly-bound envelope, the impact on the red giant is quite different. The shock propagates through its more tenuous envelope and converges on its rearward side. All but a small fraction of the entire envelope is ejected, leaving a He pre-white dwarf surrounded by a halo of high-entropy hydrogen and helium.

We can summarize our results by stating that as a result of the impact of the supernova shell the main sequence companion loses  $0.15 M_{\odot}$  and the subgiant companion loses  $0.17 M_{\odot}$ . In contrast, the red giant companions lose almost their entire envelopes, at least  $0.53 M_{\odot}$ . The main sequence companion receives a kick of  $86 \text{ km s}^{-1}$ , the subgiant  $49 \text{ km s}^{-1}$ . In all cases, the kick received by the remnant is smaller than the original orbital velocity. Because it is too small to intercept more than a negligible amount of momentum, the red giant core will not receive an appreciable kick.

The characteristic velocity of the stripped hydrogen (half-mass point in the distribution) is less than  $10^3 \text{ km s}^{-1}$  for all the scenarios. For the red giant case, the characteristic velocity is in the range  $420 - 590 \text{ km s}^{-1}$ , depending on the scenario. For the main sequence and subgiant cases, the characteristic velocities are  $820 \text{ km s}^{-1}$  and  $890 \text{ km s}^{-1}$ , respectively. With such low velocities, the bulk of the stripped hydrogen and helium is embedded within the low-velocity iron of the supernova ejecta. The region behind the stellar remnant that is contaminated with stripped hydrogen is always much larger than the geometrical shadow, the solid angle subtended by the companion as seen from the site of the explosion. For the main sequence companions the stripped hydrogen extends as far as  $66^{\circ}$  away from the downstream axis and for the subgiant case as far as  $72^{\circ}$ . The hydrogen from the red giant contaminates a much larger solid angle, as far as  $115^{\circ}$  from the downstream axis. These angles correspond to fractions of the sky of 29%, 35%, and 71%. This is one distinction between the main sequence, the subgiant, and the red giant scenarios. The stripped hydrogen and helium is distributed over a much wider solid angle for the red giant scenarios. Despite the change in distribution of the stripped material, the hole in the supernova debris (of angular size  $31^{\circ} - 34^{\circ}$ ) caused by the impact with the secondary is similar for all the scenarios.

If we define the efficiency of momentum transfer as the ratio of the momentum transferred to the stellar remnant to the incident momentum, then typical values for the main sequence simulations lie in the range of  $0.2 - 0.5$ , with the highest efficiency belonging to the secondary with the greatest binary separation. The characteristic velocity of the stripped material stays within  $660 - 860 \text{ km s}^{-1}$ , with the material from the closest binary companions having the highest velocities. The closest binaries will also create the widest plume of stripped material.

One motivation for this project is the possibility of using the velocity distribution of the stripped hydrogen and helium to discriminate between Type Ia progenitor models. However, to make any definitive predictions requires non-LTE radiative transfer calculations using the low-velocity distribution of the stripped material to determine the effect of hydrogen/helium contamination on the late-time supernova spectrum. Such calculations can determine the hydrogen



and helium line strengths and ratios of narrow emission lines that will emerge months after the impact, as the photosphere recedes to reveal the low-velocity supernova ejecta where the bulk of the stripped material is located. Unfortunately,  $H_\alpha$  is blended with numerous Fe and Co lines, especially [Co III] at 6578 Å, and will be difficult to identify. Because of atmospheric water absorption, a search for  $P_\alpha$  ( $1.87\mu m$ ) can not easily be conducted from the ground. Searches for  $P_\beta$  ( $1.28\mu m$ ) can be conducted from the ground, but telluric absorption and a  $P_\beta$  emission line from the Earth’s atmosphere require careful subtraction. Also,  $P_\beta$  is likely to be blended with a broad supernova Fe line at  $1.26\mu m$ . Other lines to look for are He lines at 5876 Å,  $1.083\mu m$ , and  $2.05\mu m$  that will be distributed in velocity and angle like the hydrogen, but note that high-velocity helium is also present in sub-Chandrasekhar explosion models. With a complete study of the emergence of the narrow hydrogen and helium lines and the competing Fe and Co lines in the late-time supernova spectrum, an optimum time may be found when the hydrogen may be detected and used to distinguish one Type Ia supernova scenario from another.

Although most of the stripped material is ejected at low velocities, all the numerical simulations yield a small high-velocity tail. Above  $3.0 \times 10^3 \text{ km s}^{-1}$ , all four scenarios have no more than  $\sim 0.014 M_\odot$  of high-velocity hydrogen. The HCVL simulation has  $0.014 M_\odot$ , followed by the HALGOLa with  $0.012 M_\odot$ , the HCV with  $0.010 M_\odot$ , and lastly, the SYMB simulation with only  $0.004 M_\odot$ . Above  $10^4 \text{ km s}^{-1}$ , the amount of high-velocity hydrogen has dropped by a factor of 10 for all four scenarios. In this velocity range ( $3.0 \times 10^3 - 10^4 \text{ km s}^{-1}$ ), we can easily discriminate between the companions in Roche lobe overflow and a model in which the red giant that is too distant to be in Roche lobe overflow, our SYMB scenario. Above  $1.5 \times 10^4 \text{ km s}^{-1}$ , the HALGOLa and the SYMB scenario have the most high-velocity hydrogen: the HALGOLa with  $3.3 \times 10^{-4} M_\odot$  and the SYMB with  $3.0 \times 10^{-4} M_\odot$ . We note that even if the red giant companions have more low-velocity hydrogen, they have substantially more hydrogen above  $1.5 \times 10^4 \text{ km s}^{-1}$  than the main sequence or subgiant models. Because the HCVL has more high-velocity hydrogen than the HCV scenario, we can discriminate between the subgiant and main sequence companions at  $1.5 \times 10^4 \text{ km s}^{-1}$ .

The Della Valle *et al.* (1996) observational upper limit from SN 1990M corresponds to a total hydrogen mass of  $\sim 3 \times 10^{-4} M_\odot$ . If this hydrogen is mixed only within the observable photosphere, then the main sequence, subgiant, and the red giant models are just under this upper limit. However, if the upper limit were reduced by only a factor of 3, the red giant and subgiant models would clearly exceed this limit, while the main sequence model is marginal. With this interpretation, the high-velocity tail of SN 1990M can not yet be used to exclude any progenitor models with hydrogen-rich companions.

The impact of the supernova ejecta on the secondary star creates an oddly shaped, small gap in the supernova debris. The highest velocity debris flows around the secondary, creating a narrow gap of angle  $\sim 31^\circ - 34^\circ$ . The lower velocity supernova material flows through the bow shock, creating a wider gap in the inner ejecta of angle  $\sim 40^\circ$ . Therefore, the hole in the supernova is narrow at the outside of the shell, broad at the inside of the shell, and filled with high-velocity

stripped material from the companion. As discussed above, most of the stripped material fills a wide solid angle and trails behind the supernova debris. Because the supernova flow is supersonic, the hole in the debris will not close with time. However, the orbital motion of the main sequence and subgiant secondaries will add a small component of velocity ( $100 - 200 \text{ km s}^{-1}$ ) tangential to the axis of the original binary system that will slowly distort the shape of the slow-moving contaminated region behind most of the supernova debris. The evolution and mixing of the hydrogen-filled region become a 3-D problem.

We use the angular size of the hole as an estimate of the region of asymmetry in the supernova ejecta caused by the impact on the companion star. The angular size of the gap in the supernova debris depends on the binary scenario. A typical angular size for the gap in the high-velocity material is  $31^\circ - 34^\circ$ , which corresponds to only  $7 - 8\%$  of the ejecta’s surface. The main sequence model has the smallest gap, the subgiant has a slightly larger gap, and the red giant has the largest gap. The typical angular size for the gap in the low-velocity ejecta is  $\sim 40^\circ$ , independent of the model. This corresponds to  $12\%$  of the surface area of the ejecta. Because the binary scenarios we explore are all close enough, or almost close enough, to be in Roche lobe overflow, the degree of asymmetry is similar for all the models. Asymmetry in the supernova ejecta will indicate the presence of a companion star, but it will be difficult to use the degree of asymmetry alone to discriminate between main sequence, subgiant, and red giant companions.

The asymmetry in the supernova debris could have observational consequences beyond the change in morphology of the supernova remnant. In the early-time spectra, subtle distortions may appear in the P Cygni lines that are dependent on the orientation of the hole in the supernova debris relative to the observer. For example, if the gap lies towards the observer, the P Cygni lines may have a distorted blue wing. If the gap lies at some angle away from the observer, the P Cygni lines may have a distorted red wing. However, because the hole in the supernova debris subtends such a small solid angle, its effect on the spectra will be equally small. The asymmetry may also affect the polarization of the supernova debris to some degree.

The impact of the supernova shell will also have consequences for the future evolution of secondary star. After the impact, the main sequence star is puffed up, much like a pre-main sequence star. Although the energy generation rate during the impact shoots up by a factor of  $\sim 1000$ , it immediately plummets as the star expands and cools. Hydrogen burning in the core will be nearly extinguished, but the luminosity will rise dramatically, to as high as  $\sim 5000 L_\odot$ , as the extended envelope relaxes back into thermal equilibrium and then follows a Kelvin-Helmholtz track on a timescale of  $\sim 10^4$  yrs. The supernova is initially much more luminous with  $L \sim 10^9 L_\odot$ . However, after  $2 - 3$  years, the supernova luminosity will have decayed enough that a very bright secondary might be visible. After thermal equilibrium is reestablished and the residue has settled back onto the main sequence, the remnant will continue its evolution at a rate prescribed by its new mass. The  $1.0 M_\odot$  main sequence secondary will eventually return to the main sequence with a mass of  $0.85 M_\odot$ , having lost  $0.15 M_\odot$  due to the impact, with a slightly smaller radius of  $0.9 R_\odot$ , and a luminosity of  $\sim 0.4 L_\odot$ . The subgiant puffs up after the impact and must contract to

reignite hydrogen shell-burning, which has been extinguished during the subgiant’s expansion. Like the main sequence case, the luminosity will be high during this phase.

A He pre-white dwarf will be left after a supernova explosion with a red giant companion. Almost all the envelope will be ejected by the impact, but a residual amount of material will form an extended, hydrogen-rich envelope around the degenerate core. This extended envelope of  $\sim 0.02 M_{\odot}$  of hydrogen-rich material will settle down onto the star to feed the hydrogen burning shell. The star will evolve away from the red giant branch at constant luminosity and increasing effective temperature on a timescale of  $10^5 - 10^6$  years. Before the luminosity drops, it may appear as an underluminous O or B star. When the star begins to dim and cool, it may pass through an sdO or sdB phase before retiring along a standard He white dwarf cooling track. This binary scenario could be a possible pathway for the formation of a subset of single, low-mass He white dwarfs.

The metallicity of the secondary may increase if it accretes any supernova material as a result of the explosion. We do not expect that the secondary star will accrete a significant amount of supernova material by the direct impact of the supernova shell on the surface of the star because, as the shock created by the impact propagates through the stellar envelope, the shock-heated material escapes the secondary, carrying away any impinging supernova material. However, this does not necessarily mean that the secondary will not accrete any low-velocity iron-group elements (or oxygen and silicon if the ejecta is radially mixed) long after the initial impact.

High resolution late-time observations focused on detecting stripped hydrogen and helium from the companion star are needed to verify the single-degenerate scenario. With non-LTE synthetic spectra, such observations may be used to discriminate between the main sequence, the subgiant, and the red giant companions. Asymmetry in the supernova ejecta, distorted P Cygni lines or line ratios, and slight polarization may also indicate an unseen companion star. Our theoretical study was performed in support of the quest to unravel the persistent mystery of the site of Type Ia supernova explosions. Given the emerging cosmological importance of such explosions as standardizable candles and the resulting renaissance in their study, the time is ripe for a renewed investigation into the consequences of the variety of binary scenarios for thermonuclear supernovae.

We thank Brian Chaboyer for the stellar models used in the simulations and Matthias Steinmetz for the Poisson solver. Conversations with Phil Pinto, Jim Liebert, Peter Hoefflich, and Betsy Green are gratefully acknowledged. This work was supported by NSF grant AST96-17494, NASA GSRP Fellowship NGT-51305, and by the ASCI Center for Thermonuclear Flashes at the University of Chicago, under DOE contract B341495. The calculations were performed on the Cray C90 at Pittsburgh Supercomputer Center and on the Cray T90 at the San Diego Supercomputer Center. Postscript images, MPEG movies, and a selection of figures presented in this paper, are posted at <http://www.astrophysics.arizona.edu> and are available via FTP at [www.astrophysics.arizona.edu](http://www.astrophysics.arizona.edu), in directory pub/marietta. This research has made use of NASA’s Astrophysics Data System Abstract Service.

## REFERENCES

- Applegate, J. H., & Terman, J. L. 1989, *ApJ*, **340**, 380
- Benvenuto, O. G., & Althaus, L. G. 1999, *MNRAS*, **303**, 30
- Branch, D., Buta, R., Falk, S. W., McCall, M. L., Sutherland, P. G., Uomoto, A., Wheeler, J. C., & Wills, B. J. 1982, *ApJ*, **252**, L61
- Branch, D., Lacy, C. H., McCall, M. L., Sutherland, P. G., Uomoto, A., Wheeler, J. C., & Wills B. J. 1983, *ApJ*, **270**, 123
- Branch, D., Doggett, J. B., Nomoto, K., & Thielemann, F. 1985, *ApJ*, **294**, 619
- Branch, D., Pauldrach, W. A., Puls, J., Jeffery, D. J., & Kudritzki, R. P. 1991, in *SN1987A and Other Supernovae*, eds. J. Danziger et al., (Garching: ESO)
- Branch, D., Livio, M., Yungelson, L. R., Boffi, F. R., & Baron, E. 1995, *PASP*, **107**, 1019
- Chaboyer, B. 1998, private communication
- Cheng, A. 1974, *Ap&SS*, **31**, 49
- Chugai, N. N. 1986, *Soviet Astronomy*, **30**, 563
- Clayton, D. C. 1983, *Principles of Stellar Evolution and Nucleosynthesis*, (University of Chicago Press, Chicago)
- Colella, P., & Woodward, P. 1984, *J. Comp. Phys.*, **54**, 174
- Colella, P., & Glaz, H., M. 1985, *J. Comp. Phys.*, **59**, 264
- Colgate, S. A. 1970, *Nature*, **225**, 247
- Cox, J. P., & Giuli, R. T. 1968, *Principles of Stellar Structure, Volume 1 and 2*, (Gordon and Breach, New York)
- Cumming, R. J., Lundqvist, P., Smith, L. J., Pettini, M., & King, D. L. 1996, *MNRAS*, **283**, 1355
- Della Valle, M., & Livio, M. 1994, *ApJ*, **423**, L31
- Della Valle, M., Benetti, S., & Panagia, N. 1996, *ApJ*, **459**, L23
- Eggleton, P. P. 1983, *ApJ*, **268**, 368
- Filippenko, A. V. 1997, *ARA&A*, **35**, 309
- Fryxell, B. A., & Arnett, W. D. 1981, *ApJ*, **243**, 994
- Fryxell, B. A., Müller, E. & Arnett, W. D. 1989, Max-Planck-Institut für Astrophysik Report, **449**

- Garnavich, P. M., & Challis, P. M. 1997, in the proceedings of the NATO-ASI on Thermonuclear Supernovae, held in Aiguablava, Spain, June 19-30, 1995, *Thermonuclear Supernovae*, 711 (Kluwer Academic Publishers)
- Green, E. 1999, personal communication
- Hachisu, I., Kato, M., & Nomoto, K. 1996, *ApJ*, **470**, L97
- Hachisu, I., Kato, M., & Nomoto, K. 1999a, preprint
- Hachisu, I., Kato, M., Nomoto, K., & Umeda, H. 1999b, preprint
- Ho, L. C., & Filippenko, A. V. 1995, *ApJ*, **444**, 165
- Iben, I., Jr., & Tutukov, A. 1984, *ApJS*, **54**, 335
- Iben, I., Jr., & Tutukov, A. 1986, *ApJ*, **311**, 742
- Iben, I., Jr., & Tutukov, A. 1991, *ApJ*, **370**, 615
- Iben, I., Jr., & Livio, M. 1993, *PASP*, **105**, 1373
- Iben, I., Jr., & Tutukov, A. 1993, *ApJ*, **418**, 343
- Iben, I., Jr., & Tutukov, A. 1994, *ApJ*, **431**, 264
- Israelian, G., Rebolo, R., Basri, G., Casares, J., & Martín, E. L. 1999, submitted to *Nature*, January 1999
- Jeffery, D. J., Leibundgut, B., Kirshner, R. P., Benetti, S., Branch, D., & Sonneborn, G. 1992, *ApJ*, **397**, 304
- Kenyon, S. J., Livio, M., Mikolajewska, J., & Tout, C. A. 1993, *ApJ*, **407**, L81
- Kippenhahn, R. & Weigert, A. 1991, *Stellar Structure and Evolution*, (Springer-Verlag, New York)
- Li, X.-D., & van den Heuvel, E. P. J. 1997, *A&A*, **322**, L9
- Livio, M. & Truran, J. W. 1992, *ApJ*, **389**, 695
- Livio, M. 1999, preprint
- Leibundgut, B., Kirshner, R. P., Filippenko, A. V., Shields, J. C., Foltz, C. B., Phillips, M. M., & Sonneborn G. 1991, *ApJ*, **371**, L23
- Livne, E., Tuchman, Y., & Wheeler, C. J. 1992, *ApJ*, **399**, 665
- Marsh, T. R., Dhillon, V. S., & Duck, S. R. 1995, *MNRAS*, bf 275, 828
- Müller, E., & Steinmetz, M. 1995, *Computer Physics Communications*, **89**, 45

- Nomoto, K. 1982a, ApJ, **253**, 798
- Nomoto, K. 1982b, ApJ, **257**, 780
- Nomoto, K., Thielemann, F.-K., & Yokoi, K. 1984, ApJ, **286**, 644
- Nomoto, K., & Kondo Y. 1990, ApJ, **367**, L19
- Nomoto, K., Iwamoto, K., Tsujimoto, T., & Suzuki, T. 1995, Phys. Rep., **256**, 173
- Nomoto, K., Hashimoto, M., Tsujimoto, T., Thielemann, F.-K., Kishimoto, N., Kubo, Y., & Nakasato, N. 1997, Nucl. Phys. A, **616**, 79
- Pinto, P. *et al.* 1999, in prep.
- Polcaro, V. F., & Viotti, R. 1991, A&A, **242**, L9
- Rappaport, S., DiStefano, R., & Smith, J. D. 1994, ApJ, **426**, 692
- Ruiz-Lapuente, P., Jeffrey, D. J., Challis, P. M., Filippenko, A. V., Kirshner, R. P., Ho, L. C., Schmidt, B. P., Sánchez, F., & Canal, R. 1993, Nature, **365**, 728
- Ruiz-Lapuente, P. 1996, in the proceedings of the NATO-ASI on Thermonuclear Supernovae, held in Aiguablava, Spain, June 19-30, 1995, *Thermonuclear Supernovae*, 205 (Kluwer Academic Publishers)
- Ruiz-Lapuente, P. 1997, *Science*, **276**, 1813
- Saffer, R. A., Livio, M., & Yungelson, L. R. 1998, ApJ, **502**, 394
- Sills, A., Lombardi, J. C. Jr., Baily C. D., Demarque P., Rasio F. A., & Shapiro S. L. 1997, ApJ, **487**, 290
- Sofia, S. 1967 ApJ, **149**, L59
- Taam, R. E., & Fryxell, B. A. 1984, ApJ, **279**, 166
- Tutukov, A. V., Yungelson, L. R., & Iben, I., Jr. 1992, ApJ, **386**, 197
- Turatto, M., Benetti, S., Cappellaro, E., Danziger, I. J., Della Valle, M., Gouiffes, C., Mazzali, P. A., & Patat, F. 1996, MNRAS, **283**, 1
- Verbunt, F. & Zwaan, C. 1981, A&A, **100**, L7
- Webbink, R. F. 1984, ApJ, **277**, 355
- Wheeler, C. J., Lecar, M., & McKee, C. F. 1975, ApJ, **200**, 145
- Wheeler, J. C., & Harkness, R. P. 1990, Rep. Prog. Phys., **53**, 1467

- Wheeler, C. J. 1992, IAU Symposium 151 *Evolutionary Processes in Interacting Binary Stars*, eds. Y. Kondo et al., (Kluwer Academic Publishers)
- Whelan, J. & Iben, I. 1973, ApJ, **186**, 1007
- Woosley, S. E., & Weaver, T. A. 1986, ARA&A, **24**, 205
- Woosley, S. E., & Weaver, T. A. 1994, ApJ, **423**, 371
- Yungelson, L., Livio, M., Tutukov, A., & Kenyon, S. J. 1995, ApJ, **447**, 656
- Yungelson, L., Livio, M. 1998, ApJ, **497**, 168

Fig. 1.— Mass vs. radius for the main sequence, subgiant, and red giant secondaries.

Fig. 2.— Absolute value of the exterior binding energy of the main sequence, subgiant, and red giant secondaries. The binding energy of each secondary is provided next to its legend. The value listed for the red giant secondaries is the binding energy of the envelope only. The dashed line indicates the binding energy profile of the red giant core.

Fig. 3.— Frames (a)-(d) illustrate the impact of supernova Type Ia W7 on a  $1.0 M_{\odot}$  main sequence companion at 29, 104, 179 and 329 seconds after the explosion. The color scale indicates  $\text{Log}_{10}\rho$ : blue  $\sim 160.0 \text{ gm cm}^{-3} \rightarrow$  red  $\sim 10^{-13} \text{ gm cm}^{-3}$ . The explosion occurs off the grid at a distance consistent with the companion losing mass to the white dwarf primary by Roche lobe overflow. Frame (a) shows the companion star at the origin of the grid at 29 seconds, just prior to the impact of the debris. In Frame (b), at 104 seconds, the leading edge of the supernova shell has just collided with the surface of the companion. By 179 seconds (Frame (c)), the leading edge of the supernova shell converges along the downstream axis. The companion is now enveloped in the supernova ejecta. Frame (d), at 329 seconds, shows the shock wave that was driven into the companion by the impact and the bow shock just upstream of the companion. MPEG movies and 2-D images are posted at <http://www.astrophysics.arizona.edu> and are available via FTP from [www.astrophysics.arizona.edu](http://www.astrophysics.arizona.edu), in directory `pub/marietta`.

Fig. 4.— Frames (a)-(d) illustrate the impact of supernova Type Ia W7 on a  $1.0 M_{\odot}$  main sequence companion at 529, 755, 2029 and 2033 seconds after the explosion. The color scale is the same as in Figure 3. In Frame (a) the shock has just passed through the stellar core. In Frame (b) the shock has converged within the star along the downstream axis. Kelvin-Helmholtz and Rayleigh-Taylor instabilities are visible in both frames. Frame (c) illustrates the end of the mass stripping phase. By Frame (d), several dynamical times have passed, and the remnant is beginning to recover hydrostatic equilibrium.

Fig. 5.— Frames (a)-(f) illustrate the impact of supernova Type Ia W7 on a  $1.0 M_{\odot}$  main sequence companion in a series of cartoon images, each color indicating the dominant element in that region. For clarity each region is also numbered: (1) circumstellar medium, (2) stellar hydrogen, (3) supernova oxygen-group elements, (4) supernova silicon, and (5) supernova iron-group elements. The frames shown are at 104, 179, 329, 529, 755, and 2029 seconds after the explosion. Frames (a) and (b) show the initial impact. The oxygen, silicon, and iron layers of the supernova ejecta are clearly visible. Frames (c) and (d) illustrate the beginning of the mass stripping phase when the outermost layer of the companion’s envelope is stripped and caught in the oxygen and silicon layers of the supernova ejecta. By Frame (e), any mass lost from the companion’s envelope is embedded within the iron region of the supernova ejecta. Frame (f) shows the end of the mass stripping phase. The envelope of the companion is now extended; about 15% of the mass will escape the companion and follow the flow of the supernova.

Fig. 6.— Momentum and density profile of SNIa W7 and SNIa Hedt. SNIa W7 is shown at 24 hrs



while SNIa Hedt is shown at 27.87 hrs.

Fig. 7.— Pressure profile of the initial impact on the main sequence secondary (HCV) along the  $z$  axis, illustrating the propagation of the shock through the stellar core and the development of the bow shock. The profiles shown are at 29, 104, 179, 257, 332, 451, 601, 676, and 2030 seconds after the explosion and are labeled 1-9, respectively. The first and last timesteps are marked by thicker lines. They represent the undisturbed companion and the companion after the mass stripping is complete and are included for reference.

Fig. 8.— Pressure profile of the main sequence secondary (HCV) along the  $z$  axis, illustrating the abrupt pressure rise in the back of the star as the stellar shock converges along the axis. As the shock-heated material is ejected from the star, the back pressure drops. The profiles shown are at 29, 751, 827, 902, 1026, 1178, 1528, and 2030 seconds after the explosion and are labeled 1-8, respectively. The first and last timestep are marked by thicker lines. They represent the undisturbed companion and the companion after the mass stripping is complete.

Fig. 9.— Pressure profile of the main sequence secondary (HCV) along the  $z$  axis as the star recovers hydrostatic equilibrium. The remnant is now moving down the axis with the kick received by the impact. The profiles shown are at 29, 2030, 5035, 10053, 15056, and 20032 seconds after the explosion and are labeled 1-6, respectively. The first and last timesteps are marked by thicker lines; they represent the undisturbed companion and the post-impact companion after several pulsations.

Fig. 10.— Central density and temperature as a function of time for the HCV scenario ( $1.0 M_{\odot}$  secondary)

Fig. 11.— Pre- and Post-impact density profile of the the main sequence secondary (HCV) and the subgiant secondary (HCVL).

Fig. 12.— Pre- and Post-impact entropy profile (per Boltzmann’s constant per baryon) of the main sequence secondary (HCV) and the subgiant secondary (HCVL).

Fig. 13.— Estimate of nuclear energy generation from the pp chains and the CNO cycle for the HCV scenario ( $1.0 M_{\odot}$  secondary) using a 1-D section with spherical symmetry. The compression and expansion of the stellar core releases  $\sim 10^{38}$  ergs in the first 1000 seconds.

Fig. 14.— A. Velocity distribution  $dM/dV$  of the stripped stellar hydrogen and helium for the HCV binary scenario at the end of the simulation, along with the velocity distribution of SNIa W7. The velocity at the half-mass point of the HCV distribution, as indicated by the vertical line and the arrow, is  $823 \text{ km s}^{-1}$ . In contrast, the velocity at the half-mass point of the SN W7 distribution, also indicated in the plot, is  $7836 \text{ km s}^{-1}$ . B. Velocity distribution  $dM/dV$  of the stripped stellar hydrogen and helium for the HCVL binary scenario at the end of the simulation, along with the velocity distribution of SNIa W7. The velocity at the half-mass point of the HCVL distribution,

as indicated by the vertical line and the arrow, is  $887 \text{ km s}^{-1}$ .

Fig. 15.— The solid angle distribution of the stripped envelope of the main sequence and subgiant simulations HCV and HCVL. The half-mass angle of each distribution is listed. The dashed lines indicate the distribution of supernova material for both simulations. The hole in the supernova debris created by the impact is visible between  $0^\circ - 40^\circ$ .

Fig. 16.— The magnitude of the angular distribution ( $dM/d\alpha$ ) is plotted as the radial coordinate for the HCV and HCVL binary scenarios. The angular coordinate is the angle from the downstream axis. The geometrical shadow is shown for both simulations.

Fig. 17.— Hydrogen mass fraction of the contaminated supernova ejecta for the HCV scenario ( $1.0 M_\odot$  main sequence secondary) vs. the mass of the original W7 supernova model. The solid line indicates the hydrogen mass fraction assuming that the stripped material is uniformly mixed in angle with Type Ia model W7. The mass fractions of the O, Si, and Fe-group elements are shown for comparison. Because the stripped material in this simulation contaminates only the supernova ejecta within  $65.7^\circ$  of the downstream axis, the dashed line indicates the hydrogen mass fraction assuming mixing only in this region.

Fig. 18.— Hydrogen mass fraction of the contaminated supernova ejecta for the HCV scenario ( $1.0 M_\odot$  main sequence secondary) vs. velocity. See the caption for Figure 17.

Fig. 19.— Frames (a)-(d) illustrate the impact of supernova Type Ia W7 on a  $1.0 M_\odot$  main sequence companion for different binary separations: simulations HCV, HCVb, HCVc, and HCVd. The color scale indicates  $\text{Log}_{10}\rho$ : blue  $\sim 160.0 \text{ gm cm}^{-3} \rightarrow$  red  $\sim 10^{-13} \text{ gm cm}^{-3}$ . This color scale is the same as in Figure 3. Frame (a) shows the impact for a ratio  $a/R = 3.0$  (binary separation over stellar radius) at 1031 seconds after the explosion. This is our HCV simulation. Frame (b) shows the impact with  $a/R = 4.0$  at 1336 seconds after explosion, the HCVb test case. Frame (c) shows the impact with  $a/R = 6.0$  at 1197 seconds, and Frame (d) with  $a/R = 12.0$  at 1308 seconds. The timesteps are increasing primarily because the length of time needed for the supernova ejecta to reach the secondary is increasing.

Fig. 20.— The magnitude of the angular distribution ( $dM/d\alpha$ ) is plotted as the radial coordinate for the main sequence simulation HCV and test cases HCVa, HCVb, and HCVc, which differ only in their distance from the supernova explosion. The half-mass angles of the distributions are  $45.1^\circ$ ,  $42.7^\circ$ ,  $35.8^\circ$ ,  $24.7^\circ$ , and  $9.9^\circ$  for the HCVa, HCV, HCVb, HCVc, and HCVd simulations, respectively.

Fig. 21.— Frames (a)-(d) illustrate the impact of supernova Type Ia W7 on a  $1.13 M_\odot$  subgiant companion at 343, 945, 2044 and 20044 seconds after the explosion. The color scale indicates  $\text{Log}_{10}\rho$ : blue  $\sim 2.7 \times 10^3 \text{ gm cm}^{-3} \rightarrow$  red  $\sim 10^{-13} \text{ gm cm}^{-3}$ . The explosion occurs off the grid at a distance consistent with the companion losing mass to the white dwarf primary by Roche lobe overflow. Frame (a) shows the subgiant and the incoming supernova shell 343 seconds after the

explosion. Only  $0.06 M_{\odot}$  of the companion’s envelope has been stripped by this time. In Frame (b) at 945 seconds, the shock has just propagated through the subgiant’s core and is about to converge in the back of the subgiant. Frame (c) shows the subgiant in the last stages of mass loss. The subgiant has lost  $0.15 M_{\odot}$  of its envelope which can be seen streaming away from the subgiant. By Frame (d), 20044 seconds after the explosion, the remnant of the subgiant is recovering hydrostatic equilibrium.

Fig. 22.— Impact of supernova Type Ia W7 on a  $1.13 M_{\odot}$  subgiant companion at 1958 seconds near the end of the mass stripping phase. The Kelvin-Helmholtz instabilities, which help the hot material to escape the surface, are easily seen in this image. The color scale is the same as in Figure 21.

Fig. 23.— Hydrogen mass fraction of the contaminated supernova ejecta for the HCVL scenario ( $1.1 M_{\odot}$  subgiant secondary) vs. the mass of the original W7 supernova model. The solid line indicates the hydrogen mass fraction assuming that the stripped material is uniformly mixed in angle with W7. The mass fractions of the O, Si, and Fe-group elements are shown for comparison. Because the stripped material in this simulation contaminates the supernova ejecta within only  $72.5^{\circ}$  of the downstream axis, the dashed line indicates the hydrogen mass fraction assuming mixing only in this region.

Fig. 24.— Hydrogen mass fraction of the contaminated supernova ejecta for the HCVL scenario ( $1.1 M_{\odot}$  subgiant secondary) vs. velocity. See the caption for Figure 23.

Fig. 25.— Frames (a)-(d) illustrate the impact of supernova Type Ia Hedt on a  $0.98 M_{\odot}$  red giant companion at 8.7 hrs, 14.3 hrs, 2.1 days and 5.9 days after the explosion. Only the region around the red giant is shown to emphasize the interaction. The full images are shown in Figures 26.

Fig. 26.— Frames (a)-(d) illustrate the impact of supernova Type Ia Hedt on a  $0.98 M_{\odot}$  red giant companion at 8.7 hrs, 14.3 hrs, 2.1 days and 5.9 days after the explosion. In these images the supernova can be seen exploding on the grid. These are the full images corresponding to the images in Figures 25.

Fig. 27.— A. Velocity distribution  $dM/dV$  of the stripped stellar hydrogen and helium for the HALGOLa binary scenario at the end of the simulation, along with the velocity distribution of SNIa W7. The velocity at the half-mass point of the HALGOLa distribution, as indicated by the vertical line and the arrow, is  $593 \text{ km s}^{-1}$ . In contrast, the velocity at the half-mass point of the SN W7 distribution, also indicated in the plot, is  $7836 \text{ km s}^{-1}$ . B. Velocity distribution  $dM/dV$  of the stripped stellar hydrogen and helium for the SYMB binary scenario. The velocity at the half-mass point of the SYMB distribution, as indicated by the vertical line and the arrow, is  $421 \text{ km s}^{-1}$ . The velocity at the half-mass point of the SN Hedt distribution, also indicated in the plot, is  $10000 \text{ km s}^{-1}$ .

Fig. 28.— Solid angle distribution of the stripped envelope of the red giant simulations HALGOLa

and SYMB. The dashed lines indicate the distribution of supernova material. The gap between  $0^\circ - 40^\circ$  illustrates the hole in the supernova ejecta created by the impact.

Fig. 29.— The magnitude of the angular distribution ( $dM/d\alpha$ ) is plotted as the radial coordinate for the red giant simulations (HALGOLa and SYMB).

Fig. 30.— Hydrogen mass fraction of the contaminated supernova ejecta for the HALGOLa scenario ( $0.98 M_\odot$  red giant secondary) vs. the mass of the original W7 supernova model. The solid line indicates the hydrogen mass fraction assuming that the stripped material is uniformly mixed in angle with Type Ia model W7. The mass fractions of the O, Si, and Fe-group elements are shown for comparison. Because the stripped material in this simulation contaminates the supernova ejecta within only  $115.4^\circ$  of the downstream axis, the dashed line indicates the hydrogen mass fraction assuming mixing only in this region.

Fig. 31.— Hydrogen mass fraction of the contaminated supernova ejecta for the HALGOLa scenario ( $0.98 M_\odot$  subgiant secondary) vs. velocity. See the caption for Figure 30.

Fig. 32.— Mass of stripped hydrogen with velocity  $\geq V$  for the HCV ( $1.0$  main sequence), HCVL ( $1.13 M_\odot$  subgiant), SYMB and HALGOLa ( $1.0 M_\odot$  red giant) simulations. To compare the mass profiles to Type Ia supernova observations near maximum light, we indicate with a horizontal line the Della Valle *et al.* (1996) upper limit of  $3 \times 10^{-4} M_\odot$  of hydrogen in the spectrum of SN 1990M. This assumes perfect radial mixing of the silicon and hydrogen. Because Della Valle *et al.* (1996) estimated the error in the upper limit to be a factor of  $2 - 3$ , we also include horizontal lines to indicate this range. Della Valle *et al.* (1996) estimated that the size of the photosphere was  $0.04 M_\odot$  at the time of the observation. The velocity corresponding to this mass is estimated from SNIa W7 and shown in the figure as a vertical line.

Table 1. Single Degenerate Type Ia Models

Single Degenerate SNIa	Secondary	Mass Transfer
Hydrogen Cataclysmic Variables	Main Sequence/Subgiant	RLOF, H
Hydrogen Cataclysmic-Like Variables	Main Sequence/Subgiant	RLOF, H
Symbiotic Stars	Red Giant	Wind, H
Hydrogen Algols	Red Giant	RLOF, H
Helium Cataclysmic Variables	He Star	RLOF, He
Helium Algols	He Giant	RLOF, He

Table 2. Secondary Models

Evolutionary Stage	M ( $M_{\odot}$ )	R (km)	$t_{dyn}$ (s) <sup>a</sup>	$t_{cross}$ (s) <sup>b</sup>
Main Sequence	1.017	$6.80 \times 10^5$	$1.5 \times 10^3$	$2.6 \times 10^3$
Subgiant	2.118	$1.62 \times 10^6$	$4.0 \times 10^3$	$5.8 \times 10^3$
Subgiant, mass loss	1.132	$1.22 \times 10^6$	$3.5 \times 10^3$	$5.5 \times 10^3$
Red Giant <sup>c</sup>	0.977	$1.19 \times 10^8$	$6.4 \times 10^6$	$5.5 \times 10^6$

<sup>a</sup>Dynamical time,  $t_{dyn} = \frac{1}{2} (G\langle\rho\rangle)^{-1/2}$

<sup>b</sup>Sound crossing time,  $t_{cross} = R/\langle c_s \rangle$ , integrated over star

<sup>c</sup>Softened  $\phi(r) = -GM_c/(r + r_c)$ ,  $M_c = 0.424 M_{\odot}$ ,  $R_c = 5 \times 10^5$  km

Table 3. Supernova Ejecta Models

Model	M ( $M_{\odot}$ )	E ( $10^{51}$ ergs)	P ( $M_{\odot} V_c$ ) <sup>a</sup>	$\langle V \rangle$ <sup>b</sup>	$V_{\frac{1}{2}M}$ <sup>c</sup>
SNIa W7 <sup>d</sup>	1.378	1.233	1.175	$8.527 \times 10^3$	$7.836 \times 10^3$
SNIa Hedtb11 <sup>e</sup>	0.899	1.079	0.912	$1.014 \times 10^4$	$1.006 \times 10^4$

<sup>a</sup>Momentum of supernova ejecta, specified in units of  $M_{\odot}$  and divided by  $V_c = 10^9$  cm s<sup>-1</sup>

<sup>b</sup>Average speed of the supernova ejecta, km s<sup>-1</sup>

<sup>c</sup>Speed of the supernova ejecta at the half-mass point, km s<sup>-1</sup>

<sup>d</sup>Nomoto *et al.* 1984

<sup>e</sup>Woosley & Weaver 1994

Table 4. Simulations

Simulations	M ( $M_{\odot}$ )	a (km)	a/R	SN Model
HCV	1.017 (MS)	$2.04 \times 10^6$	3.00	W7
	Additional Separations			
HCVa	1.017 (MS)	$1.75 \times 10^6$	2.57	W7
HCVb	1.017 (MS)	$2.72 \times 10^6$	4.00	W7
HCVc	1.017 (MS)	$4.08 \times 10^6$	6.00	W7
HCVd	1.017 (MS)	$8.16 \times 10^6$	12.00	W7
HCVL	1.132 (SG)	$3.39 \times 10^6$	2.78	W7
	No Mass Loss			
HCVLa	2.118 (SG)	$4.50 \times 10^6$	2.78	W7
HALGOLa	0.977 (Red Giant)	$3.00 \times 10^8$	2.52	W7
SYMB	0.977 (Red Giant)	$3.76 \times 10^8$	3.16	Hedt

Table 5. Pre- and Post-Impact Central Values for HCV Companion

	Initial	Final	Fractional Change
Pressure (dynes $\text{cm}^{-2}$ )	$2.34 \times 10^{17}$	$9.41 \times 10^{16}$	0.60
Density ( $\text{gm cm}^{-3}$ )	$1.54 \times 10^2$	$7.95 \times 10^1$	0.48
Temperature (K)	$1.56 \times 10^7$	$9.68 \times 10^6$	0.38
Entropy ( $k_b^{-1}$ baryon $^{-1}$ )	$1.10 \times 10^1$	$1.35 \times 10^1$	0.23

Table 6. Stripped Mass

Scenario	Time (s)	$\Delta M (M_{\odot})^a$	$\Delta M (M_{\odot})^b$
HCV	$2.0 \times 10^4$	0.15	0.16
HCVa	$2.0 \times 10^4$	0.23	0.20
HCVb	$2.5 \times 10^4$	0.074	0.11
HCVc	$3.0 \times 10^4$	0.022	0.063
HCVd	$3.0 \times 10^4$	0.0018	0.021
HCVL	$3.0 \times 10^4$	0.17	0.14
HCVLa	$3.0 \times 10^4$	0.25	0.21
HALGOLa	$6.0 \times 10^6$	0.54 (98%)	0.55 (100%)
SYMB	$8.0 \times 10^6$	0.53 (96%)	0.55 (100%)

<sup>a</sup>Numerical Calculation of Stripped Mass

<sup>b</sup>Analytic Estimate of Stripped Mass, method of Wheeler *et al.* 1975

Table 7. Kicks

Scenario	$M_{rem} (M_{\odot})^a$	$V_{rem}^b$	$V^c$	$V_{orb}^d$	$P_{rem}/P_{in}^e$
HCV	0.867	85.7	109.8	227.1	0.228
HCVa	0.787	99.2	137.1	245.2	0.176
HCVb	0.943	61.5	73.2	196.7	0.316
HCVc	0.995	35.2	41.7	160.6	0.429
HCVd	1.015	10.1	14.8	113.5	0.503
HCVL	0.962	49.4	70.4	172.1	0.125
HCVLa	1.868	54.4	65.4	126.5	0.267

<sup>a</sup>Numerical Calculation of the Mass of the Stellar Remnant

<sup>b</sup>Numerical Calculation of the Kick of the Stellar Remnant,  $\text{km s}^{-1}$

<sup>c</sup>Ballpark Estimate of Kick from Inelastic Collision,  $\text{km s}^{-1}$

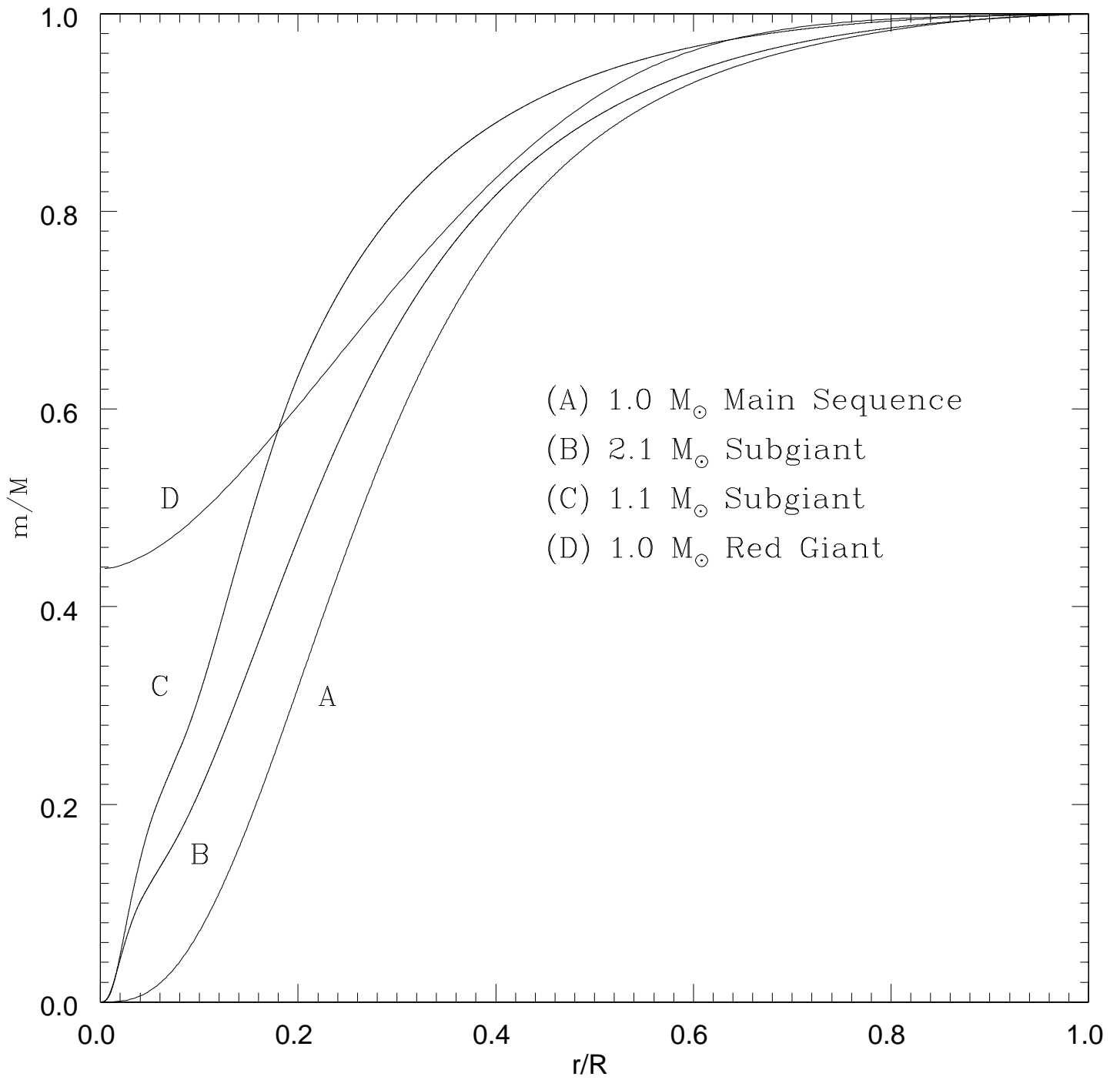
<sup>d</sup>Orbital Velocity,  $\text{km s}^{-1}$

<sup>e</sup>Ratio of Stellar Remnant Momentum ( $P_{rem}$ ) to Incident Supernova Momentum ( $P_{in}$ )

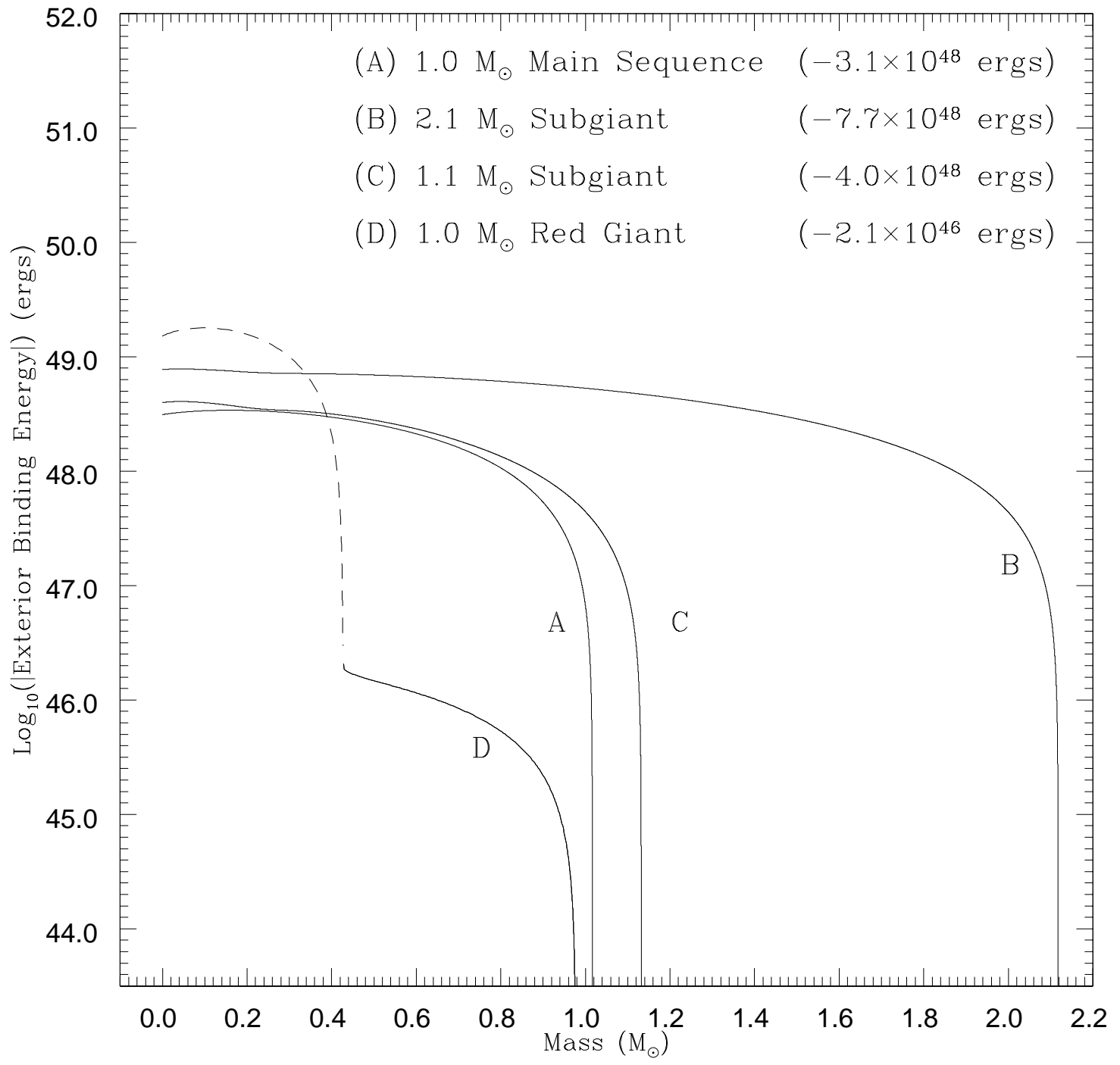


Table 8. Mass of Stripped Hydrogen with Velocity  $\geq V$  at four chosen points:  
 $V_A = 3.0 \times 10^3 \text{ km s}^{-1}$ ,  $V_B = 1.0 \times 10^4 \text{ km s}^{-1}$ ,  $V_C = 1.2 \times 10^4 \text{ km s}^{-1}$ , and  
 $V_D = 1.5 \times 10^4 \text{ km s}^{-1}$ .

Scenario	A	B	C	D
HCV	$9.7 \times 10^{-3} M_\odot$	$1.3 \times 10^{-3} M_\odot$	$6.9 \times 10^{-4} M_\odot$	$1.3 \times 10^{-4} M_\odot$
HCVL	$1.4 \times 10^{-2} M_\odot$	$1.4 \times 10^{-3} M_\odot$	$7.8 \times 10^{-4} M_\odot$	$1.7 \times 10^{-4} M_\odot$
HALGOLa	$1.2 \times 10^{-2} M_\odot$	$1.4 \times 10^{-3} M_\odot$	$8.9 \times 10^{-4} M_\odot$	$3.3 \times 10^{-4} M_\odot$
SYMB	$4.3 \times 10^{-3} M_\odot$	$6.2 \times 10^{-4} M_\odot$	$4.8 \times 10^{-4} M_\odot$	$3.0 \times 10^{-4} M_\odot$



- (A) 1.0  $M_{\odot}$  Main Sequence ( $-3.1 \times 10^{48}$  ergs)
- (B) 2.1  $M_{\odot}$  Subgiant ( $-7.7 \times 10^{48}$  ergs)
- (C) 1.1  $M_{\odot}$  Subgiant ( $-4.0 \times 10^{48}$  ergs)
- (D) 1.0  $M_{\odot}$  Red Giant ( $-2.1 \times 10^{46}$  ergs)



This figure "F3.gif" is available in "gif" format from:

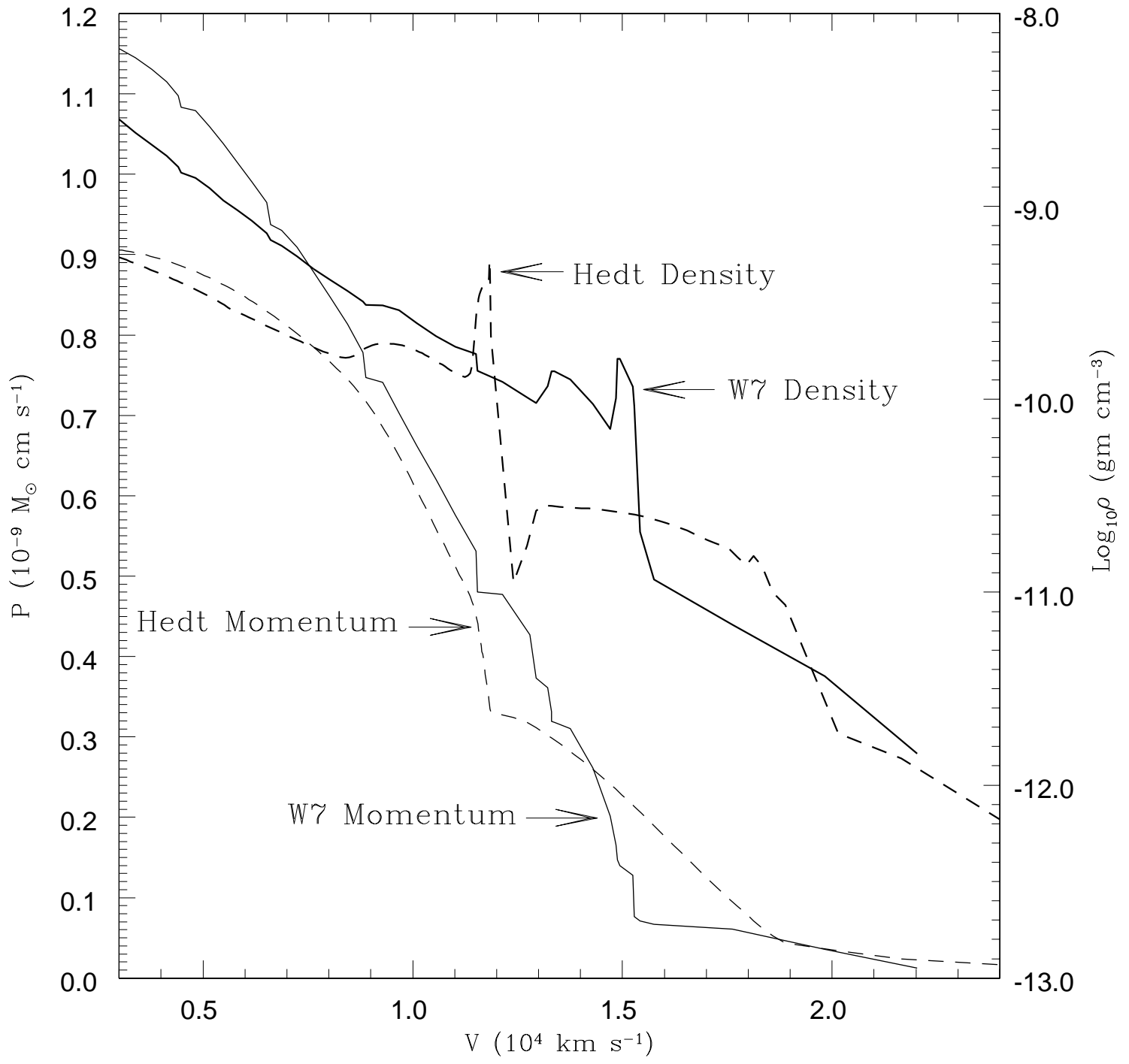
<http://arxiv.org/ps/astro-ph/9908116v1>

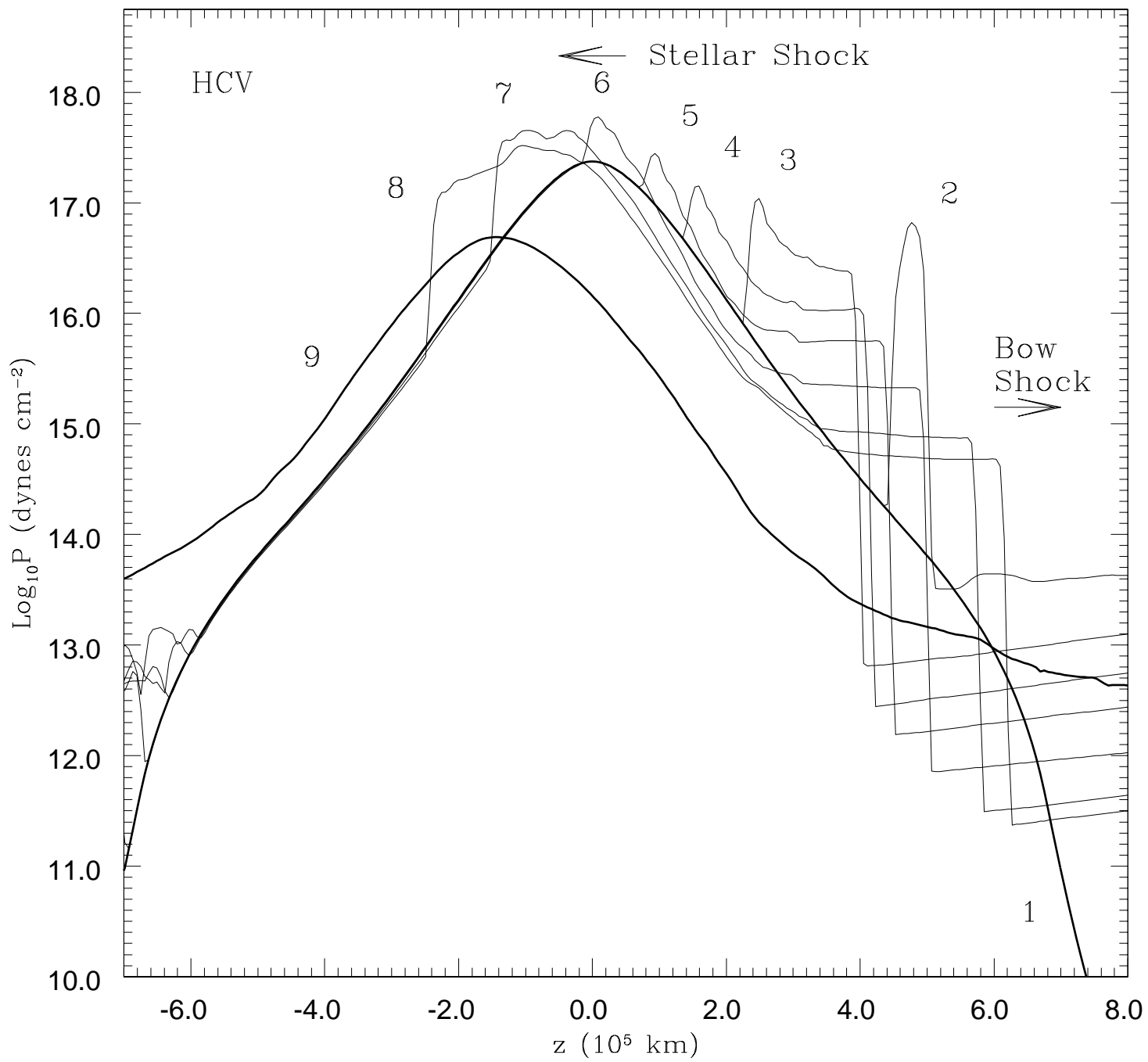
This figure "F4.gif" is available in "gif" format from:

<http://arxiv.org/ps/astro-ph/9908116v1>

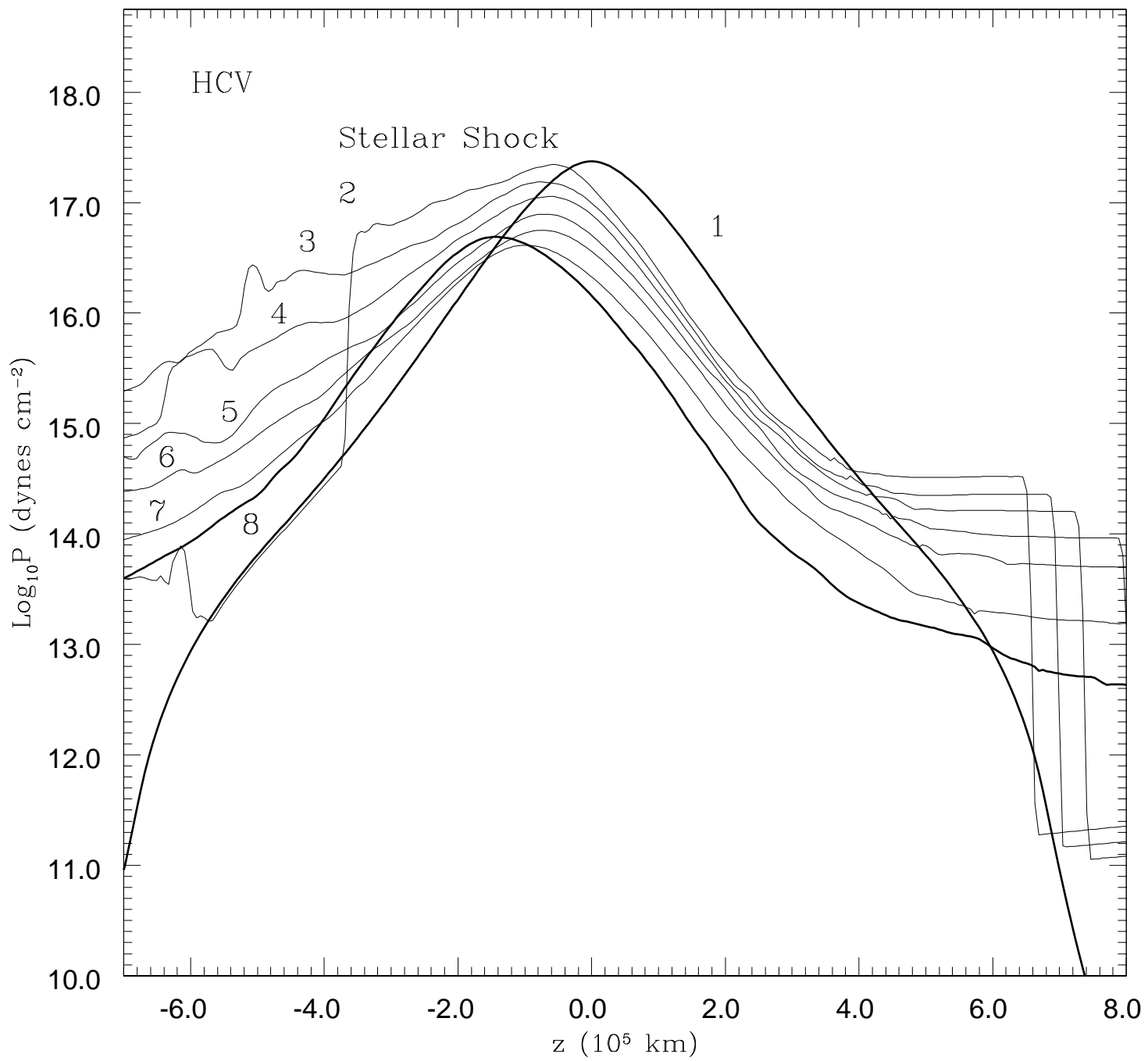
This figure "F5.gif" is available in "gif" format from:

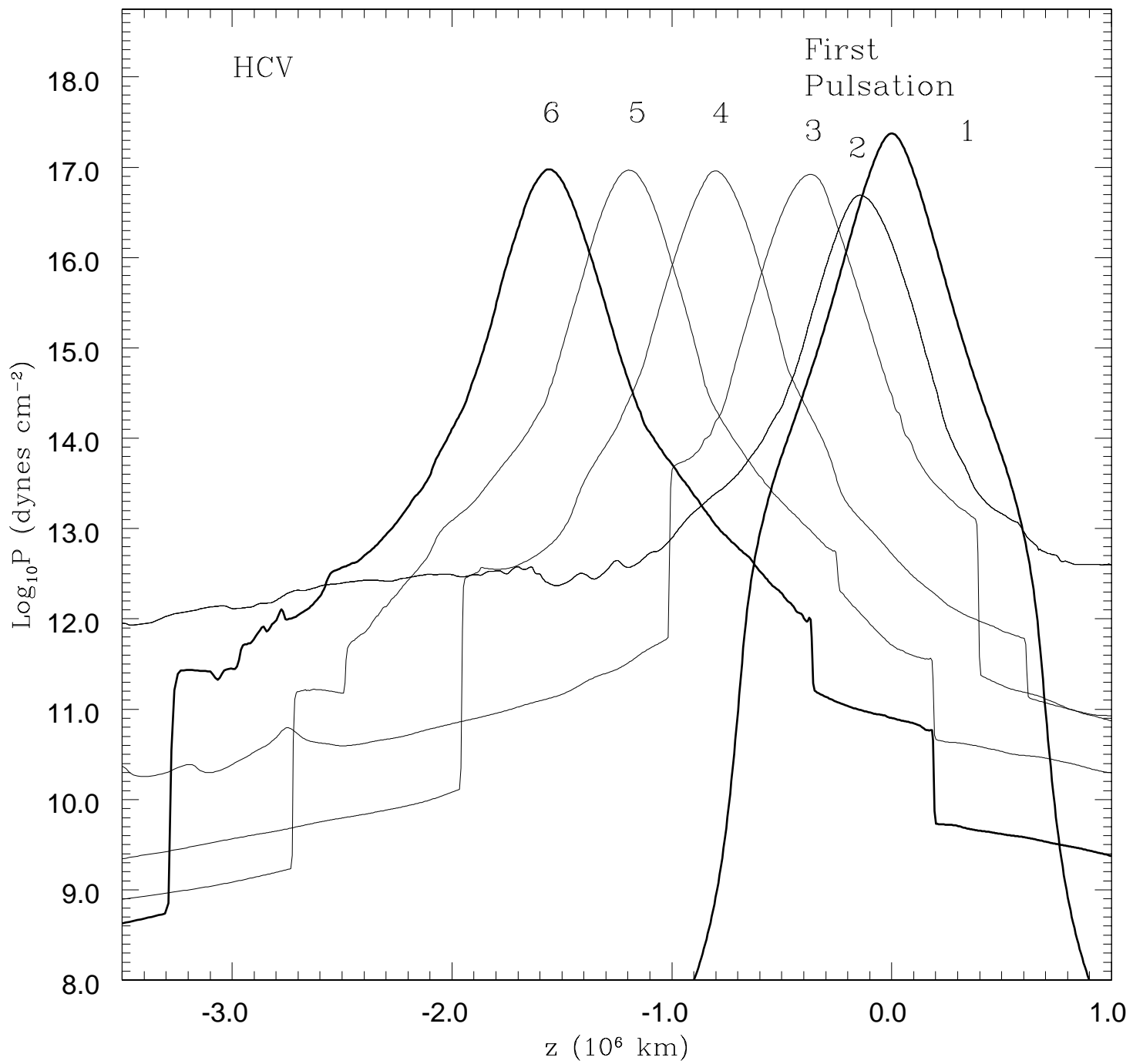
<http://arxiv.org/ps/astro-ph/9908116v1>

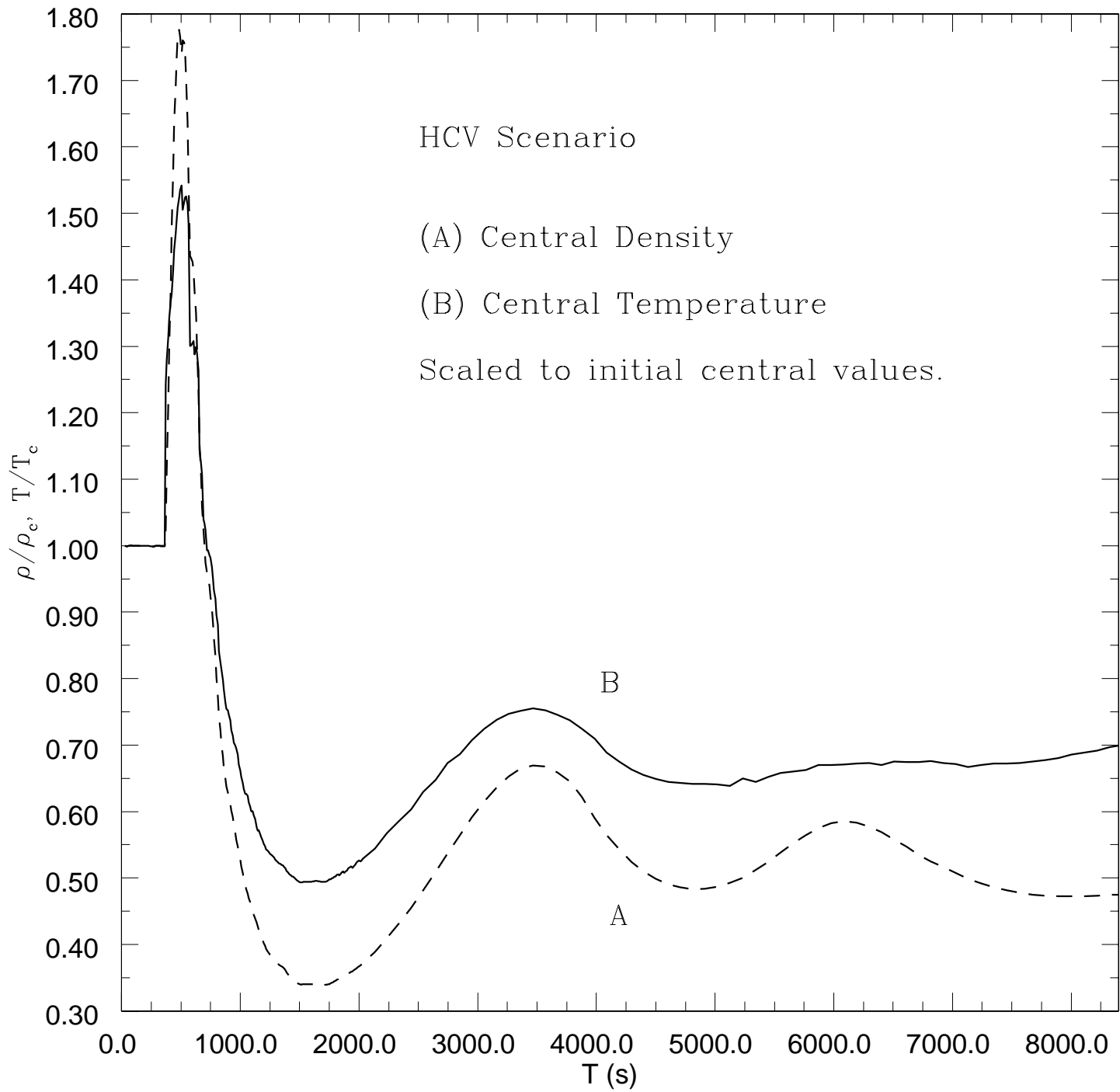


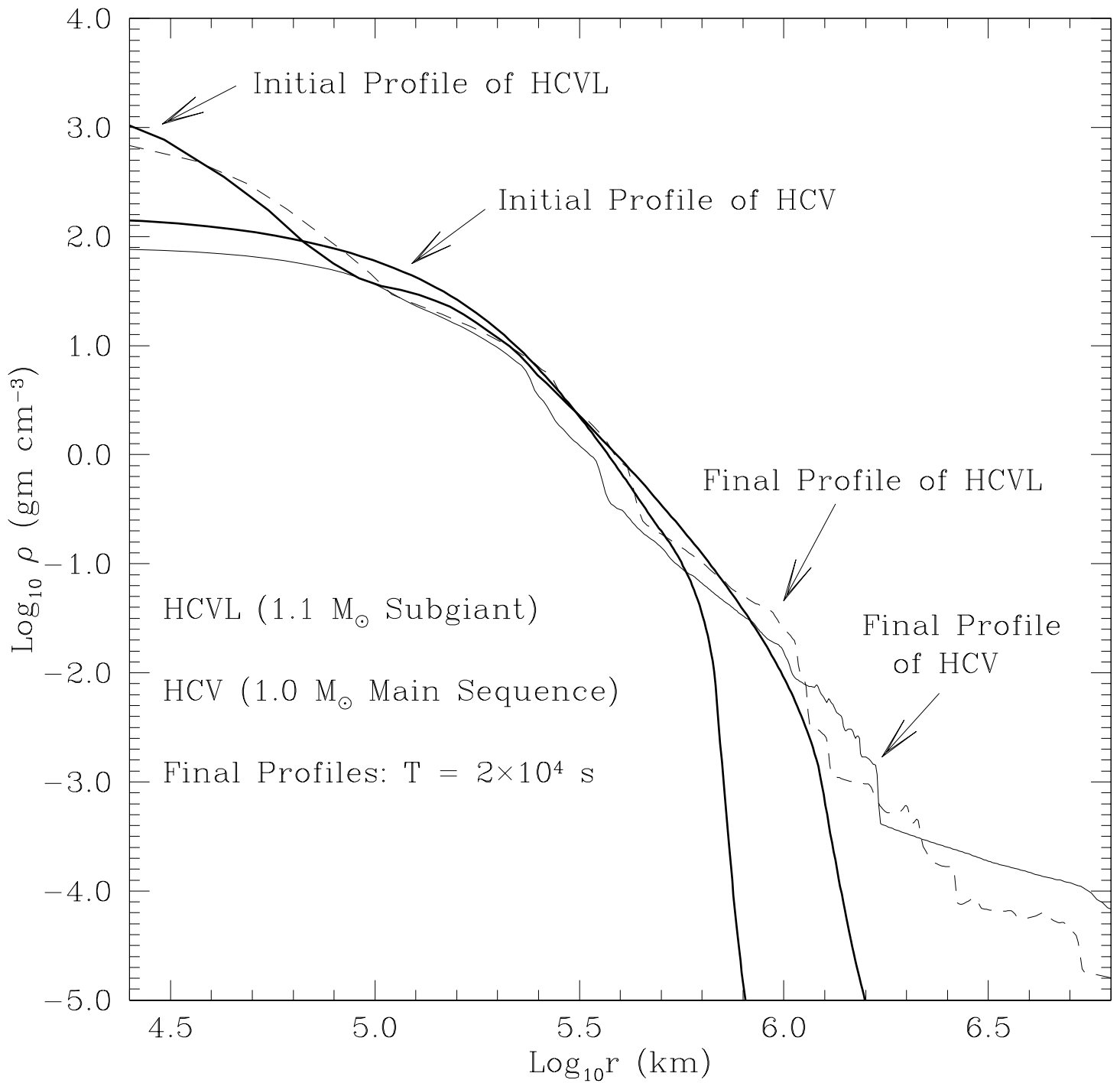


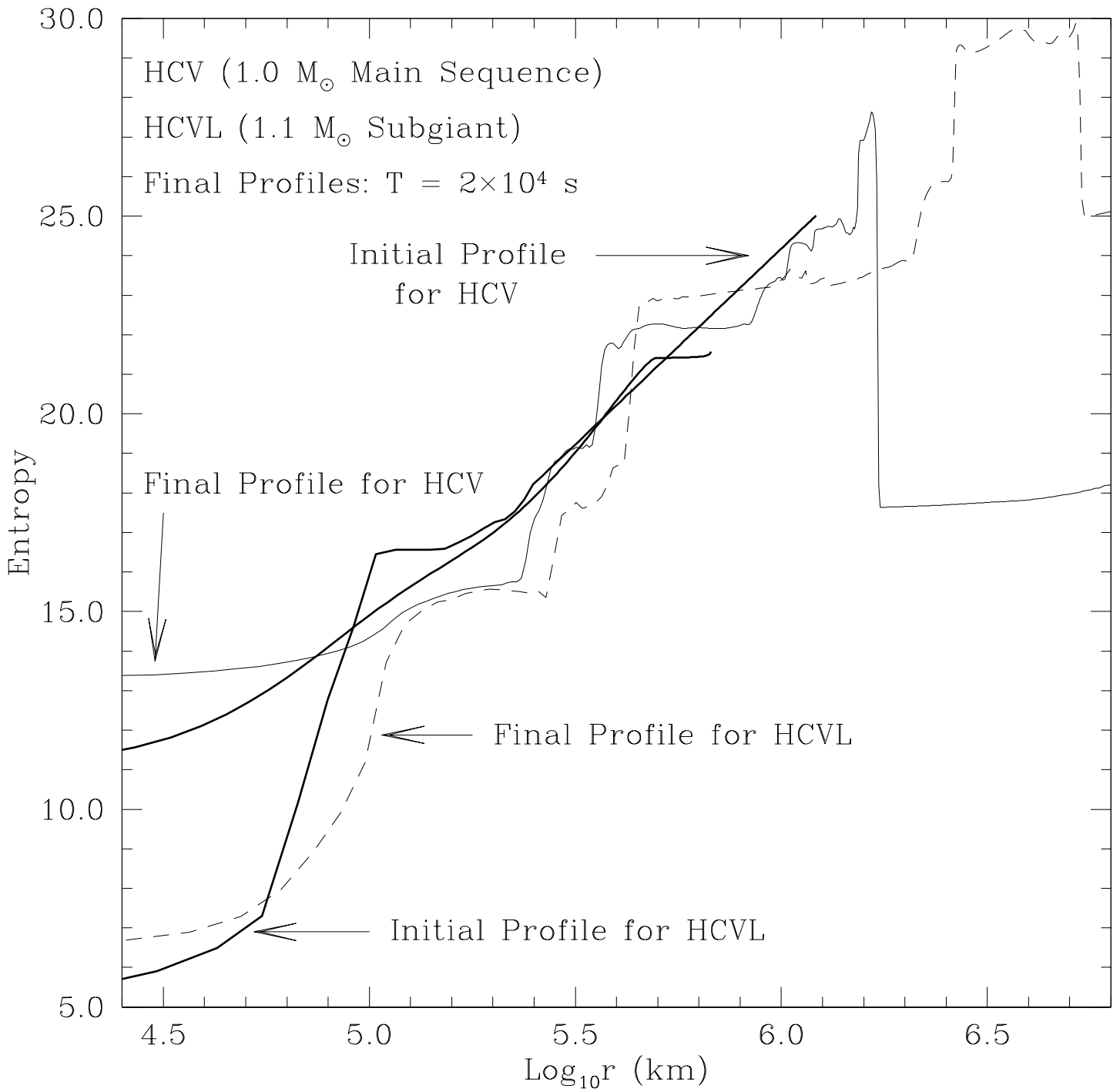


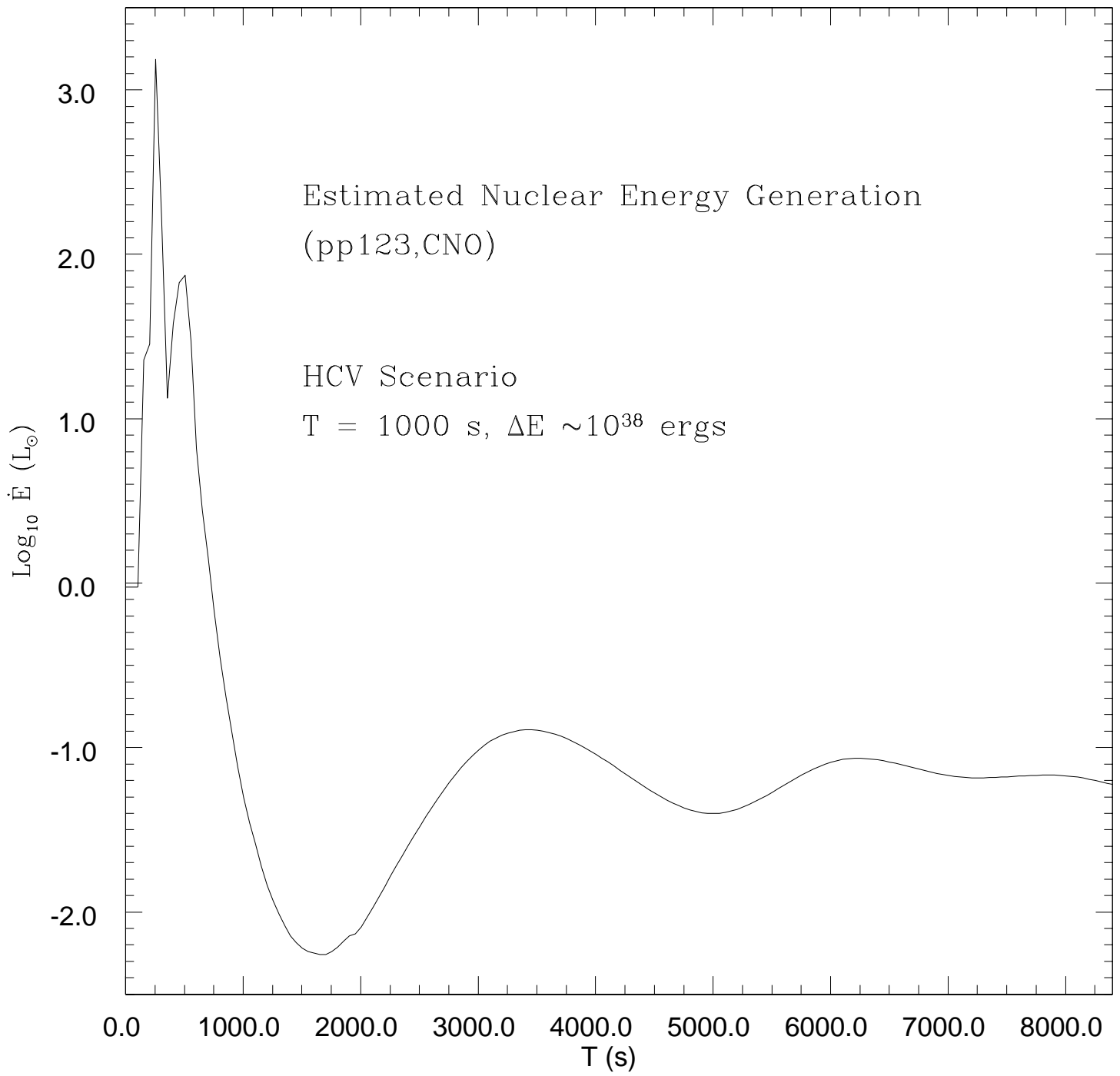


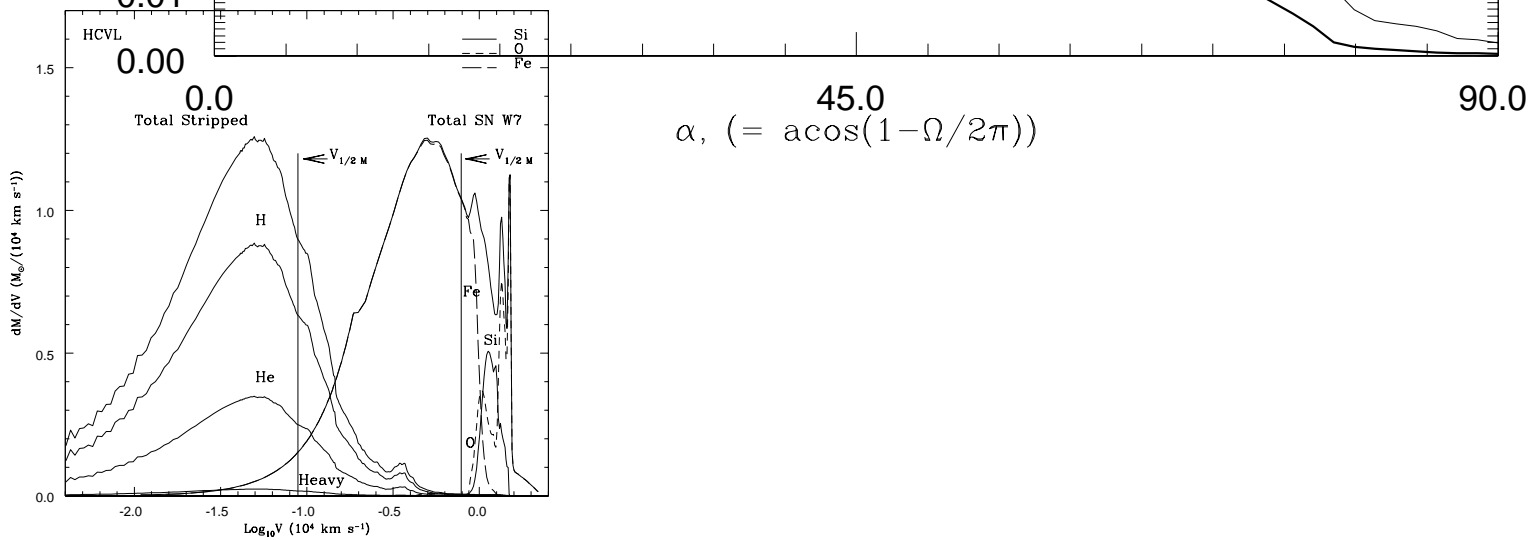
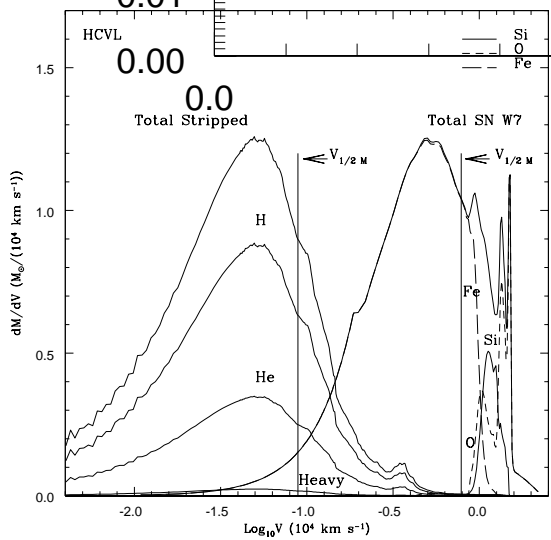
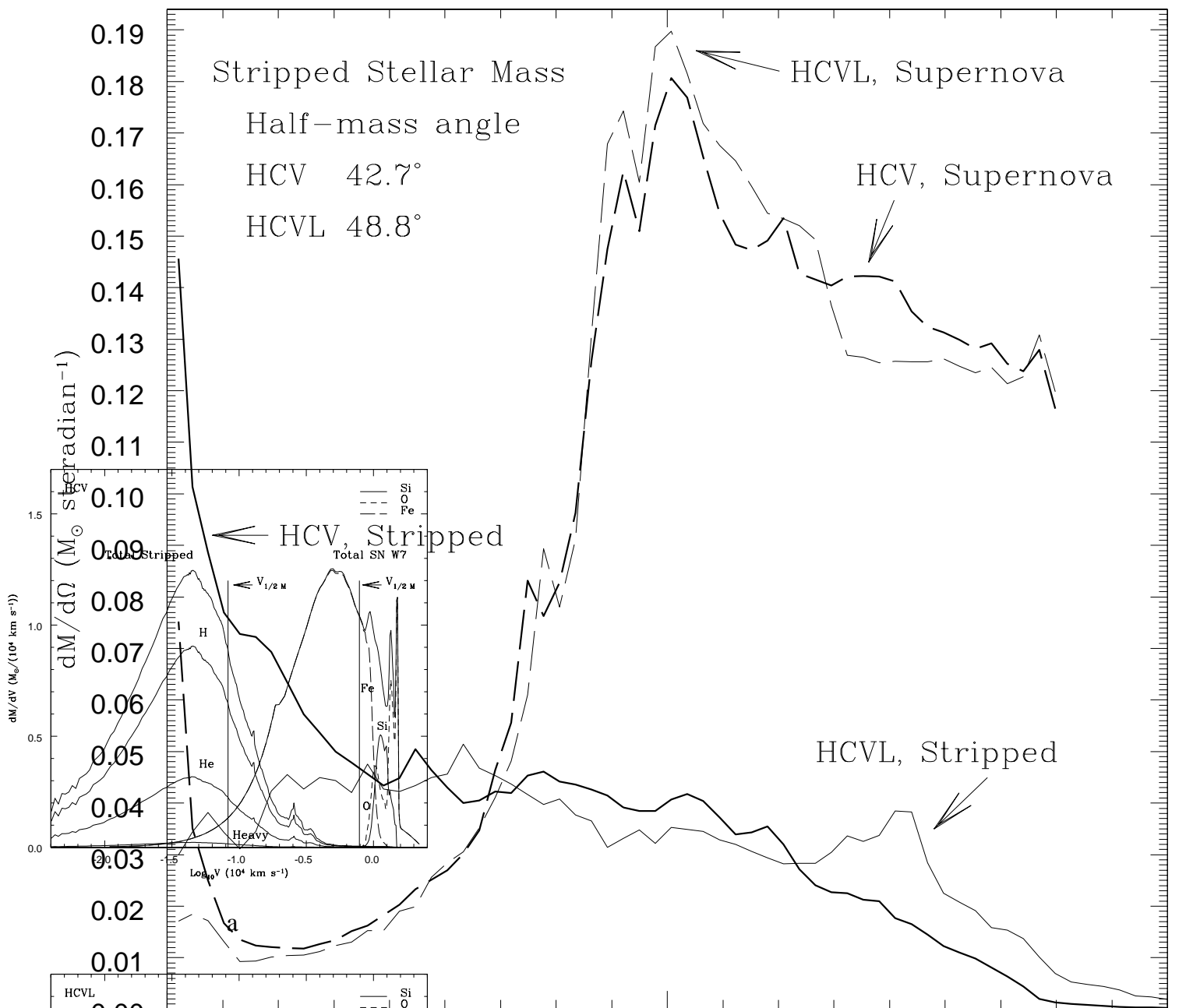








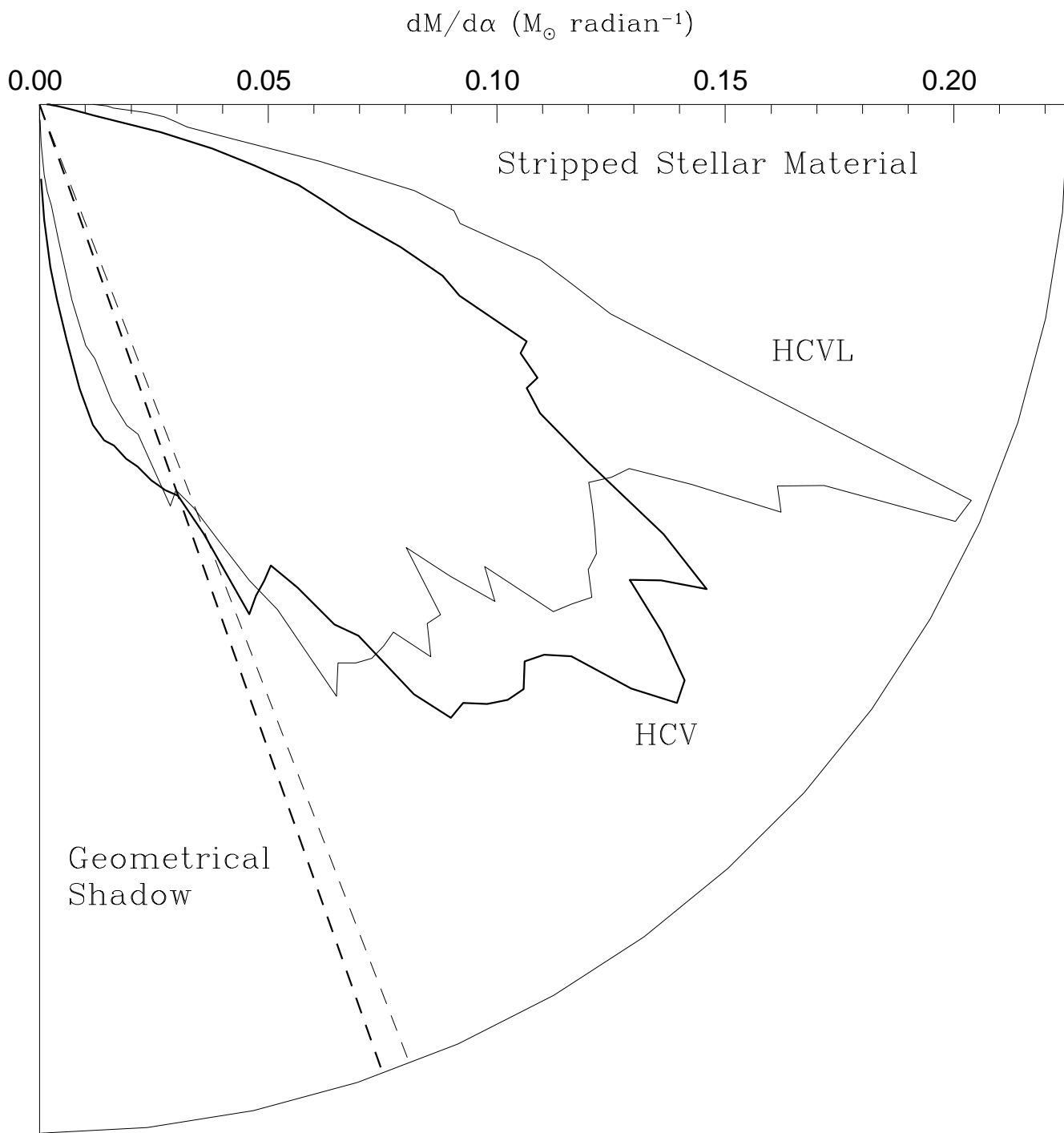




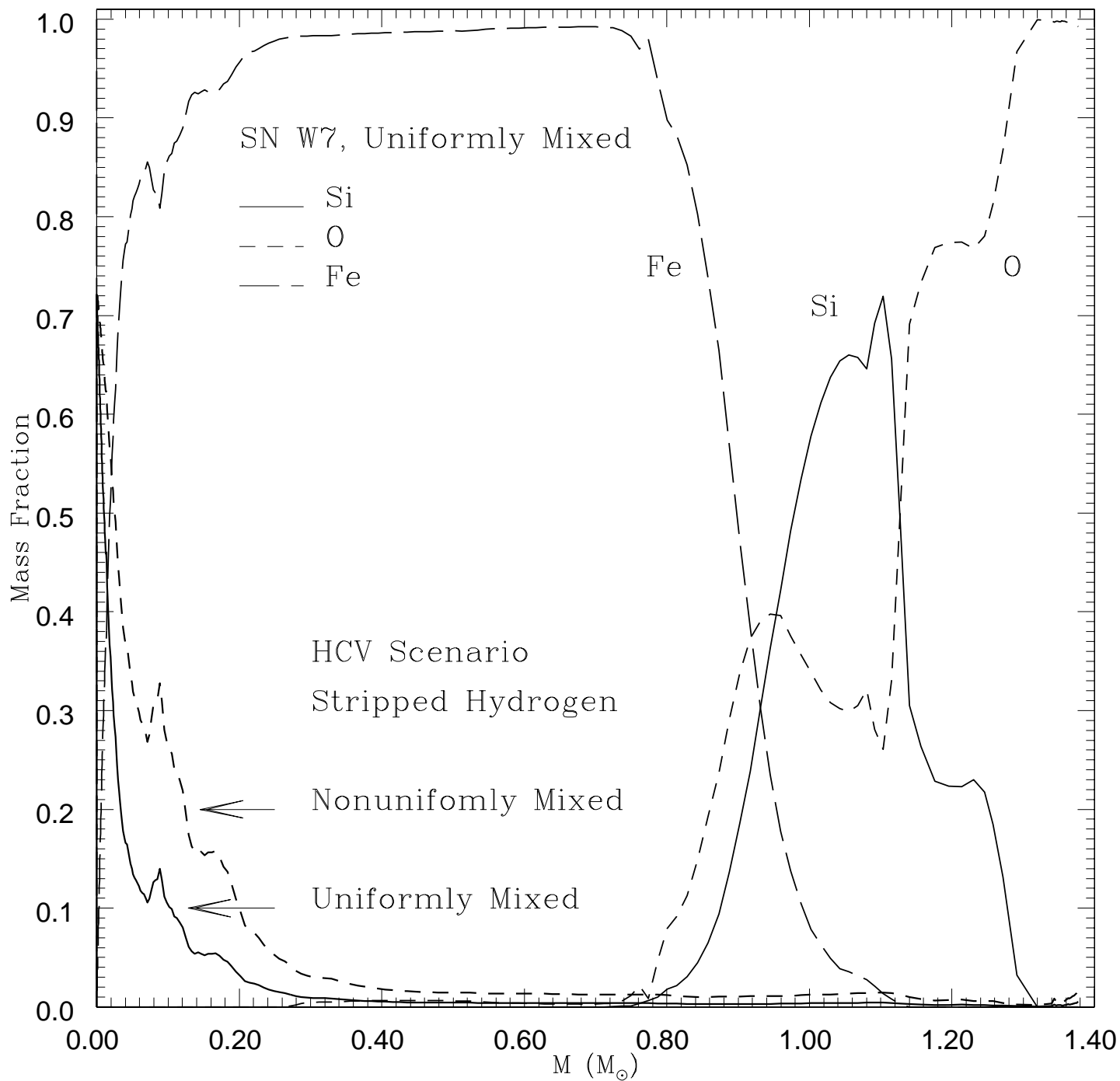
45.0

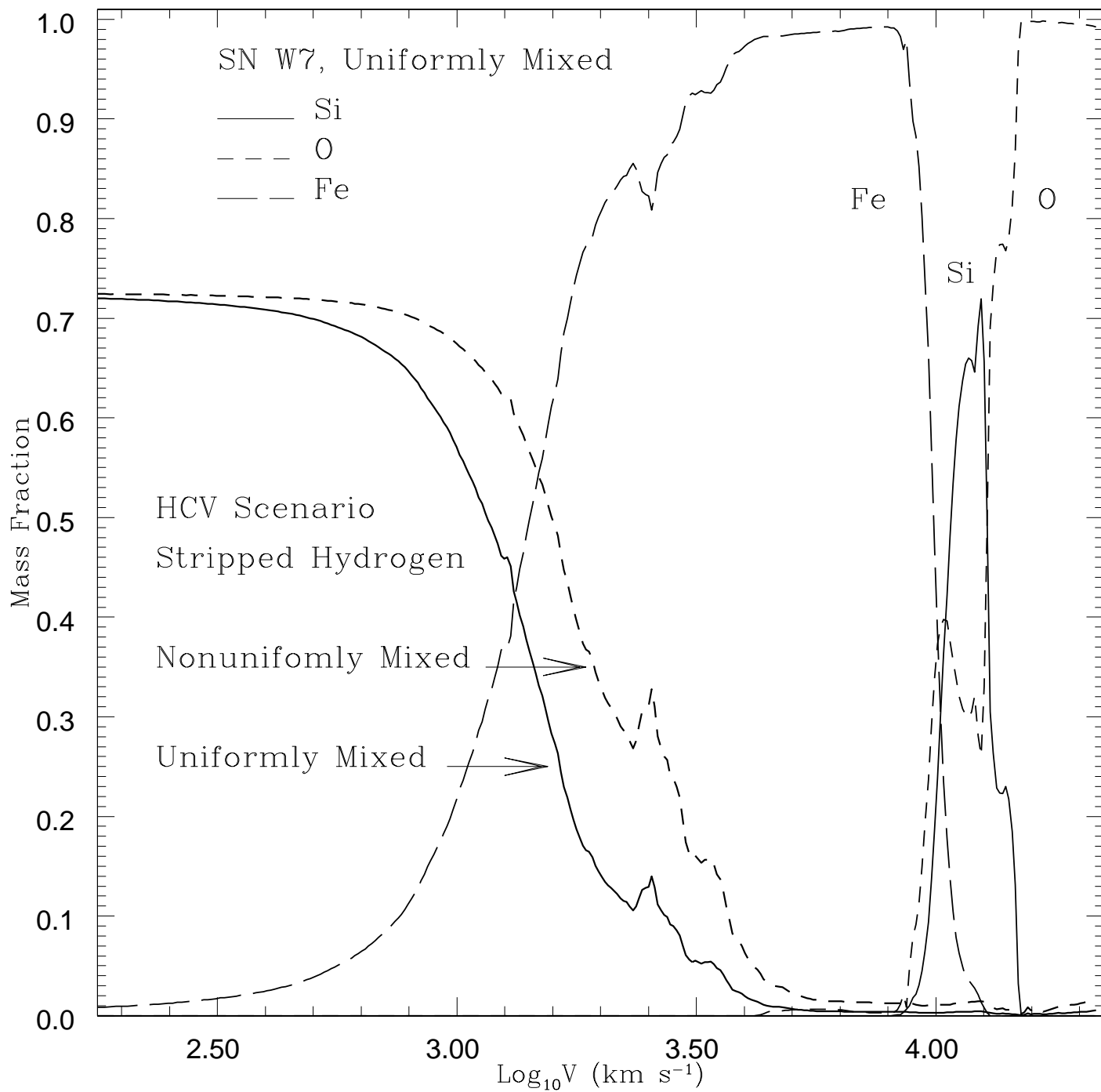
$\alpha, (= \text{acos}(1 - \Omega/2\pi))$

b



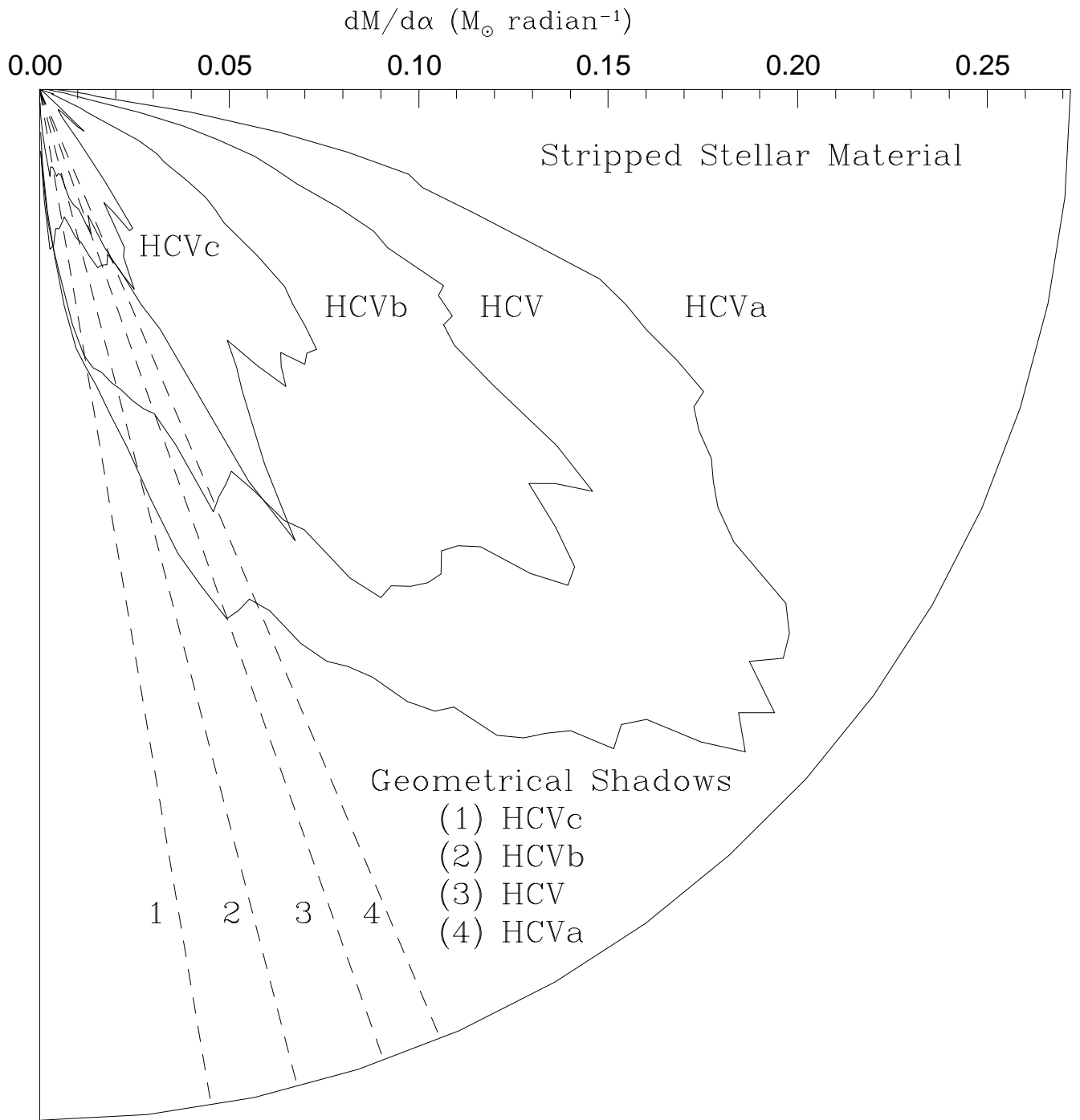






This figure "F19.gif" is available in "gif" format from:

<http://arxiv.org/ps/astro-ph/9908116v1>



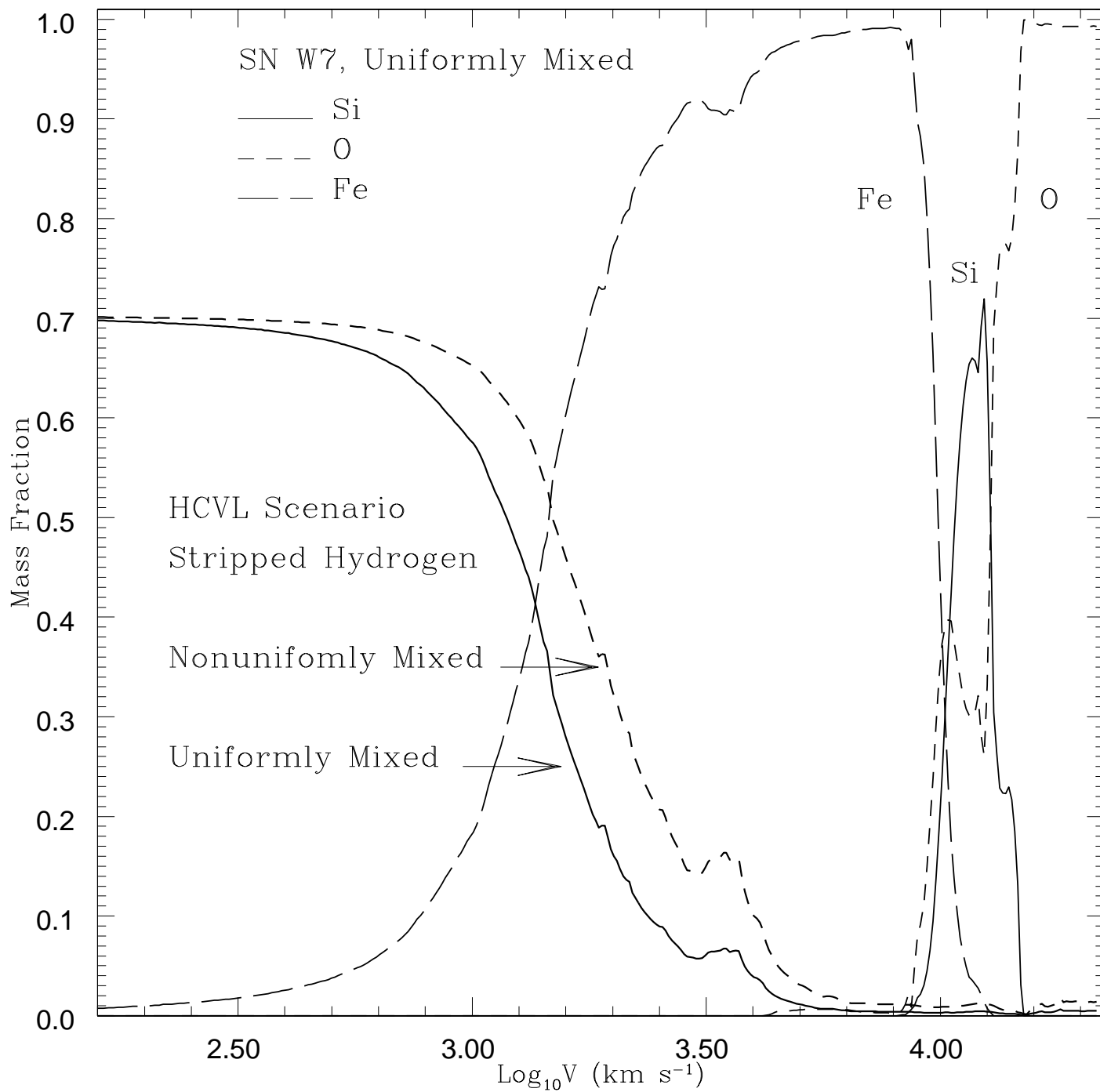
This figure "F21.gif" is available in "gif" format from:

<http://arxiv.org/ps/astro-ph/9908116v1>

This figure "F22.gif" is available in "gif" format from:

<http://arxiv.org/ps/astro-ph/9908116v1>







This figure "F25.gif" is available in "gif" format from:

<http://arxiv.org/ps/astro-ph/9908116v1>

This figure "F26.gif" is available in "gif" format from:

<http://arxiv.org/ps/astro-ph/9908116v1>

